Soft Lithographic Patterned Architectures in Dye Sensitized Solar Cells

Myoung-Ryul Ok

"A dissertation submitted to the faculty of the University of North Carolina at Chapel Hill
in partial fulfillment of the requirements for the degree of Doctorate of Philosophy
in the Curriculum in Applied Sciences and Engineering."

Chapel Hill

2013

Approved by

Edward T. Samulski

Alfred Kleinhammes

John M. Papanikolas

Rene Lopez

Sergei Sheiko

ABSTRACT

MYOUNG-RYUL OK: Soft Lithographic Patterned Architectures
in Dye Sensitized Solar Cells
(Under the direction of Edward Samulski)

Arrays of periodic surface features were patterned on mesoporous Nb_2O_5 and TiO_2 films by soft-lithographic techniques to construct photonic crystal (PC) structures on the back side of the oxide. The patterned oxide films were integrated into dye-sensitized solar cells (DSSCs) and their performance was evaluated relative to flat (unpatterned) counterparts. The PC structure on niobium oxide surfaces caused large changes in optical characteristics, particularly in the blue wavelength regime. The incident photon-to-current conversion efficiency (IPCE) of patterned niobium oxide anodes exhibited a relative enhancement over the entire wavelength range corresponding to the higher absorption in optical measurements. However, the effect of surface PC structures on the optical response of the TiO_2 is different from that of the Nb_2O_5 photoanode. The enhancement of light harvesting efficiency (LHE) is not obviously due to the higher thickness and larger dye loading than Nb_2O_5 films. However, patterned TiO_2 samples exhibited higher global efficiency than the flat reference, although there was no notable change in LHE. It was hypothesized that surface PC structures changed the de-trapping rate from trap states based on the simulated reflection behavior near the surface of the PC structure, and that in turn, enhances charge collection efficiency.

A cubic array of rectangular ITO posts (5×5×6.5μm, 10μm period) were fabricated on FTO coated glass in order to reduce the distance between charge generation points in the

mesoporous TiO_2 film and the transparent conductive oxide (TCO) layer in an effort to enhance charge collection in the DSSCs. In spite of the decrease in optical transmission due to the tall ITO structures, DSSCs with patterned ITO exhibited increased photocurrent by 12~18% to the reference DSSCs with identical volume of sensitized TiO_2. However, DSSCs with patterned ITO substructures showed deterioration in the open circuit voltage ($\boldsymbol{V_{oc}}$), fill factor, and global efficiency. Electrochemical impedance spectroscopy (EIS) showed that DSSCs with patterned ITO exhibited faster recombination rates leading to the decline in $\boldsymbol{V_{oc}}$,, fill factor, and global efficiency. We conclude that a barrier coating to suppress back electron transfer to the electrolyte should be conformally applied in order to take full advantage of the patterned ITO substructure.

ACKNOWLEDGEMENTS

I would like to express my appreciation to those numerous people who helped me to complete this work in many aspects.

Most of all, I owe the greatest thanks and praise to my advisor, Dr. Edward T. Samulski. He's been not only the perfect teacher in science with his ingenious ideas and stimuli, but a real mentor who always cares for my whole life in Chapel Hill. His intelligence guided me to the right direction and his tolerance and warmth waited till I could find a breakthrough myself whenever I encountered a wall in science. Also, my whole family deeply thanks him and Mrs. Samulski for their encouragement and consideration.

I also want to express my special thanks to Prof. Rene Lopez for his support and discussion. My research got nurtured by his stimulating discussions and encouragement. Without his support, I would have lost my way in optics and could not have overcome many challenges in this work. I would like thank to Prof. Sheiko for his discussions and care in my beginning days and help as a committee member. I also express my thanks to Prof. Papanikolas for his help as a committee member and his inspiration to the ITO works. And I want to thank Prof. Kleinhammes and Prof. Wu for their help as the committee member for my defense and prelim.

There are many I would like to express my gratitude for their support and discussion. Most of all, I want to thank Dr. Doo-Hyun Ko for his aids and discussions when I first joined

this group. His help is not limited only to the science, but includes timely lessons and advice to the life in Chapel Hill. Also, for my research, I cannot express my thanks too much to the help of Kyle, Rudy, and Leila. They taught me how to use lots of instruments and shared their ideas and time for discussion. Also, as my topics cover optics and PFPE, I owe much to Lopez group (Eugene, Emily, Cary, Yuki, Yingchi, Tim, and John) and Prof. DeSimone and his group (especially Chris and Charlie). I also want to express my thanks to Hanlin for her help and discussion. The CHANL also supported me much, and I want to thank Carrie, Amar, Bob, and Wallace. I also want to express my appreciation to the UNC EFRC for the research funding and many chances of seminar and useful discussions: I appreciate Prof. Meyer, Dr. Hoertz, Catherine, Ralph, and many other people in the center.

I also express my gratitude to the CASE and the administrative people to help me to work in the UNC Chapel Hill. I want to thank Carolyn Newman for her help on my first day in the office, Prof. Qin for his concern for the students during the first two semesters, and Prof. Washburn for his support as an associate chair of Applied Science. Also, I want to thank Duane for his help and warm advice as the physics lab director.

There are many friends who lubricated my life in Chapel Hill. I want to thank Tony for his warm heart and encouragement. I really enjoyed my years in the Samulski lab and want to express my thanks to the members, Yongchao, Walter, Agata, Craig, Mukti, Abay, and the last student of this group, Leah. Also, there are many Korean friends who shared their ideas, heart, and energy when I need help, advice, and/or relief. Most of all, I want to express my special appreciation to Dr. Sangwook Wu for his mentoring whenever I got depressed by the hardship as a student or a father. Also, I would like to thank Dr. Jinwoo Park, Dr. Sungjin Park, Dr. Changsun Eun, Dr. Wonhee Jeong, Dr. Honggu Chun, Dr.

Changjun Lee, and Prof. Soo-Hyoung Lee. I also want to express my gratitude to Seung Hun for his friendship, and finally, Dr. Ahyeon Koh, and Soo Yeon Sim for their help, discussion, and shared memories in Chapel Hill. Also, I want to encourage Yejee Han who is about to start her life in the UNC Chapel Hill.

There are also many people I want to express my gratitude in Korea. I would like to express my special thanks to Dr. Kyung Tae Hong, who helped me to start my professional career as a scientist and taught me a lot of virtues a scientist should have. I also want to thank Prof. Dongil Kwon for his instruction that helped me to build a strong foundation as a professional. I also want to express my gratitude to Dr. Seunghee Han and Dr. Eric Fluery for their help in research and the application process. And I would like to thank Dr. Jin-Yoo Suh for his overall contribution to my career and life. I want to express my thanks to Dr. HyunKwang Seok for his support and concern to my future direction. And I feel really sorry there are too many scientists and staffs to acknowledge here, especially in KIST, but the pages are limited: I want to express my thanks to all of them and apologize not to be able to write down all of their names.

However, I could not complete my requirements without the encouragement and support from my family. First of all, my mother is the most influential person of all. From my childhood, she always raised me in a more difficult but powerful way, by showing me commitment, tolerance, and honor, rather than referring those virtues. I want to express my gratitude and love to her. I feel sorry my father cannot see me become a Ph.D, but his love remained in me, and I feel his love to me was actually much bigger than I felt in the past, as I become a father myself. Also, I want to express my special thanks to my sisters for their lifelong concern, support, and love to the only brother. And I would like to thank my

brothers-in-law for their support and concerns like the real ‘brothers’, and nephews and nieces, Sehoon, Sanghyun, Se-in, and Soyeon.

And I cannot express my thanks too much to my father-in-law and mother-in-law: they have always regarded me and my wife’s decisions, encouraged us, and never saved their support and blessing. Moreover, especially when my two kids were born, without their special care, I could not have reconciled myself to a father. I also thank my sister-in-law and her family for their encouragement and concern.

But, the greatest contribution to my Ph.D was from my wife, Eun Young. Although she encountered the first hardship in her life as a wife of a foreign student and had to struggle to overcome loneliness, she always encouraged and supported me by her brightness and sacrifice, as a good wife and mother. I would express my special appreciation and love to her, beyond the limits of language. Also, I want to express my love to my sons, Jino and Sean, who healed me every day, and my daughter to be born in November.

TABLE OF CONTENTS

LIST OF TABLES

Table

LIST OF FIGURES

Figure

LIST OF ABBREVIATIONS AND SYMBOLS

$A(\lambda)$	Absorption
AAO	Anodic aluminum oxide
AFM	Atomic force microscopy
ALD	Atomic layer deposition
AM	Air mass
AMOL	Absorbance modulation optical lithography
CCE	Charge collection efficiency
CIE	Charge injection efficiency
CVD	Chemical vapor deposition
DSPEC	Dye-sensitized photo-electrochemical cells
DSSC	Dye-sensitized solar cell
EIS	Electrochemical impedance spectroscopy
EQE	External quantum efficiency
FF	Fill factor
FTO	Fluorine-doped tin oxide
I	Current
IPCE	Incident-photon-to-current conversion efficiency
IS	Integration sphere
ITO	Tin-doped indium oxide
J	Current density
J_m	Photocurrent at the maximum power point
J_{sc}	Short circuit current density

LHE	Light harvesting efficiency
M_w	Molecular weight
MIMIC	Micromolding in capillaries
NP	Nanoparticle
P_{inj}	Incident power to the DSSC
PBG	Photonic band gap
PC	Photonic crystal
PDMS	Polydimethylsiloxane
PFPE	Perfluoropolyether
PLD	Pulsed laser deposition
PS	Polystyrene
PU	Polyurethane
PV	Photovoltaic
R(λ)	Reflection
REM	Replica molding
RIE	Reactive ion etching
SAED	Selected area electron diffraction
SAMIM	Solvent-assisted micromolding
SEM	Scanning electron microscopy
T(λ)	Transmission
TCO	Transparent conductive oxide
TEM	Transmission electron microscopy
V	Photovoltage

V_m	Photovoltage at the maximum power point
V_{oc}	Open circuit voltage
XRD	X-ray diffraction
η	Global efficiency
μCP	Microcontact printing
μTM	Microtransfer molding
φ_{inj}	Charge injection efficiency

CHAPTER 1

LITERATURE REVIEW OF AND INTRODUCTION TO SOFT-LITHOGRAPHY AND DYE-SENSITIZED SOLAR CELLS

1.1 Introduction to soft-lithography

Nanopatterning is one of the key technologies in modern science and engineering. Most of the nanopatterning methodologies were developed initially for semiconductor industries[1] which require continued reduction of feature sizes to integrate more components per unit area, reduce manufacturing cost, miniaturize electronic devices, lower power consumption, and increase processing power of the devices.[2] Recently, it has been discovered that nanostructured materials do not simply mean physically smaller feature sizes, but new properties of existing materials solely stemming from their dimensions.[3-8] Good examples of these inherent departures from nominal properties with decreasing size are the metal-insulator transitions of metal clusters,[3] the Coublomb blockade and single electron tunneling,[4] and quantum dots.[5-8] So, it becomes even more important to develop nanopatterning methodologies not only to enable smaller feature sizes, but to build new nanostructures with a variety of functional materials in various fields, such as optics,[9] biotechnology,[10] and/or energy materials.[11,12]

In this section, I provide a brief review of nanopatterning methods focusing on the conventional photolithographic technologies and the newly developed soft-lithographic methods.

1.1.1 Photolithography

Photolithography is a technique to utilize UV lights, photomasks, and photoresists to fabricate patterns.[1] Figure 1.1[10] shows a typical nanopatterning processes using conventional photolithograpy. A thin photoresist layer was spin-coated onto the substrate (first step of the Figure 1.1) and exposed to UV radiation to develop a nanopattern in the photoresist on the substrate. In this step, usually a projection-printing system is utilized for projecting the image/pattern on the photomask in reduced size onto the photoresist thin film.[13,14] By proper etching and removal of the residual photoresist, nanopatterns are subsequently formed on the substrate. Since photolithography utilizes projections of images at the photomasks onto the photoresist to transfer the nanopatterns, the resolution of the nanopatterns are determined by the precision of the optical system. It is widely known that shorter wavelengths are critical to getting smaller resolution in optical microscopy.[1] So, UV wavelengths used for photolithography have moved to shorter wavelengths, e.g. 436nm (g line of Hg lamp, resolution of the nanostructure: 500nm), 365nm (i line of Hg lamp, 350nm resolution), 248nm and 193nm (KrF and ArF excimer laser respectively).[1,14] However, higher resolution could be achieved even with the same wavelength of UV in combination with delicate optical technologies like phase shifting masks,[15] immersion optics,[16,17] or the absorbance modulation optical lithography (AMOL)[18] to overcome the wavelength limitation. For further reduction of feature sizes below 100nm, advanced lithographic techniques such as electron-beam lithography,[19] X-ray lithography,[20] ion beam technologies,[21] and/or proximal probe

lithography[22] are required. On the other hand, there are several problems with the fabrication of nanopatterns that depend on the photolithographic methodology: adaption of these new technologies inherently results in a spike in the manufacturing costs;[14] moreover, photolithography can basically be applied only to flat surfaces due to its optical nature.[1,14] Moreover, with the spreading of nanopatterning technologies beyond microelectronics, there arose strong needs for nanopatterning techniques which can form nanostructures not only simply with photosensitive materials, but with various functional materials to pattern functionalities on the surface,[23] e.g., proteins on the surface,[24] or organic photovoltaic materials.[25] So, new methods for nanopatterning which are easily accessible to scientist in various fields and are low cost became necessary. The new technology should also be able to pattern various functional materials below the micrometer scale, even onto non-flat surfaces.

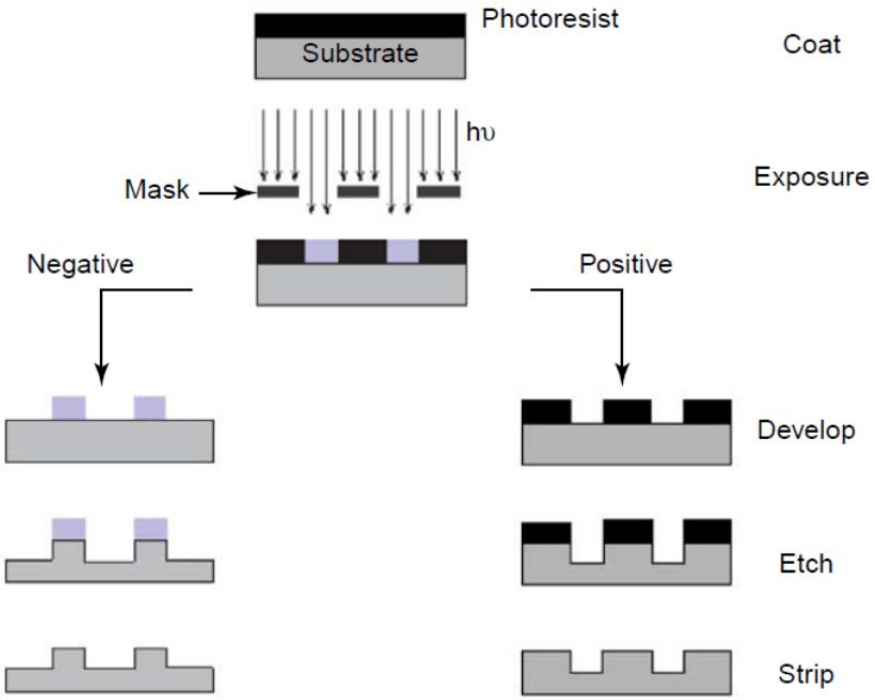

Figure 1.1 Schematic representation of the typical photolithography steps for nanopatterning. (Reprinted with permission from reference 10. Copyright © 2006 Elsevier Ltd.)

1.1.2 Soft-lithography

As nanotechnologies become mature and widespread in various fields of sciences and engineering over the last couple of decades,[26-29] the manufacturing cost of the nanopatterning techniques has become a more important factor to researchers in various fields. To the biological scientists and materials scientists who require a number of experiments, nanopatterning techniques have still been difficult to access and expensive[14] to manage for the bulk of experiments, in part because nanopatterns fabricated by state-of-the-art techniques are expensive and are usually just for one-time use. So, there has been a strong demand for new techniques which enable the construction of nanopatterns at a resolution on the ~100nm level with reduced expense.[10,14]

Whitesides and coworkers have opened a new field called 'soft-lithography' which enabled low cost fabrication of nanopatterns on the lab-scale in the 1990s:[14,23,29] instead of building new nanopatterns with photolithography every time, they reproduced nanopatterns by adapting soft elastomers which are the 'replicas' of the expensive master nanopatterns made by conventional photolithography. Polydimethylsiloxane (PDMS) has been the main elastomer since the invention of the soft-lithography,[14] and other polymeric materials such as polyacrylates,[30] polyurethane (PU),[31] fluoropolymers,[32,33] polyolefins,[34] polycarbonates.[35] Recently, a new fluoropolymer, perfluoropolyether (PFPE) was developed and intensively used for nanopatterning by DeSimone and coworkers.[36-38] PFPE has advantages such as high permeability of vapors, higher strength, and low surface energy compared to the prevailing PDMS.[37]

Soft-lithography is generally classified in detail as microtransfer molding (μTM),[39] replica molding (REM),[40] solvent-assisted micromolding (SAMIM),[41] micromolding in

capillaries (MIMIC),[42] and microcontact printing (μCP),[43] depending on the physical and chemical characteristics of the methods. Figure 1.2[29] is a schematic representation of the specific soft-lithography techniques listed above.

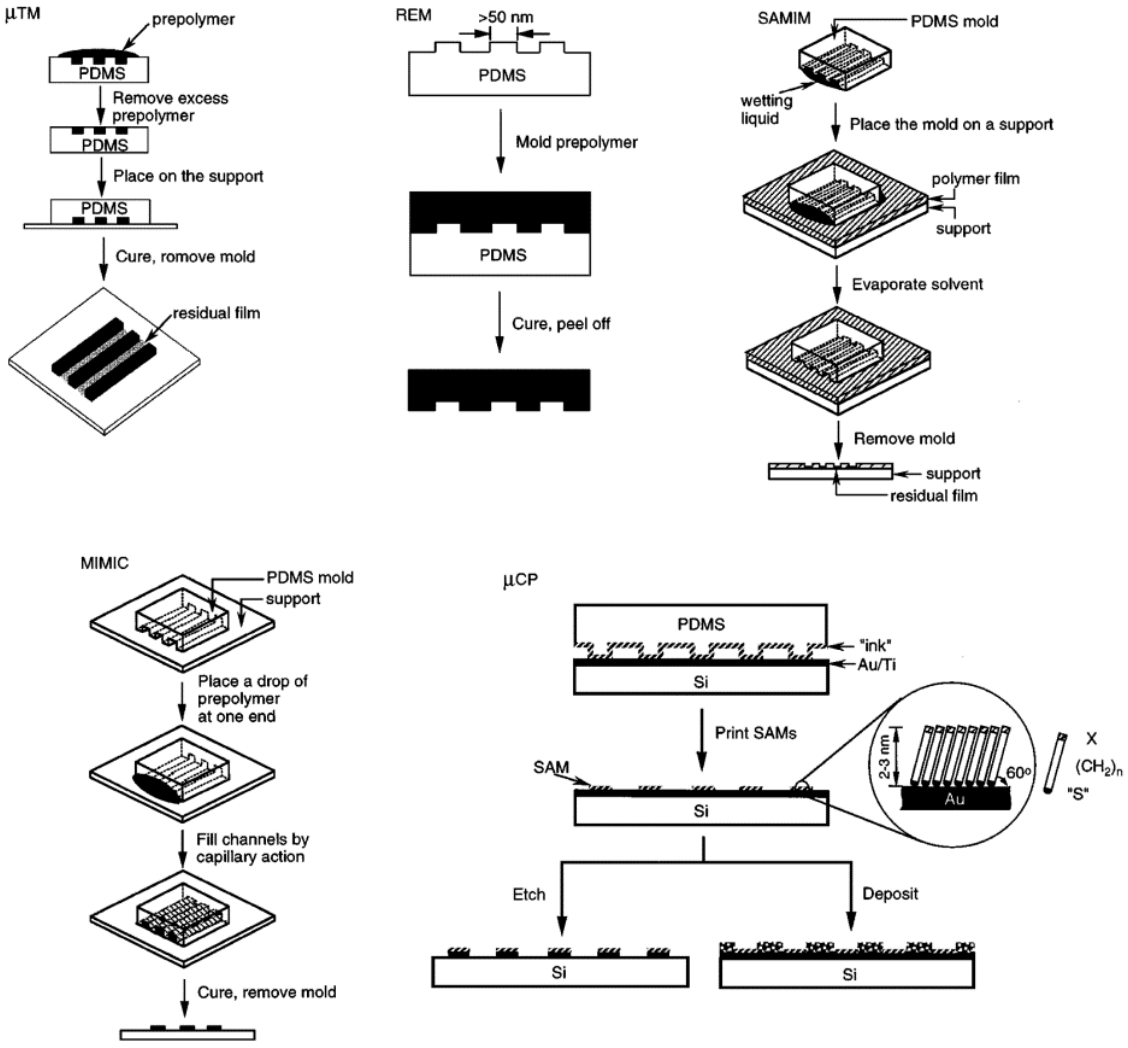

Figure 1.2 Schematic representation of soft-lithographic techniques following the classification of reference 29. (Reprinted with permission from reference 29. Copyright © 1998 Annual Reviews)

1.2 Dye-sensitized solar cells (DSSCs)

With the predicted exhaustion of current fossil energy resources, extensive and intensive research is ongoing for the realization of solar energy, one of the attractive sustainable energy technologies.[44] According to Grätzel,[45] as the solar energy supplied in a year is estimated to be 3×10^{24}J, more than 10^4 times of the annual energy consumption by human civilization. Energy produced by photovoltaic (PV) cells with just 10% conversion efficiency covering 0.1% of the earth's surface could supply sufficient energy to mankind. In the history of PV technology, initial PV cells have been dominated by solid-state junction devices based on crystalline or amorphous silicon which could be readily adapted to the built-in technologies of the silicon semiconductor industries,[45] as is evident in Figure 1.3.[46]

The dye-sensitized solar cell (DSSC) has been one of the emerging photovoltaic cells with very low production costs since the first report of 7.1% efficiency by O'Regan and Grätzel in 1991.[47] By the combination of better dye molecules absorbing a wider spectrum of sunlight,[48-52] and/or new electrolytes with enhanced transport,[53-55] their efficiency exceeded 12% in 2011,[55] and current world record is 15%.[56]

In this section, I present brief explanations of the basic operating principles of the DSSC. Also, I introduce the research trends and issues associated with the improvement of the conversion efficiency of the DSSCs in terms of the basic operating principles.

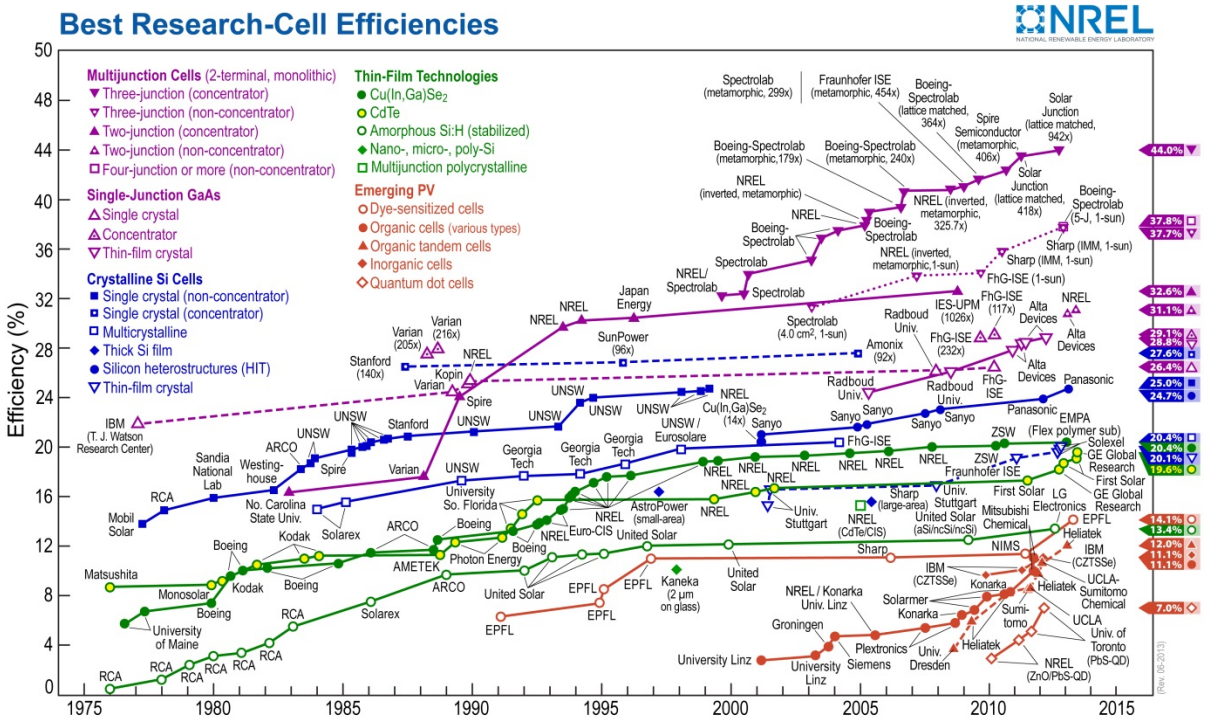

Figure 1.3 Best research cell records of various types of PV cells by timeline. (This figure is reprinted with permission by the National Renewable Energy Laboratory, http://www.nrel.gov/ncpv/images/efficiency_chart.jpg.[46] Accessed July 24, 2013.)

1.2.1 Basic principles and terms of DSSCs

As anatase nanoparticle TiO_2 has a band gap energy of 3.2eV,[57] which corresponds to the photon energy of the UV light, it is not a proper material for photovoltaic cells as it is, because it cannot absorb and utilize a large portion of sunlight, i.e., the visible and the IR. So, in DSSCs, TiO_2 nanoparticles are sensitized with a mono layer of dye molecules which absorb a wide spectrum of sunlight and inject excited electrons to the underlying supporting TiO_2, and the electrolyte transferring electrons to the holes in the dye molecules.[45] As DSSCs solely depend on the monolayer of dye molecules to harvest photons and produce electrons, the TiO_2 layer should have a large surface area in order to accommodate the maximum number of dye molecules on the surface of TiO_2. Typically, the TiO_2 layer in the DSSC has a

mesoporous morphology consisting of nanoparticles around 20nm; this provides sufficient internal surface area—a factor of 1000 greater than the arial area.[48] The injected electrons diffuse through the nanoparticle network to be finally collected by an FTO film before flowing to the counter platinized electrode through an external circuit. The typical electrolyte contains iodide/triiodide (I^-/I_3^-) ions:[45] when a dye molecule (denoted by S in its stable state) absorbs a photon to give an excited electron in its LUMO level (S*), it can inject the electron to the TiO_2, and thereby leave a hole in the HOMO of the dye (S^+). Finally, the I^- ions in the electrolyte regenerate the dye ($S^+ \rightarrow S$) and transform to I_3, which can be oxidized again to the I^- ion at the platinized counter electrode. The schematic representation of the operation principle of the DSSC is summarized in Figure 1.4.[47]

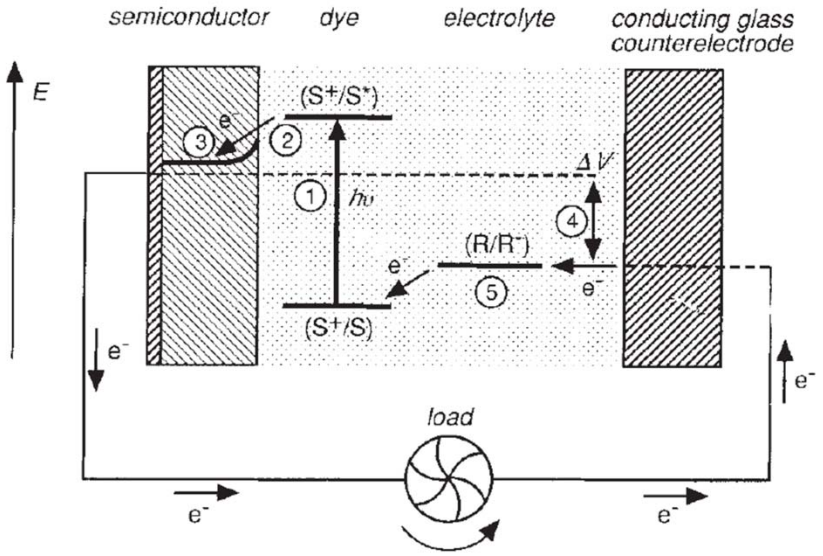

Figure 1.4 Schematic representation of the operation principle of DSSC. (Reprinted with permission from reference 47. Copyright © 1991 Nature Publishing Group)

Generally, DSSCs are composed of a photoanode which is a sensitized TiO_2 film on the transparent conductive oxide (TCO) electrode (typically the fluorine-doped tin oxide (FTO)), a platinized cathode, and an electrochemical redox electrolyte containing I^-/I_3^- ions

for regeneration of dye molecules. For enhanced stability, solid state DSSCs with the solid hole-conducting organic layer were reported[58] to avoid liquid electrolytes which are less stable and difficult to seal.

Characterization of the solar energy conversion performance of DSSCs is basically evaluated by the incident-photon-to-current conversion efficiency (IPCE) measurement as a function of photon wavelength, and the ***J*-*V*** (or ***I*-*V***) measurement under simulated sunlight, typically called AM1.5 (100mW/cm^2, full sunlight).[58] IPCE is the ratio of the number of electrons collected at the external circuit to the incident flux of (monochromatic) photons on the sensitized TiO_2 films, generally expressed as equation 1.[47]

$$\mathrm{IPCE}(\lambda) = \mathrm{LHE}(\lambda) \times \varphi_{inj} \times \eta_{coll} \tag{1.1}$$

Here, LHE(λ) is the light harvesting efficiency, φ_{inj} and η_{coll} are charge injection efficiency (CIE) and charge collection efficiency (CCE), respectively. The details of the LHE, CIE, and CCE will be discussed in the next section. IPCE is also called the external quantum efficiency (EQE).[59] As IPCE indicates the conversion efficiency as a function of wavelength, it is especially useful when combining a photonic crystal geometries with DSSCs.[59-61]

The ***J*-*V*** (or ***I*-*V***) measurement shows the maximum photovoltage (called as the open circuit voltage), photocurrent (short circuit current), and power output of the DSSCs. By linearly sweeping potentials (typically from -1V to 1V interval), resultant current is monitored with and without illumination. The ***J*-*V*** curve in the dark reveals the electrical characteristics of the DSSC, e.g. the shunt resistance, etc.[62] Important parameters under illumination are the open circuit voltage ($\boldsymbol{V_{oc}}$), the short circuit current density ($\boldsymbol{J_{sc}}$), the

maximum power output and/or global efficiency (η) of the cell, and the fill factor (***FF***). The open circuit voltage, $\boldsymbol{V_{oc}}$, is the maximum voltage in the ***J-V*** curve when the DSSC is in an open circuit condition, i.e. the net external current is equal to 0. So, under open circuit conditions, as the external current is equal to zero, electrons injected to the TiO_2 network from the dye molecules should be balanced by the electron back transfer from the conduction band of TiO_2 to the I_3^- ions in the surrounding electrolyte.[63] The measured open circuit voltage is the difference between the quasi Fermi level of the TiO_2 and the redox potential of the triiodide/iodide ions in the electrolyte,[45] as shown in Figure 1.4 (noted as ΔV in the figure). The short circuit current density, $\boldsymbol{J_{sc}}$, is the maximum photocurrent density flowing out to the external short circuit. So, the measured short circuit current is the flow of photoelectrons injected by the dye molecules into the TiO_2 nanoparticle network, and diffused through it to the FTO layer, and flew out to the external short circuit.[63]

In real conditions, utilization of both maximum photocurrent and photovoltage is impractical, due to the series resistance and finite shunt resistance not perfectly suppressing alternative pathways for electron transfer.[64] So, by multiplying the photocurrent density (in mA/cm^2) and the photovoltage (V) of every point in the ***J-V*** curve, one can get the maximum power output. Using the maximum power output conditions ($\boldsymbol{J_m}$ and $\boldsymbol{V_m}$ in the Figure 1.5), the fill factor (FF) of the cell can be obtained as the ratio of the value $\boldsymbol{J_m \times V_m}$ (area of the rectangle in orange color in the figure) to $\boldsymbol{J_{sc} \times V_{oc}}$ (denoted as the rectangle in blue color in the figure). Equation 1.2 is the global efficiency (η) of the DSSCs using the fill factor.[47]

$$\eta = \frac{J_{sc} \times V_{oc} \times FF}{P_{inc}} \tag{1.2}$$

Here, P_{inc} is the incident power to the DSSC in measurement, usually 100mW/cm^2 corresponding to the solar energy density of AM1.5.[58] Very recently, the Grätzel group reported an efficiency of 15%, the world record of the (solid state) DSSC so far.[56]

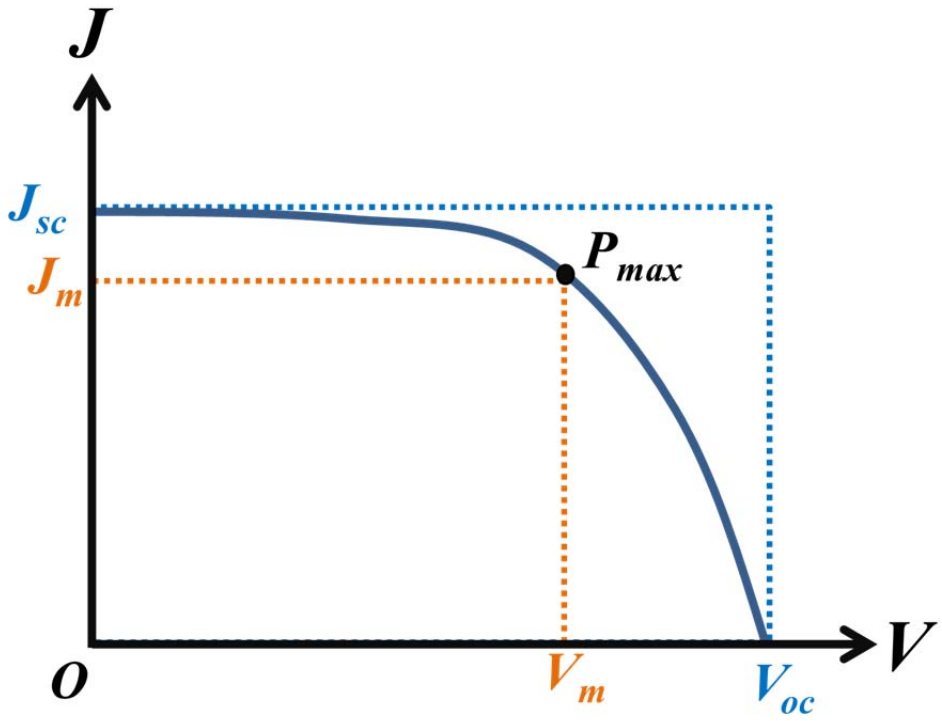

Figure 1.5 Schematic representation of the typical J-V curve under illumination. The ratio $J_mV_m/J_{sc}V_{oc}$ is the fill factor which is graphically indicated by two rectangles in blue and orange colors.

1.2.2 Issues for the enhancement of the power conversion efficiency

Photoelectrochemical solar energy conversion processes occurring in DSSCs are thoroughly summarized in numerous references.[45,47,62] The widely accepted steps are 'light harvesting' of incident photons followed by the 'charge injection' from the dye molecules to the TiO_2 nanoparticle network, and charge collection processes. [45, 47, 48, 65,66]

The light harvesting efficiency (LHE) is related to the photon absorption process by the dye molecules. So, for higher LHE, optimized nanoparticle networks of supporting metal

oxide semiconductor (typically TiO_2) should load a sufficient amount of dyes for maximized absorption. Currently, the light absorption of sensitized TiO_2 film of typical thickness (10μm~) at the absorption peak of dye molecules (N3 or N719) reaches close to unity.[45,66] It also depends on the characteristics of the dye species: there are several brilliant advances in developing new dye molecules absorbing more photons over a wider sunlight spectrum, e.g. N3,[48] N719,[50] Black dye,[49] and C101.[52] In summary, high LHE is achieved by the combination of the optimized nanostructure accommodating as much dyes as possible and good dye molecules which can absorb more photons over wide wavelength range. There have been efforts to enhance LHE through the application of photonic crystal structures which can reflect unabsorbed photons back to the sensitized TiO_2 layer and increase the chance of additional absorbtion.[59,61,67] The DSSCs combined with the photonic crystal structure will be discussed in the separate section later.

The charge injection efficiency (CIE) is the quantum yield for charge injection,[47] i.e. the efficiency of the photoelectron injection from the dye molecule into the nanoparticle network of the metal oxide semiconductors. According to Grätzel,[45] the electronically excited dye state is deactivated so quickly (with a rate of 10^3~10^{10} s^{-1}), that charge injection should occur about 100 times faster than the deactivation process. Indeed, the well-developed dye molecules like commercially available N3 and/or N719 also have CIEs close to unity,[48,51,66] which means that charge injection occurs in picoseconds, i.e. with a rate of 10^{12} s^{-1}.[45]

The charge collection efficiency (CCE) is the efficiency of collecting injected electrons.[47] Injected electrons travel along the complex network of TiO_2 nanoparticles which is surrounded by the electrolyte containing iodide/triiodide redox couples and cations. Many researchers pointed out that the nature of electron movement in the TiO_2 network is not the

drift, but the diffusional process due to the shielding of Coulomb potential of electrons by the cations in the electrolyte which in turn, prevents the formation of the electric field in the mesoporous TiO_2 film that enables charge drift.[68] Some researchers showed that diffusing electrons spend 10^{-3} to 10^{0} seconds in the nanoparticle network experiencing trap/detrap processes of ~10^{6} times before harvested by the FTO layer.[69] Most of the trap states are provided by the interfacial defects between nanoparticles, and electron back transfer occurs mainly from the trap states of the nanoparticle network to the I_3^- ions in the electrolyte.[44] Moreover, even after collected by the FTO layer, electron back transfer can occur from the FTO layer to the electrolyte.[63] These electron back transfer pathways give basic ideas on how to improve the CCE: cover the FTO layer with a dense barrier coating,[54,66,70,71] and/or form TiO_2 structures with less interfacial defects, and/or reduce the diffusion length of electrons to the TCO.[44,66] $TiCl_4$ treatment has been reported as an effective method for forming a dense TiO_2 barrier coating on the FTO layer in order to suppress electron back transfer.[48,70,72-74] In an effort to reduce the diffusion length from the charge generation point to the FTO as well as the number of interfacial defects, TiO_2 layers comprised of 1-dimensional (1D) geometry were reported in the form of nanowires[73,74] and nanotubes.[75,76] Nevertheless, as these 1D geometries inevitably have reduced surface area for the dye monolayer, their overall power conversion efficiencies were not comparable to that of conventional random nanoparticle networks.[44] So, in order to take advantage of both aligned geometries and the mesoporous morphology, branched structures were developed such as nanotripods,[77] nanoflowers,[78] and nanoforests.[79,80] Additionally, alterations of the DSSC structures aimed at minimization of the diffusion length to the TCO were reported in the form of conformal, thin TiO_2 layers[69,81] and patterned electrode structures.[66]

1.2.3 Photonic crystal (PC) structures

A photonic crystal is a periodic optical structure on the wavelength scale (several hundred nanometers) which can control the propagation of photons.[82] Joannopoulos et al.[83] used an analogy to explain the nature of photonic crystals: just as periodic electrostatic potentials of atoms can control the propagation of electrons in the crystals, periodic array of refractive index contrast on the wavelength-scale can alter the propagation of photons. Figure 1.6 shows the analogy between electronic bandstructure of Si atoms in diamond structure and photonic bandstructure of dielectric particles (ε=12) in a diamond structure.[83]

Photonic crystals originate from the work of Yablonovitch[84] and John[85] in 1987. Historically, Lord Rayleigh observed a photonic band gap from a 1-dimensional stacking of aternative refractive index materials,[82,83] as shown in Figure 1.7 (left).[82] This phenomenon is actually very frequently found in nature, e.g. iridescence of butterfly wings.[83] However, Yablonovitch and John's work showed the extension of the photonic band gap concept to more than 1-dimension, and successfully drew strong attention from researchers. Since then, researcher have focused on finding new 2- or 3-dimensional (3D) photonic crystal structures that can be realized with available fabrication methods.[83] The center and right images of Figure 1.7 are conceptual representations of 2D and 3D photonic crystals, respectively.[82,86]

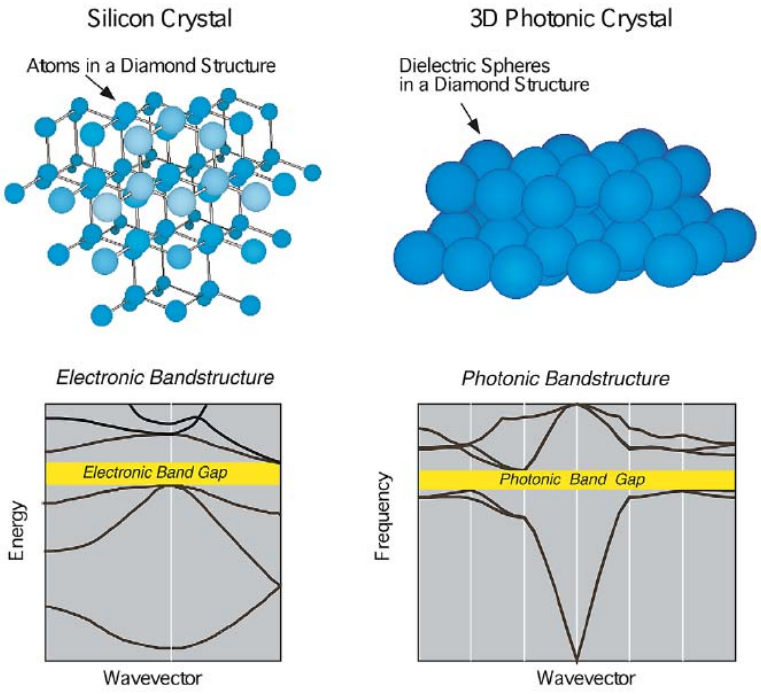

Figure 1.6 Electronic bandstructure of Si atoms in diamond structure (left) and photonic bandstructure of dielectric spheres in diamond structure showing the analogy of control of electron motion in the periodic electrostatic potential and photons in the periodic refractive index contrast. (Reprinted with permission from reference 83. Copyright © 2003 Elsevier Ltd.)

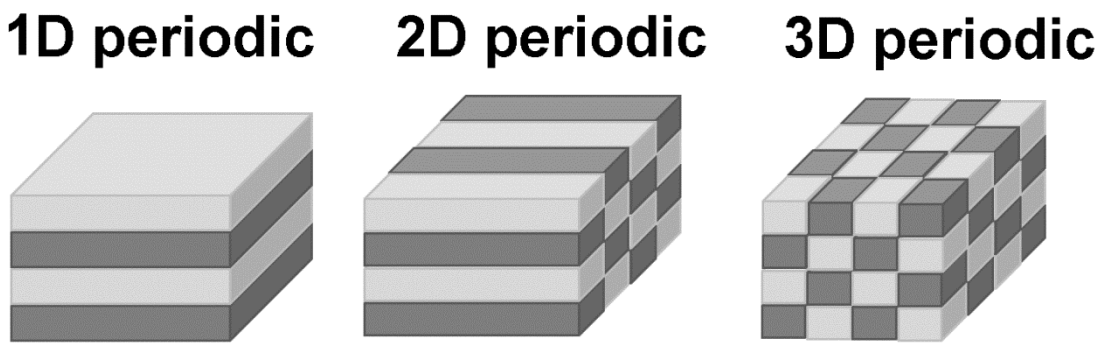

Figure 1.7 Exemplary representation of the 1D, 2D, and 3D photonic crystal structures showing the two repeating unit of different refractive indices conceptually. (Redrawn following the reference 86.)

Historically, the realization of a complete photonic band gap with 3D structures of high refractive index materials like Si has been challenging requiring expensive, multistep photolithographic techniques that depend on 'top-down' approaches.[82] The self-assembly of colloidal building blocks provided a much easier way to fabricate 3D photonic crystal structures.[87] One of the most popular 3D photonic crystal structures of this type is the inverse opal structure,[88] which is the inverse structure of a FCC array of monodisperse particles. Figure 1.8[88] shows an inverse opal 3D photonic crystal and the resultant optical characteristics. As shown in the figure, at the wavelength corresponding to the photonic band gap, an abrupt drop of transmission and an increase in reflection can be seen. So, if the inverse opal photonic crystal layer is combined with a sensitized mesoporous TiO_2 layer in the DSSC, photons that are not absorbed (or harvested) by the sensitized TiO_2 layer cannot propagate through the photonic crystal layer but are reflected back to the sensitized layer and can be "reused."[59-61]

In DSSCs, polystyrene (PS) is the popular material for the FCC array, because once the FCC array is formed, it is easy to make the inverse structure by filling the interstitial spaces between PS spheres with oxide precursors and then removing the PS by calcination.[59,61] Bilayer structures of inverse opal photonic crystal in conjuction with a sensitized TiO_2 mesoporous layer[59-61] is the typical architecture in the photonic crystal DSSCs. Figure 1.9[61] shows the complex multistep processing required to build such an architecture. By changing the diameter of the PS spheres, one can easily tune the photonic band gap wavelength[61] to enhance the LHE of the wavelength region where the intrinsic absorption of the dye molecule is weak.[59,61] However, the complex multistep process for fabricating the bilayer structure has prevented researchers from applying inverse opal

photonic crystal structures easily to the DSSCs, and has been the source of interfacial defects at the sensitized TiO_2/inverse opal layer interface. So, the usefulness of light scattering inverse opal layer has been controversial[59-61] and reports dealing with a sufficient number of samples—enough for statistics need to confirm the enhancement of the power conversion efficiency by photonic crystals—are rare in the literature.[61] So, there is a strong demand for new photonic crystal structures with simpler fabrication processes.

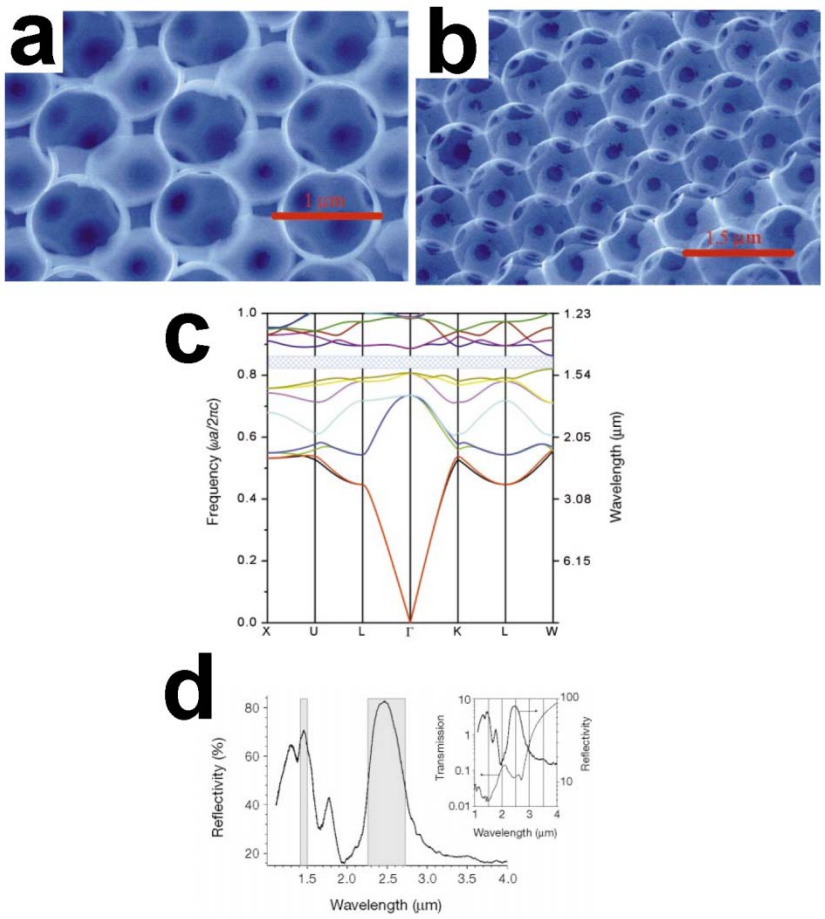

Figure 1.8 (a-b) SEM images of Si 3D inverse opal structures. (c) Calculated photonic bandstructure of Si inverse opal showing photonic band gaps in 1.5 and 2.5μm. (d) Optical measurement exhibiting photonic band gaps at predicted wavelength region.(Reprinted by permission from reference 88. Copyright 2000 © Macmillan Publishers Ltd)

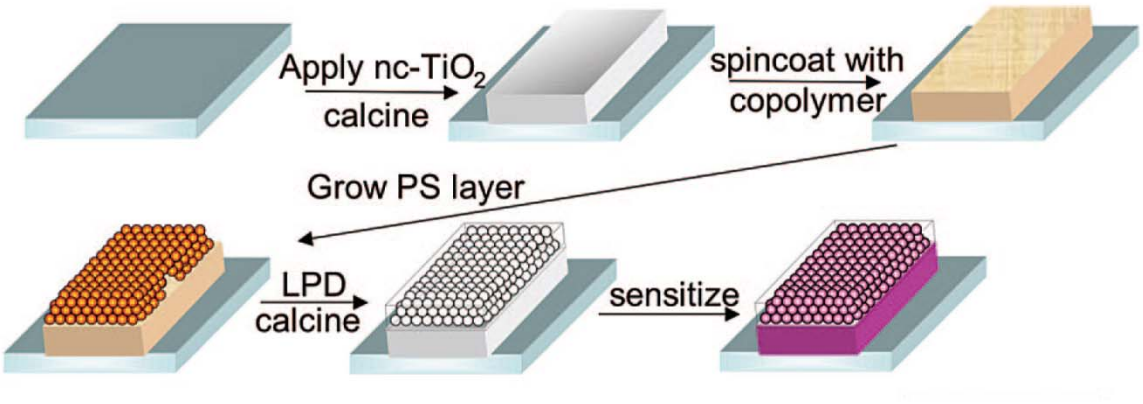

Figure 1.9 Complex multistep processes for building inverse opal/mesoporous TiO_2 bilayer structure. (Reprinted by permission from reference 61. Copyright 2008 © American Chemical Society)

1.3 Scope of thesis

In section 1.1, I reviewed the history and challenges of conventional photolithography and their limitations when applied to the research outside of microelectronics, ie. in terms of cost and versatility of applicable materials. Soft-lithographic techniques which can be used to fabricate nanostructures and patterns with relative ease and at much lower cost by using reproduced elastomers were also introduced. As the soft-lithographic techniques are appropriate to deal with liquids and viscous pastes to fill the replica patterns in the elastomer, they can be adapted to build special nano/micro structures in the DSSCs by just slightly modifying the conventional doctor blading process.

In section 1.2, the operation principles of DSSCs and related issues were introduced in terms of light harvesting, charge injection, and charge collection issues. Basic principles needed to enhance the CCE were discussed based on those working mechanisms, and then photonic crystals were also reviewed as candidate structures to enhance the LHE of DSSCs. However, as the conventional bilayer structures based on the inverse opal layer depend on

complex, multi-step processes, a new photonic crystal structure which can be built by simpler methods with good structural integrity is worth pursuing.

Consequently, in this thesis, I suggest new architectures for DSSCs that aim to increase the solar energy conversion efficiency. The modified DSSC structures focus on the improvement of the LHE and CCE, and most importantly easier fabrication of those structures. For modification of the conventional DSSC structures, I apply soft-lithographic techniques based on the PFPE elastomers.

In chapter 2 and 3, I suggest surface patterns for simpler photonic crystal geometries. As surface patterns can simply be built on the conventional mesoporous TiO_2 or other metal oxide semiconductor layer by adding just one more step using the identical oxide paste, a seamless photonic crystal structure with the conventional DSSCs can be fabricated without major structural alterations. In chapter 2, Nb_2O_5 was used for the supporting mesoporous nanoparticle network, with a thickness around 3μm, which is about 30% of the conventional sensitized layer thickness of DSSCs. Fabricated nanostructures were discussed focusing on their nanostructures and optical behavior in terms of LHE enhancement. IPCE was used as a measure of solar energy conversion efficiency. In chapter 3, TiO_2 nanoparticle networks were used for light harvesting media. Surface patterns were fabricated to form photonic crystal geometries by adapting soft-lithography methods. Characterization of the surface patterned photoanodes focus on the optical behavior of surface patterned structures and their solar energy conversion by IPCE and ***J-V*** measurements.

In chapter 4, structural modification of the TCO was introduced in patterned ITO substructures for enhancing CCE. The ITO substructures were formed on a micrometer scale comparable to the typical thickness of the sensitized TiO_2 layers in order to minimize

electron diffusion pathways to the TCO electrode. The effects of ITO substructures on the DSSC performances were analyzed in terms of their morphology, optical change of the photoanode, and solar energy conversion efficiency in IPCE and ***J-V*** measurements. Electrochemical impedance spectroscopy (EIS) was used to elucidate the characteristics of the DSSC structure with embedded ITO patterns and suggestions were made based on the integrated characterizations.

1.4 References

(1) Pease, R. F.; Chou, S. Y. *Proc. IEEE* **2008**, *96*, 248–270.

(2) Moore, G. E. *Electronics* **1965**, *38*, 114ff.

(3) Vijayakrishnan, V.; Chainani, A.; Sarma, D. D.; Rao, C. N. R. *J. Phys. Chem.* **1992**, *96*, 8679–8682.

(4) Likharev, K. K.; Claeson, T. *Sci. Am.* **1992**, *269*, 80–85.

(5) Ekimov, A. I.; Onushchenko, A. A. *JETP Lett.* **1982**, *34*, 345–349.

(6) Chestnoy, N.; Harris, T. D.; Hull, R.; Brus, L. E. *J. Phys. Chem.* **1986**, *90*, 3393–3399.

(7) Reed, M. A. *Sci. Am.* **1993**, *268*, 118–123.

(8) Alivisatos, A. P. *Science* **1996**, *271*, 933–937.

(9) Ko, D.-H.; Tumbleston, J. R.; Henderson, K. J.; Euliss, L. E.; DeSimone, J. M.; Lopez, R.; Samulski, E. T. *Soft Matter* **2011**, *7*, 6404–6407.

(10) Truskett, V. N.; Watts, M. P. C. *TRENDS in Biotech.* **2006**, *24*, 312–317.

(11) Plass, R.; Pelet, S.; Krüger, J.; Grätzel, M.; Bach, U. *J. Phys. Chem. B* **2002**, *106*, 7578–7580.

(12) Nozik, A. J. *Next Gener. Photo*V*oltaics* **2004**, 196–222.

(13) Okazaki, S. *J. Vac. Sci. Technol. B* **1991**, *9*, 2829–2833.

(14) Xia, Y.; Whitesides, G. M. *Angew. Chem. Int. Ed.* **1998**, *37*, 550–575.

(15) Levenson, M. D.; Viswanathan, N. S.; Simpson, R. A. *IEEE Trans. Electron Devices* **1982**, *ED-29*, 1828–1836.

(16) Owa, S.; Nagasaka, H.; Nakano, K.; Ohmura, Y. *Proc. SPIE* **2006**, *6154*, 615408.

(17) Sewell, H.; Mulkens, J.; McCafferty, D.; Markoya, L.; Streefkerk, B.; Graeupner, P. *Proc. SPIE* **2006**, *6154*, 615406.

(18) Menon, R.; Smith, H. I. *J. Opt. Soc. Amer.* **2006**, *A23*, 2290–2294.

(19) Herriott, D. R.; Collier, R. J.; Alles, S.; Stafford, J. W. *IEEE Trans. Electron Devices* **1975**, *ED-22*, 385–392.

(20) Warlaumont, J. *J. Vac. Sci. Technol.***1989**, B7, 2934–2938.

(21) Kaesmaier, R.; Löschner, H.; Stengl, G.; Wolfe, J. C.; Ruchhoeft, P. *J. Vac. Sci. Technol.* **1999**, *B17*, 3091–3097.

(22) Martian, C.R.K.; Snow, E.S. *Microelectron. Eng.* **1996**, *32*, 173–189.

(23) Wilbur, J. L.; Kumar, A.; Kim, E.; Whitesides, G. M. *Adv. Mater.* **1994**, *6*, 600–604.

(24) Li, H.-W.; Muir, B. V. O.; Fichet, G.; Huck, W. T. S. *Langmuir* **2003**, *19*, 1963–1965.

(25) Ko, D.-H.; Tumbleston, J. R.; Zhang, L.; Williams, S.; DeSimone, J. M.; Lopez, R.; Samulski, E. T. *Nano Lett.* **2009**, *9*, 2742–2746.

(26) Wise, K. D.; Najafi, K. *Science* **1991**, *254*, 1335–1342.

(27) Service, R. E. *Science* **1995**, *268*, 26–27.

(28) Lee, S. S.; Lin, L. Y.; Wu, M. C. *Appl. Phys. Lett.* **1995**, *67*, 2135–2137.

(29) Xia, Y.; Whitesides, G. M. *Annu. Rev. Mater. Sci.* **1998**, *28*,153–184.

(30) Choi, S. J.; Yoo, P. J.; Baek, S. J.; Kim, T. W.; Lee, H. H. *J. Am. Chem. Soc.* **2004**, *126*, 7744–7745.

(31) Kim, Y. S.; Lee, H. H.; Hammond, P. T. *Nanotechnology* **2003**, *14*, 1140–1144.

(32) Khang, D.-Y.; Lee, H. H. *Langmuir* **2004**, *20*, 2445–2448.

(33) Resnick, P. R.; Buck, W. H. In *Fluoropolymers vol. 2: Properties*; Hougham, G., Cassidy, P. E., Johns, K., Davidson, T., Eds.; Kluwer Academic Publisher: New York, 1999.

(34) Csucs, G.; Kunzler, T.; Feldman, K.; Robin, F.; Spencer, N. *Langmuir* **2003**, *19*, 6104– 6109.

(35) Pisignano, D.; D'Amone, S.; Gigli, G.; Cingolani, R. *J. Vac. Sci. Technol. B* **2004**, *22*, 1759–1763.

(36) Rolland, J. P.; Van Dam, R. M.; Schorzman, D. A.; Quake, S. R.; DeSimone, J. M. *J. Am. Chem. Soc.* **2004**, *126*, 2322–2323.

(37) Rolland, J. P.; Hagberg, E. C.; Denison, G. M.; Carter, K. R.; DeSimone, J. M. *Angew. Chem., Int. Ed.* **2004**, *43*, 5796–5799.

(38) Williams, S. S.; Retterer, S.; Lopez, R.; Ruiz, R.; Samulski, E. T.; DeSimone, J. M. *Nano Lett.* **2010**, *10*, 1421–1428.

(39) Zhao, X.-M.; Xia, Y.; Whitesides, G. M. *Adv. Mater.* **1996**, *8*, 837–840.

(40) Xia, Y.; Kim, E.; Zhao, X.-M.; Rogers, J. A.; Prentiss, M.; Whitesides, G. M. *Science* **1996**, 273, 347–349.

(41) Kim, E.; Xia, Y.; Zhao, X.-M.; Whitesides, G. M. *Adv. Mater.* **1997**, *9*, 651–654.

(42) Kim, E.; Xia, Y.; Whitesides, G. M. *Nature* **1995**, *376*, 581–584.

(43) Kumar, A.; Whitesides, G. M. *Appl. Phys. Lett.* **1993**, *63*, 2002–2004.

(44) Zhang, Q.; Cao, G. *Nano Today* **2011**, *6*, 91–109.

(45) Grätzel, M. *Inorg. Chem.* **2005**, *44*, 6841–6851.

(46) National Renewable Energy Laboratory (NREL) home page (http://www.nrel.gov/ncpv/images/efficiency_chart.jpg)

(47) O'Regan, B.; Grätzel, M. *Nature* **1991**, *335*, 737–740.

(48) Nazeeruddin, M. K.; Kay, I.; Rodicio, A.; Humphry-Baker, R.; Müller, E.; Liska, P.; Vlachopouloss, N.; Grätzel, M. *J. Am. Chem. Soc.* **1993**, *115*, 6382–6390.

(49) Nazeeruddin, M. K.; Pechy, P.; Grätzel, M. *Chem. Commun.***1997**, 1705–1706.

(50) Nazeeruddin, M.K.; Zakeeruddin, S.M.; Humphry-Baker, R.; Jirousek, M.; Liska, P.; Vlachopoulos, N.; Shklover, V.; Fischer, C.H.; Grätzel, M. *Inorg. Chem.* **1999**, *38*, 6298–6305.

(51) Wang, P.; Klein, C.; Humphry-Baker, R.; Zakeeruddin, S.; Grätzel, M. *J. Am. Chem. Soc.* **2005**, *127*, 808–809.

(52) Gao, F.; Wang, Y.; Shi, D.; Zhang, J.; Wang, M. K.; Jing, X. Y.; Humphry-Baker, R.; Wang, P.; Zakeeruddin, S. M.; Grätzel, M. *J. Am. Chem. Soc.* **2008**, *130*, 10720–10728.

(53) Huang, S. Y.; Schlichthörl, G.; Nozik, A. J.; Grätzel, M.; Frank, A. J. *J. Phys. Chem. B* **1997**, *101*, 2576–2582.

(54) Kopidakis, N.; Neale, N. R.; Frank, A. J. *J. Phys. Chem. B* **2006**, *110*, 12485–12489.

(55) Yella, A.; Lee, H.-W.; Tsao, H. N.; Yi, C.; Chandrian, A. K.; Nazeeruddin, M. K.; Diau, E. W.-G.; Yeh, C.-Y.; Zakeeruddin, S. M.; Grätzel, M. *Science* **2011**, *334*, 629–634.

(56) Burschka, J.; Pellet, N.; Moon, S.-J.; Humphry-Baker, R.; Gao, P.; Nazeeruddin, M. K.; Grätzel, M. *Nature* **2013**, *499*, 316–320.

(57) Tseng, Y.-H.; Kuo, C.-S.; Huang, C.-H.; Li, Y.-Y.; Chou, P.-W.; Cheng, C.-L.; Wong, M.-S. *Nanotechnology* **2006**, *17*, 2490–2497.

(58) Bach, U.; Lupo, D.; Comte, P.; Moser, J. E.; Weissörtel, F.; Salbeck, J.; Spreitzer, H.; Grätzel, M. *Nature* **1998**, *395*, 583–585.

(59) Guldin, S.; Hüttner, S.; Kolle, M.; Welland, M. E.; Müller-Buschbaum, P.; Friend, R. H.; Steiner, U.; Tétreault, N. *Nano Lett.* **2010**, *10*, 2303–2309.

(60) Mihi, A.; Míguez, H. *J. Phys. Chem. B* **2005**, *109*, 15968–15976.

(61) Lee, S.-H. A.; Abrams, N. M.; Hoertz, P. G.; Barber, G. D.; Halaoui, L. I.; Mallouk, T. E. *J. Phys. Chem. B* **2008**, *112*, 14415–14421.

(62) Yum, J.-H.; Baranoff, E.; Kessler, F.; Moehl, T.; Ahmad, S.; Bessho, T.; Marchioro, A.; Ghadiri, E.; Moser, J.-E.; Yi, C.; Nazeeruddin, M. K.; Grätzel, M. *Nature Comm.* **2012**, *3*, 631.

(63) Cameron, P. J.; Peter, L. M. *J. Phys. Chem. B* **2005**, *109*, 7392–7398.

(64) Jain, A.; Kapoor, A. *Solar Energy Mater. Solar Cells,* **2005**, *86,* 391–396.

(65) Kopidakis, N.; Schiff, E. A.; Park, N.-G.; van de Lagemaat, J.; Frank, A. J. *J. Phys. Chem. B* **2000**, *104*, 3930–3936.

(66) Yang, Z.; Xu, T.; Gao, S.; Welp, U.; Kwok, W.-K. *J. Phys. Chem. C* **2010**, *114*, 19151–19156.

(67) Colodrero, S.; Mihi, A.; Häggman, L.; Ocaña, M.; Boschloo, G.; Hagfeldt, A.; Míguez, H. *Adv. Mater.* **2009**, *21*, 764–770.

(68) van de Lagemaat, J.; Park, N.-G.; Frank, A. J. *J. Phys. Chem. B* **2000**, *104*, 2044–2052.

(69) Yang, Z.; Gao, S.; Li, T.; Liu, F.-Q.; Ren, Y.; Xu, T. *ACS Appl. Mater. Interfaces* **2012**, *4*, 4419–4427.

(70) Kavan, L.; O'Regan, B.; Kay, A.; Grätzel, M. *J. Electroanal. Chem.* **1993**, *346*, 291–307.

(71) Cameron, P. J.; Peter, L. M. *J. Phys. Chem. B* **2003**, *107*, 14394–14400.

(72) Barbe, C. J.; Arendse, F.; Comte, P. *J. Am. Ceram. Soc.* **1997**, *80*, 3157–3171.

(73) Park, N.-G.; Schlichthörl, G.; van de Lagemaat, J.; Cheong, H. M.; Mascarenhas, A.; Frank, A. J. *J. Phys. Chem. B* **1999**, *103*, 3308–3314.

(72) Ito, S.; Liska, P.; Comte, P.; Charvet, R. L.; Péchy, P.; Bach, U.; Schmidt-Mende, L.; Zakeeruddin, S. M.; Kay, A.; Nazeeruddin, M. K.; Grätzel, M. *Chem. Commun.* **2005**, 4351–4353.

(73) Law, M.; Greene, L. E.; Johnson, J. C.; Saykally, R.; Yang, P. D. *Nature Mater.* **2005**, *4*, 455–459.

(74) Feng, X. J.; Shankar, K.; Varghese, O. K.; Paulose, M.; Latempa, T. J.; Grimes, C.A. *Nano Lett*. **2008**, *8*, 3781–3786.

(75) Zhu, K.; Neale, N.; Miedaner, A.; Frank, A. *Nano Lett.* **2002**, *7*, 69–74.

(76) Gong, D.; Grimes, C. A.; Varghese, O. K.; Hu, W. C.; Singh, R. S.; Chen, Z.; Dickey, E. C. *J. Mater. Res.* **2001**, *16*, 3331–3334.

(77) Chen, W.; Zhang, H. F.; Hsing, I. M.; Yang, S. H. *Electrochem. Commun.* **2009**, *11*, 1057–1060.

(78) Jiang, C. Y.; Sun, X. W.; Lo, G. Q.; Kwong, D. L.; Wang, J. X. *Appl. Phys. Lett.* **2007**, *90*, 263501.

(79) Sauvage, F.; Di Fonzo, F.; Li Bassi, A; Casari, C. S.; Russo, V.; Divitini, G.; Ducati, C.; Bottani, C. E.; Compte, P.; Gratzel, M. *Nano Lett.* **2010**, *10*, 2562–2567.

(80) Ghosh, R.; Hara, Y.; Alibabaei, L.; Hanson, K.; Rangan, S.; Bartynski, R.; Meyer, T. J.; Lopez, R. *ACS Appl. Mater. Interfaces* **2012**, *4*, 4566–4570.

(81) Martinson, A. B. F.; Elam, J. W.; Liu, J.; Pellin, M. J.; Marks, T. J.; Hupp, J. T. *Nano Lett.* **2008**, *8*, 2862–2866.

(82) Von Freymann, G.; Kitaev, V.; Lotsch, B. V.; Ozin, G. A. *Chem. Soc. Rev.* **2013**, *42*, 2528–2554.

(83) Johnson, S. G.; Joannopoulos, J. D. *Acta Mater.* **2003**, *51*, 5823–5835.

(84) Yablonovitch, E. *Phys. Rev. Lett.* **1987**, *58*, 2059–2062.

(85) John, S. *Phys. Rev. Lett.* **1987**, *58*, 2486–2489.

(86) Joannopoulos, J. D.; Johnson, S. G.; Winn, J. N.; Meade, R. D. *Photonic Crystals: Molding the Flow of Light*, 2nd Ed.; Princeton University Press: Princeton, NJ and Oxford, UK, 2008.

(87) Ozin, G. A.; Hou, K.; Lotsch, B. V.; Cademartiri, L.; Puzzo, D. P.; Scotognella, F.; Ghadimi, A.; Thomson, J. *Mater. Today* **2009**, *12 (5)*, 12–23.

(88) Blanco, A.; Chomski, E.; Grabtchak, S.; Ibisate, M.; John, S.; Leonard, S. W.; Lopez, C.; Meseguer, F.; Miguez, H.; Mondia, J. P.; Ozin, G. A.; Toader, O.; van Driel, H. M. *Nature* **2000**, *405*, 437–440.

CHAPTER 2

SURFACE PATTERNING OF MESOPOROUS NIOBIUM OXIDE FILMS FOR SOLAR ENERGY CONVERSION

2.1 Introduction

Since the first report of a high efficiency (~7.1%) dye sensitized solar cell (DSSC) by O'Regan and Grätzel,[1] the DSSC has been promoted as a promising photovoltaic technology with lower intrinsic costs compared to conventional Si-based photovoltaic devices. Subsequently, extensive and intensive research has focused on improving DSSC efficiency, mainly by the development of new dye molecules absorbing over a wider spectrum of light,[2,3] novel electrolytes,[4-6] the design and optimization of cell nanostructures (e.g. tubular[7,8] or nanoforests[9] of TiO_2), and new metal oxides and/or doped materials in addition to titania for dye supports.[10-13] Niobium oxide has been a candidate in those efforts to replace TiO_2, especially noteworthy for its higher conduction band energy,[11,14-17] which can be a benefit in principle by generating a higher open circuit voltage.[18] Recently, a high conversion efficiency (4.1%) cell having only a 4μm thick Nb_2O_5 nanoporous network was reported.[19]

This chapter is reproduced with permission from Myoung-Ryul Ok, Rudresh Ghosh, M. Kyle Brennaman, Rene Lopez, Thomas J. Meyer, and Edward T. Samulski

ACS Appl. Mater. Interfaces **2013**, *5*, 3469-3474.

Another application of niobium oxide with its higher conduction band energy is a shell material of the TiO_2/Nb_2O_5 core/shell structured DSSCs, forming an energy barrier to lower the recombination loss.[20,21] Along with the efforts to apply niobium oxide to DSSCs and produce photocurrents, other approaches are underway to use niobium oxide as the wide band gap semiconductor electrode for solar fuel production, e.g. hydrogen generation with the dye-sensitized photo-electrochemical cells (DSPECs).[22] An additional variable to exploit to obtain better performance with existing materials is to utilize optical structures within the DSSCs for improving photon absorption and photocurrent generation.[23-31] These optical elements have been utilized extensively in TiO_2 based DSSCs. Utilizing for instance additional layer of larger TiO_2 particles for effective scattering that confines light in the dye-sensitized mesoporous TiO_2 layer,[23] or including a photonic crystal (PC) layer on top of the conventional mesoporous TiO_2 film for forming a photonic stop band and reflecting unabsorbed photons back to the mesoporous TiO_2 layer.[24-31] In some particularly effective cases, 3-dimensional (3-D) opal-like structures formed with monodisperse polystyrene (PS) beads were employed to create the photonic crystal layer.[24-30] This structure is advantageous because one can easily choose the photonic stop band wavelength by simply selecting the diameter of the PS beads, especially targeting the red region where intrinsic photon absorption by the dye molecules is weak.[29] However, despite the benefits of the inverse opal based bilayer structures, its construction is a complex multistep processes, limiting the practical application of PC structures to the DSSCs. Actual enhancements in cell efficiency with good reproducibility are rare.[30] Although 2-dimensional (2-D) PC structures are not as effective as the 3-D PCs which form a complete photonic band gap (PBG),[32] 2-D PCs in the form of surface patterning by soft-lithography[33] can be an alternative approach, considering

the easy and simple methods to fabricate them, and 2-D PCs have been applied to organic photovoltaic devices[34] and solid state DSSCs.[35]

Herein, I demonstrate a simple surface patterning method based on the soft-lithographic techniques to form PC structures on the nanocrystalline niobium oxide film surface. A photo-curable perfluoropolyether (PFPE)[36,37] was used to replicate 2-D patterns on a Si master and reproduce them on the surface of mesoporous niobium oxide anodes; the method exploits the low surface energy and high gas permeability of PFPE.[38] Optical characteristics and solar energy conversion performances of the surface patterned niobium oxide films were analyzed and compared to flat niobium oxide anodes.

2.2 Experimental

2.2.1 Preparation of the niobium oxide paste via sol-gel synthesis

Mesoporous nanocrystalline niobium oxide films were prepared on FTO coated glass substrates via a sol-gel route. 1.255ml (0.005mol) of niobium ethoxide ($Nb(OEt)_5$, 99.95%, Aldrich) was dissolved in 10ml of ethanol, and 1ml of this mixture was hydrolyzed with 0.3ml of ammonium hydroxide solution (29.53%, Fisher Scientific). After hydrolysis, 1ml of glacial acetic acid (99.9%, Fisher Scientific) was added to the hydrolyzed mixture, sonicated, and stirred overnight for peptization. To this niobium oxide mixture, 1.7ml of hydroxypropyl cellulose (M_w: 100,000, Aldrich) solution in deionized water (10wt%) was added and well mixed by stirring overnight. The as-prepared paste was used for mesoporous niobium oxide base layer and condensed paste was used for additional surface patterning on top of the base layer.

2.2.2 Preparation of the patterned PFPE mold

For surface patterning on top of the calcined niobium oxide films by soft-lithography, patterned polymeric mold was prepared by following the method reported by Hampton et al.[39]: Photocurable PFPE solution (a solution consisting of 1000g/mol PFPE α,Ω–functionalized dimethacrylate and 2,2-diethoxyacetophenone as the photo-initiator) was poured and spread evenly onto a patterned Si-wafer. The surface pattern used was an arbitrarily chosen 2-dimensional hexagonal array of cylindrical posts (200nm(D)×200nm(H)) with 400nm periodicity which was anticipated to exhibit observable effects in the visible wavelength range. After purging with N_2 gas for 3min, PFPE was polymerized on a Si patterns by radiating UV light for 3min. The photo-cured PFPE film was carefully removed from the Si master and rinsed with ethanol to remove uncrosslinked residues on the PFPE film. Si wafer grade flat PFPE films were also made by using a non-patterned, flat Si wafer for preparing non-patterned niobium oxide anodes as a control.

2.2.3 Fabrication of mesoporous patterned niobium oxide films

FTO coated glass substrates (15Ω/sq, 2.3mm thick, Hartford glass) were sonicated in acetone (99.5%, Fisher Scientific), isopropanol (99.9%, Fisher Scientific), and deionized water for 20min respectively and then heat-treated at 500°C in the air for 10min to completely remove organic residues before coating the niobium oxide paste. Niobium oxide paste was dropped onto FTO coated glass substrate districted by the tape spacers (3M), dried on a hot plate (80°C), and then calcined in a tube furnace to 600°C (2K/min) with mild air stream.

Figure 2.1 summarizes the steps for fabricating surface patterned niobium oxide films: On top of these flat and patterned PFPE films, a very small amount of condensed niobium oxide paste was spread evenly. Then, the PFPE molds with very thin paste layer

were put onto the calcined niobium oxide layer (Figure 2.1 (a), (b)). Mild pressure was exerted to the calcined layer/additional paste layer/PFPE-mold assembly to ensure good mechanical contact among them during the drying step (in an 80°C oven). After sufficient drying, additional niobium oxide paste layer (dried, patterned or flat) and the calcined niobium oxide film got fused into a single solid entity (Figure 2.1 (c)). Then, the niobium oxide films with additional dried layer were calcined again in the tube furnace to 600°C (2K/min) with sufficient air stream.

2.2.4 Characterization of the nanostructure of the patterned niobium oxide

Crystallographic characterization was performed with X-ray diffraction (Rigaku MultiFlex X-ray diffractometer, Cu Kα radiation, 40kV-40mA, scan speed 4°/min) and a tunneling electron microscope (TEM, 100-CX, JEOL). Morphological information of the calcined niobium oxide films and surface patterns was obtained with a scanning electron microscope (SEM, S-4700, Hitachi). UV-visible absorption spectra were collected with an integration sphere (Cary 5000 fitted with DRA 2500). A surface profilometer (KLA Tencor P-6, scan speed: 50μm/s, scan length: 5mm) was used to measure the thickness of prepared films.

2.2.5 Evaluation of the solar energy conversion performances

To evaluate the solar energy conversion performance of flat and patterned niobium oxide films, prepared films were sensitized with N719 dye and assembled to DSSCs: N719 dye was dissolved to a 1:1 mixture of acetonitrile and t-butanol (0.2 mM), and the solution was then centrifuged to remove aggregates. Before sensitization, prepared niobium oxide films were heat treated (500°C for 30min) and cooled down to 80°C, and carefully submerged into the N719 dye solution. The films were sensitized overnight in the solution,

and rinsed with acetonenitrile to wash off unabsorbed portion of dye. The sensitized niobium oxide films were shaped to ~5mm×5mm with a razor blade. Sealed DSSCs were prepared basically following methods in the literature,[40] using a 100 μm Surlyn spacer and drilling one hole for electrolyte injection. The redox electrolyte used was a solution of 0.5 M LiI and 0.05 M I_2 in dry acetonitrile. A 75 W Xe Oriel 6251/Oriel Cornerstone 260 monochromator coupled with a Keithley 6517A current meter was used to measure the incident photon-to-current conversion efficiency (IPCE).

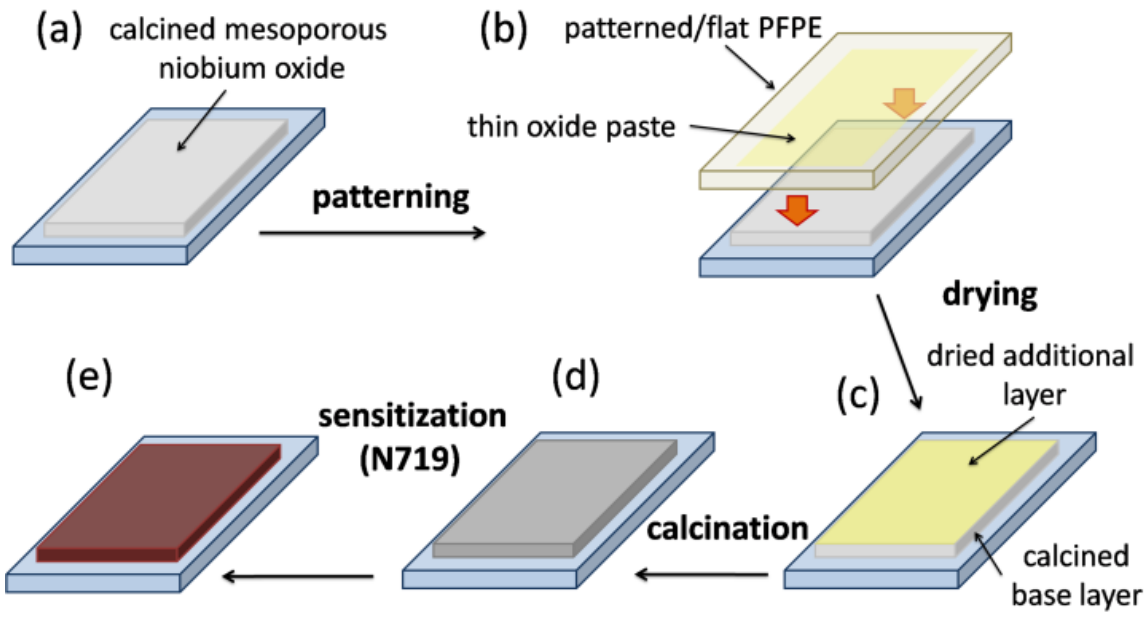

Figure 2.1 Procedure for forming mesoporous patterned niobium oxide film using a photo-cured PFPE mold.

2.3 Results and Discussion

2.3.1 Morphological analysis of the patterned niobium oxide films

The surface images of the calcined niobium oxide samples are shown in Figure 2.2. Patterns were well developed maintaining their original periodicity, 400 nm, as shown in Figure 2.2 (a). One can see that the diameter of the individual features is much smaller than 200 nm, the original diameter of the cylindrical posts on the Si master. As the patterns were made of a paste containing oxide nanoparticles and a polymeric additive, a large amount of shrinkage occurs during the calcinations by the removal of the residual solvent and polymeric phase and interconnection between oxide nanoparticles. However, even with the change in detailed shape of individual features relative to the original mold, the resulting surface structures exhibited the periodic 2-D spatial dimensions which constitute a PC geometry. The surface of the niobium oxide film revealed a mesoporous fine structure of around 10 nm (based on the smallest dimension) particles, as shown in Figure 2.2 (b). Note that the top surface shows only the nanostructures of an additional layer formed by patterning; that layer experienced the calcination process just once whereas the bulk of the niobium oxide base layer was calcined twice. In Figure 2.2 (c), one can clearly see the bilayer structure through a defective top layer. The dimensions of the base layer were much coarser than the top layer. To resolve the morphological discrepancy between the fine top layer and the coarse base layer, a monolayer with equivalent thermal history to the base layer (double calcinations with heating rate of 2K/min to 600°C) was prepared and observed with an SEM. As shown in Figure 2.2 (d), a layer with double calcination steps exhibited a bicontinuous mesoporous structure with coarser particle size about 20~40 nm, which matches well to the image of the base layer exposed in Figure 2.2 (c). The particles were so well connected that one cannot

discriminate individual nanoparticles from each other in the SEM images. This implies that the morphology of the base layer would have been like the fine structure of the top layer surface shown in Figure 2.2 (b) after the first calcination, and then became coarse and bicontinuous by the second calcination step. In terms of solar energy conversion, this coarser but bicontinuous nanostructure could be beneficial in electron transport, while detrimental to dye loading, in general.

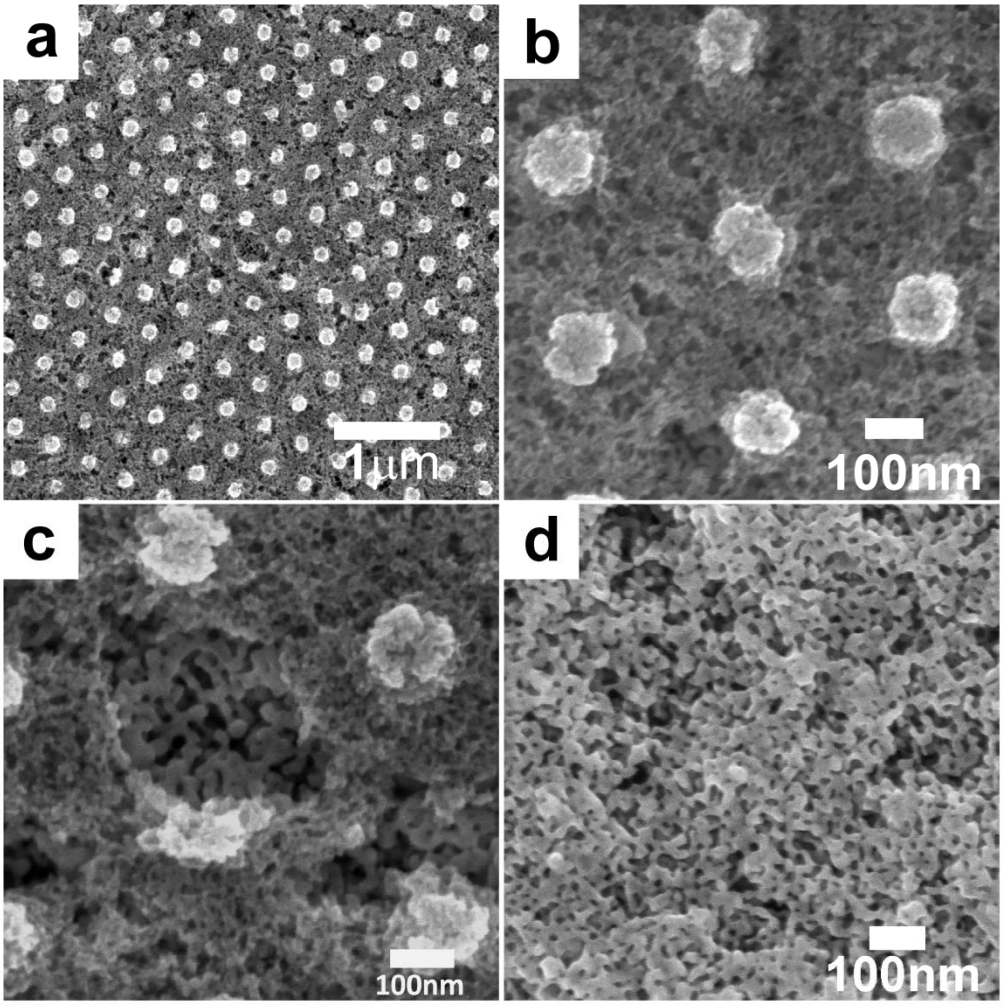

Figure 2.2 SEM images of the patterned niobium oxide films in different magnifications ((a)-(c)) exhibiting mesoporous surface morphology. The bilayer structure of the thin top layer on a coarser base layer is evident through a surface defect in the top layer in (c), and the morphology of the base layer achieved by calcining a film twice is shown in (d).

2.3.2 Crystallographic characterization of the patterned niobium oxide films

Crystallographic information of the niobium oxide films were analyzed with XRD and TEM. In Figure 2.3 (a), XRD data are shown. Considering the process conditions and resultant crystal structure in the literature,[22,41] it appears that the crystal structure of the prepared niobium oxide film is orthorhombic structure (JCPDS #27-1003). However, as shown in Figure 2.3 (a), most of the main peaks of both an orthorhombic and a hexagonal structure (JCPDS #28-0317) are so close that it is very difficult to identify one from the other solely by XRD from a thin film on a substrate. So, transmission electron microscopy (TEM) was used to collect more crystallographic evidence. Figure 2.3 (b) and (c) are TEM image of the niobium oxide particles and selected area electron diffraction (SAED) pattern of them prepared by grinding the niobium oxide film. The TEM image in Figure 2.3 (b) exhibited fragmented nanoparticles and larger globular structures together. Though the globular structures are an order of magnitude larger than the average particle size of the coarse base layer, they revealed many sections in contrast and looked like overlapped particles of several tens of nanometer. So, considering the SEM images shown in Figure 2.2, they are believed to be the globular flakes of the prepared oxide film which were the interconnected structure of the nanocrystalline niobium oxide particles. From the SAED pattern in Figure 2.3 (b), the crystal structure of the niobium oxide nanoparticles was identified as orthorhombic structure (T-phase) with a zone axis $[01\bar{8}]$. This matches well with the crystal structure and process conditions reported in the literature.[20,39] However, there exists discrepancy in the thermal history of the top and base layers and top layer is the most probable position where the residual low temperature hexagonal phase could exist. Figure 2.3 (c) is TEM image of the small ground structure and SAED pattern from it. Considering the size of the nanoparticles in

it, it is evident that the particle is a part of the top layer fired once. The SAED pattern in Figure 2.3 (c) was also identified as the orthorhombic structure with the same zone axis $[01\bar{8}]$. So, it can be concluded that both top and base layers consist of nanocrystalline orthorhombic niobium oxide particles.

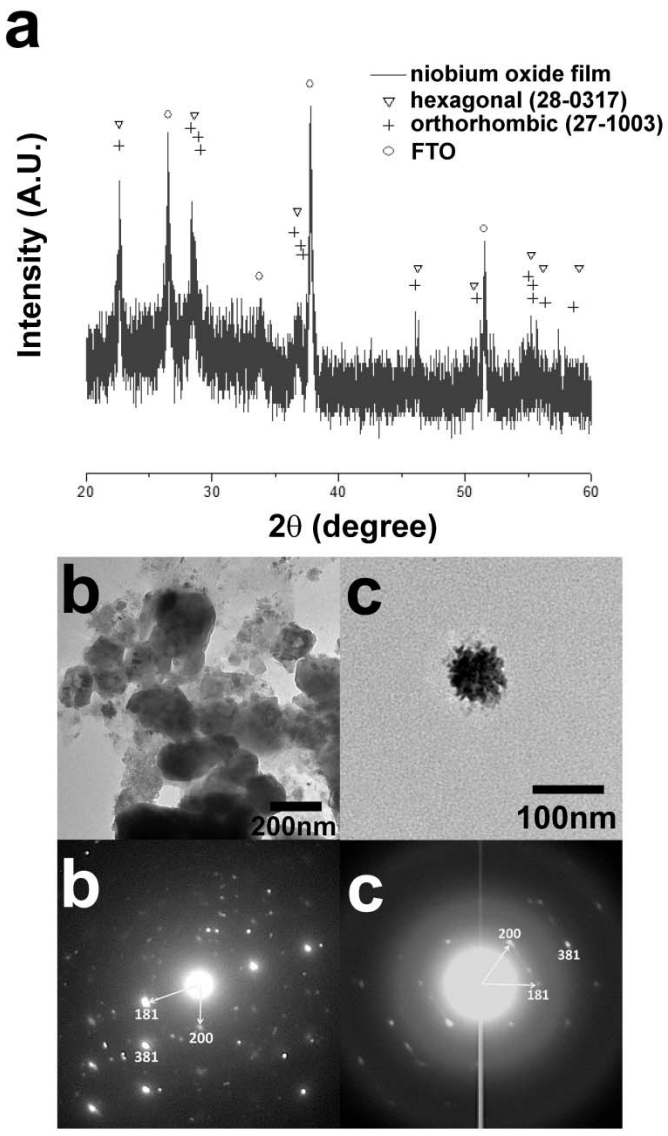

Figure 2.3 Crystallographic analysis of the prepared niobium oxide by using (a) XRD and (b), (c) TEM. SAED patterns in (b) and (c) revealed an orthorhombic crystal structure with a zone axis $[01\bar{8}]$.

2.3.3 Optical properties of the patterned niobium oxide films

The optical properties of the flat and patterned niobium oxide films were measured in the UV-visible range. Initially, apart from the mesoporous niobium oxide films shown in Figure 2.2, denser surface patterns were produced (by not adding polymeric additives to the oxide paste) to maximize the photonic crystal effect: when making photonic crystal structures, selection of two materials with high refractive index contrast yields the most effective effect.[32] In this surface patterning study, one material of the repeating unit is either air, (refractive index=1) in optical measurements, or the redox electrolytes in actual solar energy conversion experiments, e.g. acetonenitrile (n=1.34) in DSSCs; the other material is the niobium oxide (refractive index=2.39[42]). Once the intrinsic refractive index of two materials for patterning is determined, maximization of refractive index difference could be achieved by forming dense niobium oxide patterns: porous materials have refractive index between the neat materials and the air filling the pores.

SEM images of the dense surface patterns are shown in Figure 2.4 (a) and the transmission spectra in the UV-visible range of flat and patterned niobium oxide film with and without dyes are shown in Figure 2.4 (b). One can see a clear decrease in transmission by the surface patterned films, especially in the blue range, both with and without dye loading. The net change of transmission, reflection, and absorption by patterning are illustrated in Figure 2.4 (c) by normalizing the spectra from the patterned niobium oxide film to those from flat films. It can be seen from the plot that the effect of patterning on the optical property is distinct over a wide wavelength range. Moreover, PC effect is evident especially in the normalized transmission and absorption spectra, despite the large degree of variation with wavelength and the relatively small variation of normalized reflection spectra with

wavelength. Indeed, it was confirmed from Figure 2.4 (b) and (c) that the dense surface patterns on the surface constituted a PC structure strongly interacting with UV and visible light. However, the niobium oxide paste used to build dense patterns had critical problems in the surface patterning steps: as the paste did not contain polymeric additives, the additional layer dried too quickly when spread onto patterned PFPE mold and it could not be fused to the base layer. So, it was really hard to pattern a large area uniformly. Also, when spread onto the base layer and covered with a patterned mold to avoid the 'quick drying' problem, as the viscosity of the oxide paste without a polymeric additive is too small, it flows into the pores in the base layer and makes it less porous, rather than staying within the space between mold and base layer for patterning. Consequentially it was essential to stabilize the fabrication processes by using an oxide paste containing a polymeric additive while sacrificing some portion of the benefit of dense patterns; it would be meaningful to compare the optical properties of PCs made from porous patterns to those made from dense oxide patterns.

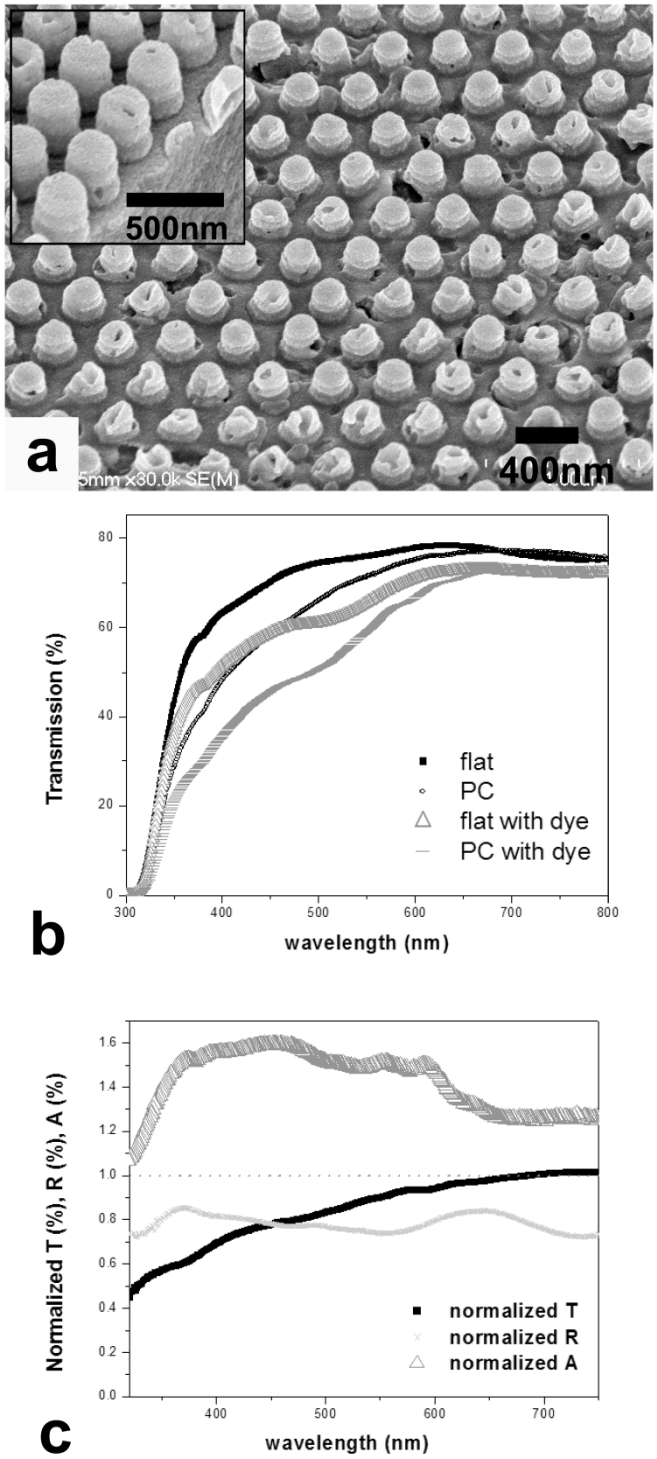

Figure 2.4 (a) SEM image of the dense patterns made of an oxide paste without polymeric additives. (b) Transmission spectra of flat and patterned niobium oxide films with and without dye loading. (c) Normalized transmission, reflection, and absorption spectra from a patterned film relative to a flat film as a function of wavelength.

Optical transmission spectra of mesoporous top layers (flat and/or patterned) identical to the films shown in Figure 2.2 are shown in Figure 2.5 (a). Although not so distinct as in the spectra of dense patterns, a drop in the transmitted intensity can be seen in the raw spectra. The normalized transmission in Figure 2.5 (b) indicates that the mesoporous patterns also formed a PC structure exhibiting decrement in transmission close to 20% around the 400nm wavelength range. Although the decrement of the normalized transmission by the mesoporous patterns was about a half of the value exhibited by dense patterns, considering the huge benefits of the polymer-containing oxide paste in the fabrication processes, the degradation of PC performance with mesoporous patterns is acceptable.

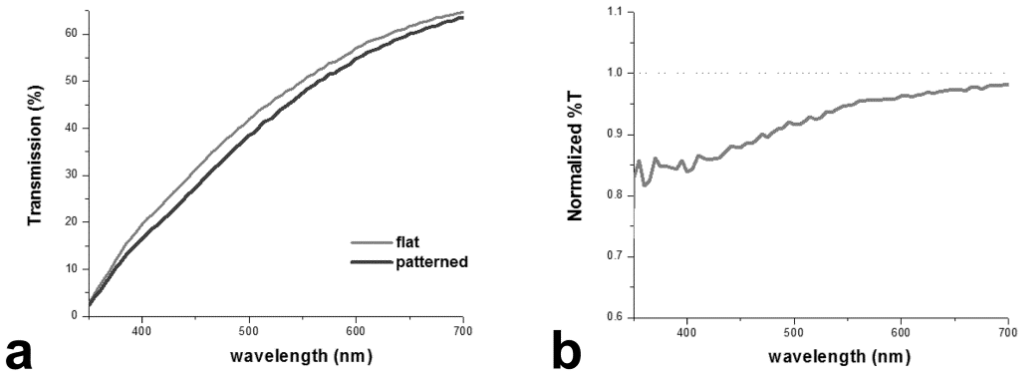

Figure 2.5 (a) Transmission spectra of flat and patterned films with mesoporous top layers. (b) Normalized transmission of the PC sample relative to the flat film.

2.3.4 Photoelectrochemical solar energy conversion by IPCE measurement

In order to observe how the optical effects by the superficial PC structure can actually affect the photocurrent generation, the flat and patterned niobium oxide electrodes were prepared in sealed DSSCs and the incident photon-to-current conversion efficiency (IPCE) was measured. Figure 2.6 (a) is the IPCE of flat and patterned samples versus wavelength. The patterned sample exhibited higher IPCE values than the flat sample over the whole wavelength range shown. To clarify the PC effect as a function of wavelength, the IPCE of the each sample was normalized at 530nm, as shown in the Figure 2.6 (b), and the normalized IPCE of the sample with PC to the IPCE of a flat reference sample, as drawn in the Figure 2.6 (c). It is notable from the Figure 2.6 (b) that the increment in IPCE exhibited by the PC structure becomes more distinct as the wavelength of the photons decreases, which is in good agreement with the trend observed in the optical measurements in Figure 2.5 (b). The enhancement of IPCE over the whole wavelength range is distinct especially in the Figure 2.6 (c): the normalized IPCE curve in the figure lies above one, meaning that all IPCE values of the PC structure were greater than the IPCE of the flat sample. Although the patterned sample was 3.6% thicker than the flat sample (2.971 μm and 2.864 μm, respectively), normalized IPCE revealed a much larger difference which could not to be explained by the thickness difference. This implies that the decrement of light transmission by the surface PC structure could be related to the increment of the absorption of photons as confirmed in Figure 2.4 (c), and that the increased absorption of photons caused a greater generation of photocurrent. So, it can be concluded that building PC structures by merely patterning the surface is a simple but powerful strategy for enhancing light harvesting and solar energy conversion. It can be seen from the plots in Figure 2.6 that the surface patterns

were especially more effective in the blue relative to the red end of the visible spectrum. As the patterns form a 2-D surface PC structure with an incomplete photonic band gap (PBG) rather than a 3-D structure forming a complete PBG in a narrow wavelength range,[32] it reflects photons over a wide energy span back to the mesoporous sensitized layer.[30,35] So, the blue enhancement can be explained by the combination of the two effects: on the one hand, it can be attributable to the geometry (especially the periodicity[35]) of the surface patterns used in this investigation, and one can expect different optical responses by tuning the period of the patterns. On the other hand, it is impacted by scattering in the blue wavelength region, i.e., by Rayleigh scattering[30,43] as photons of higher energy scatter more in the media. So, when unabsorbed photons are reflected back to the sensitized layer by the surface PC structure, reflected photons of shorter wavelength tend to have more chance for absorption. Thus, the enhancement of photon-to-current conversion by the surface patterns should increase by decreasing the wavelength of the photons, as shown in Figure 2.6 (a) through (c).

Indeed, the superficial surface patterns described here are quite an effective strategy to incorporate PC effects into DSSC devices using a much simpler fabrication process relative to 3-D photonic crystals structures. In addition, as the PC effects result from combinations of refractive indices of materials and geometry of the patterns,[32] if one apply the same patterns used in this study to other oxide semiconductor materials with similar refractive index, one can expect similar enhancement in solar energy conversion. Moreover, the hexagonal array of cylindrical posts investigated in this study was selected from extant patterns, not designed intentionally for optimal effects. This implies that more enhancements of IPCE than reported in this study are likely to be achieved by optimization of the geometry of the surface patterns.

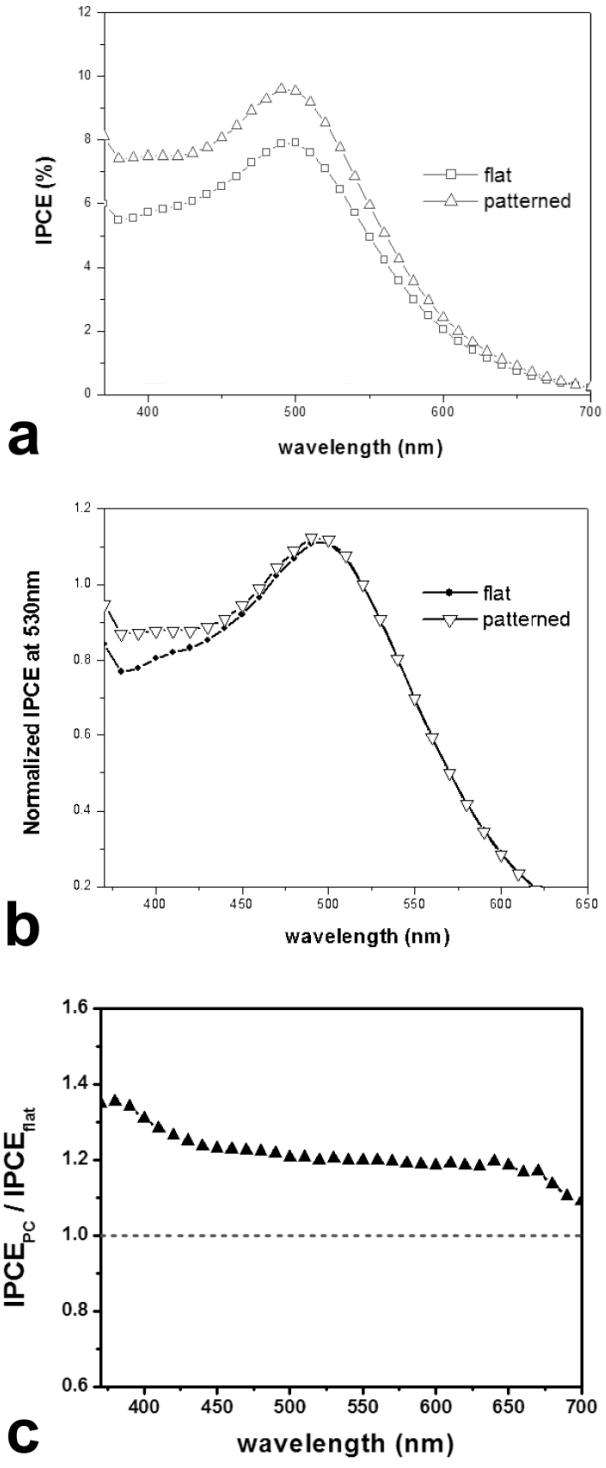

Figure 2.6 IPCE of flat and PC samples. (a) IPCE of flat and patterned (PC) niobium oxide anode; (b) the normalized IPCE of flat and PC samples at 530nm and (c) the normalized IPCE of PC relative to IPCE of flat film, revealing an enhancement of IPCE in the blue range.

2.4 Conclusions

A simple surface patterning technique using a photo-curable PFPE was applied to form photonic crystal structures on the mesoporous niobium oxide films. The surface patterns were well replicated using a PFPE mold on top of a preformed base layer with minimal changes in the dimensions of the oxide morphology. Even though surface structures exhibited changes in the detailed shape and dimensions relative to that of the mold, they retained the attributes of an ordered array retaining periodicity of the mold. Synthesized niobium oxide nanoparticles in the top and base layers had an orthorhombic structure (T-phase) irrespective of the number of calcination steps. Optical measurements showed that the surface patterns formed a PC structure resulting in increased absorption of photons, especially in the blue wavelength region. By this surface alteration of the optical behavior of niobium oxide films, more photocurrent was generated in solar energy conversion experiments using DSSCs. The IPCE was enhanced by the surface PC structure over the whole wavelength range of the UV-visible spectrum, but the enhancement was more distinct in the blue range, agreeing with the optical measurement. In summary, mesoporous surface patterns on niobium oxide electrodes can be readily formed into a photonic crystal structure that effectively enhances the photocurrent generation. This surface patterning strategy can also be applied to other mesoporous oxide semiconductor materials having similar refractive indices (e.g., titanium oxide and zinc oxide) routinely used in DSSCs.

2.5 References

(1) O'Regan, B.; Grätzel, M. *Nature* **1991**, *353*, 737-740.

(2) Nazeeruddin, M. K.; Kay, I.; Rodicio, A.; Humphry-Baker, R.; Müller, E.; Liska, P.; Vlachopouloss, N.; Grätzel, M. *J. Am. Chem. Soc.* **1993**, *115*, 6382-6390.

(3) Gao, F.; Wang, Y.; Shi, D.; Zhang, J.; Wang, M.; Jing, X.; Humphry-Baker, R.; Wang, P. M.; Zakeeruddin, S.; Grätzel, M. *J. Am. Chem. Soc.* **2008**, *130*, 10720-10728.

(4) Huang, S. Y.; Schlichthörl, G.; Nozik, A. J.; Grätzel, M.; Frank, A. J. *J. Phys. Chem. B* **1997**, *101*, 2576-2582.

(5) Kopidakis, N.; Neale, N. R.; Frank, A. J. *J. Phys. Chem. B* **2006**, *110*, 12485-12489.

(6) Yella, A.; Lee, H.-W.; Tsao, H. N.; Yi, C.; Chandrian, A. K.; Nazeeruddin, M. K.; Diau, E. W.-G.; Yeh, C.-Y.; Zakeeruddin, S. M.; Grätzel, M. *Science* **2011**, *334*, 629-634.

(7) Macak, J. M.; Tsuchiya, H.; Ghicov, A.; Schmuki, P. *Electrochem. Commun.* **2005**, *7*, 1133-1137.

(8) Roy, P.; Albu, S. P.; Schmuki, P. *Electrochem. Commun.* **2010**, *12*, 949-951.

(9) Sauvage, F.; Di Fonzo, F.; Li Bassi, A.; Casari, C. S.; Russo, V.; Divitini, G.; Ducati, C.; Bottani, C. E.; Comte, P.; Graetzel, M. *Nano Lett.* **2010**, *10* (7), 2562-2567.

(10) Tennakone, K.; Kumara, G. R. R.; Kottegoda, I. R. M.; Perera, V. S. P. *Chem. Commun.* **1999**, 15-16.

(11) Sayama, K.; Suguhara, H.; Arakawa, H. *Chem. Mater.* **1998**, *10*, 3825-3832.

(12) Jose, R.; Thavasi, V.; Ramakrishna, S. *J. Am. Ceram. Soc.* **2009**, *92* (2), 289-301.

(13) Feng, X.; Shankar, K.; Paulose, M.; Grimes, C. A. *Angew. Chem., Int. Ed.* **2009**, *48* (43), 8095-8098.

(14) Lenzmann, F.; Krueger, J.; Burnside, S.; Brooks, K.; Grätzel, M.; Gal, D.; Rühle, S.; Cahen, D. *J. Phys. Chem. B* **2001**, *105*, 6347-6352.

(15) Maruska, H. P.; Ghosh, A. K. *Solar Energy* **1978**, *20*, 443-458.

(16) Scaife, D. E. *Solar Energy* **1980**, *25*, 41-54.

(17) Grimes, C. A.; Varghese, O. K.; Ranjan, S. *Light, Water, Hydrogen: The Solar Generation of Hydrogen by Water Photoelectrolysis*; Springer: New York, 2007; p 191-255.

(18) Wurfel, U.; Peters, M.; Hinsch, A. *J. Phys. Chem. C* **2008**, *112*, 1711-1720.

(19) Ou, J. Z.; Rani, R. A.; Ham, M.-H.; Field, M. R.; Zhang, Y.; Zheng, H.; Reece, P.; Zhuiykov, S.; Sriram, S.; Bhaskaran, M.; Kaner, R. B.; Kalantar-zadeh, K. *ACS Nano* **2012**, *6*, 4045-4053.

(20) Barea, E.; Xu, X. Q.; Gonzalez-Pedro, V.; Ripolles-Sanchis, T.; Fabregat-Santiago, F.; Bisquert, J. *Energy Environ. Sci.* **2011**, *4*, 3414– 3419

(21) Kim, H.-N.; Moon, J. H. *ACS Appl. Mater. Interfaces* **2012**, *4*, 5821-5825.

(22) Luo, H.; Song, W.; Hoertz, P. G.; Hanson, K.; Ghosh, R.; Rangan, S.; Brennaman, M. K.; Concepcion, J. J.; Binstead, R. A.; Bartynski, R. A.; Lopez, R.; Meyer, T. J. *Chem. Mater.* **2013**, *25*, 122-131.

(23) Usami, A. *Chem. Phys. Lett.* **1997**, *277*, 105-108.

(24) Nishimura, S.; Abrams, N.; Lewis, B. A.; Halaoui, L. I.; Mallouk, T. E.; Benkstein, K. D.; Lagemaat, J. V. D.; Frank, A. J. *J. Am. Chem. Soc.* **2003**, *125*, 6306-6310.

(25) Halaoui, L. I.; Abrams, N. M.; Mallouk, T. E. *J. Phys. Chem. B* **2005**, *109*, 6334-6342.

(26) Mihi, A.; Míguez, H. *J. Phys. Chem. B* **2005**, *109*, 15968-15976.

(27) Mihi, A.; López-Alcaraz, F. J.; Míguez, H. *Appl. Phys. Lett.* **2006**, *88*, 193110-193113.

(28) Herman, L.A.; Yip, C.H.; Wong, C.C. *J. Nanosci. Nanotechnol.* **2010**, *10*, 4657-4662.

(29) Guldin, S.; Hüttner, S.; Kolle, M.; Welland, M. E.; Müller-Buschbaum, P.; Friend, R. H.; Steiner, U.; Tétreault, N. *Nano Lett.* **2010**, *10*, 2303-2309.

(30) Lee, S.-H. A.; Abrams, N. M.; Hoertz, P. G.; Barber, G. D.; Halaoui, L. I.; Mallouk, T. E. *J. Phys. Chem. B* **2008**, *112*, 14415-14421.

(31) Colodrero, S.; Mihi, A.; Häggman, L.; Ocaña, M.; Boschloo, G.; Hagfeldt, A.; Míguez, H. *Adv. Mater.* **2009**, *21*, 764-770.

(32) Johnson, S. G.; Joannopoulos, J. D. *Acta Mater.* **2003**, *51*, 5823-5835.

(33) Zhao, X.-M.; Xia, Y.; Whitesides, G. M. *J. Mater. Chem.* **1997**, *7*, 1069-1074.

(34) Ko, D.-H.; Tumbleston, J.; Zhang, L.; Williams, S. S.; DeSimone, J. M.; Lopez, R.; Samulski, E. T. *Nano Lett.* **2009**, *9*, 2742-2746.

(35) Kim, J.; Koh, J. K.; Kim, B.; Kim, J. H.; Kim. E. *Angew. Chem. Int. Ed.* **2012**, *51*, 6864-6869.

(36) Rolland, J. P.; Van Dam, R. M.; Schorzman, D. A.; Quake, S. R.; DeSimone, J. M. *J. Am. Chem. Soc.* **2004**, *126*, 2322-2323.

(37) Rolland, J. P.; Hagberg, E. C.; Denison, G. M.; Carter, K. R.; DeSimone, J. M. *Angew. Chem. Int. Ed.* **2004**, *43*, 5796-5799.

(38) Maynor, B. W.; LaRue, I.; Hu, Z.; Rolland, J. P.; Pandya, A.; Fu, Q.; Liu, J.; Spontak, R. J.; Sheiko, S. S.; Samulski, R. J.; Samulski, E. T.; DeSimone, J. M. *Small* **2007**, *3*, 845-849.

(39) Hampton, M. J.; Williams, S. S.; Zhou, Z.; Nunes, J.; Ko, D.-H.; Templeton, J. L.; Samulski, E. T.; DeSimone, J. M. *Adv. Mater.* **2008**, *20*, 2667-2673.

(40) Wang, Z.-S.; Kawauchi, H.; Kashima, T.; Arakawa, H. *Coord. Chem. Rev.* **2004**, *248*, 1381-1389.

(41) Lenzmann, F.; Shklover, V.; Brooks, K.; Grätzel, M. *J. Sol-Gel Sci. Tech.* **2000**, *19*, 175-180.

(42) Kukli, K.; Ritala, M.; Leskelä, M.; Lappalainen, R. *Chem. Vap. Deposition* **1998**, *4*, 29-34.

(43) Bohren, C. F.; Huffman, D. R. *Absorption and scattering of light by small particles*; John Wiley & Sons, Inc.: Weinheim, Germany, 1983.

CHAPTER 3

SURFACE PATTERNING ON MESOPOROUS TITANIA FOR DYE-SENSITIZED SOLAR CELLS

3.1 Introduction

Since the seminal discovery of the high efficiency dye sensitized solar cell (DSSC) by O'Regan and Grätzel,[1] a wide range of strategies have been applied to increase its efficiency, primarily by the development of new dyes absorbing a wider spectrum of light,[2-6] new oxide semiconductor supports in addition to titania,[7-15] and the design and optimization of the cell structure, e.g. tubular TiO_2.[16-19] An alternative approach to enhanced efficiency is to interface optical structures with DSSCs for improving photon absorption and photocurrent generation in the conventional mesoporous titania layer.[20-27] Usami proposed a new structure having an additional layer of larger titania particles with optimal diameter about $1.3\sim1.4\times\pi/k$ (where k is the wave number) for effective scattering and total internal reflection in order to confine light in the dye-sensitized mesoporous titania layer.[20] Then, photonic crystals (PCs) were used to increase the path length of light: bilayer structures of a conventional base titania film (for loading a large number of dye molecules and mainly generates photocurrent) and additional photonic crystal layers having an inverse opal structure (for forming a photonic stop band and reflecting unabsorbed photons back to the mesoporous titania layer).[21-27] The reason inverse opal/base bilayer structures have been intensively studied is that one can

easily form a 3-D photonic stop band systematically by selecting the diameter of the monodisperse polystyrene (PS) beads.[26] This implies that one can easily design a photonic stop band wavelength by simply selecting the diameter of the PS, mainly focusing on the red region where intrinsic absorption by the dye molecules is weak.[27] Mihi et al. proposed different sequence of bilayer structures and modeling for them, and reported an enhancement in IPCE by the inverse opal photonic crystal layer.[23,24] Nishimura et al.[21] and Halaoui et al.[22] also reported enhanced IPCE by the inverse opal PC layer. However, due to the complex, multistep processes required to form an inverse opal photonic crystal layer in the DSSCs, it has been challenging to clarify the photonic crystal effects on the actual operation of DSSCs.[27] And, to the best of our knowledge, only the recent work by Lee et al.[26] confirmed the enhancement of efficiency—up to 24% in the photoelectrochemical operation of DSSCs—with multiple numbers of samples. So, it is necessary to develop a new PC structure which can be fused into the DSSCs via simpler processes. For example, although PC structures of lower dimensions are not as effective as the 3-D PCs which form a complete photonic band gap (PBG),[28] 2-D surface patterning by soft-lithography[29-31] is worth pursuing as an alternative approach because of its easy and simple fabrication methods.[15,32,33]

Herein, I describe a simple surface patterning process based on the soft-lithographic techniques[29-31] to form photonic crystal structures on a DSSC electrode surface. Perfluoropolyether (PFPE)[30] was used to replicate patterns etched into Si master and reproduce them on the mesoporous titania electrodes. We utilize PFPE's low surface energy and high gas permeability.[34] The optical characteristics and the performance of the surface patterned DSSCs were analyzed and compared to the flat DSSCs.

3.2 Experimental Section

3.2.1 Materials

A titania gel containing nanocrystalline anatase titania particles and a polymeric plasticizer (DSL 18NR-T) was purchased from Dyesol. The gel was diluted—mixed with ethanol (200proof, Decon Labs, Inc.), 800mg of gel with 1ml of ethanol—for spin-casting. A PFPE precursor solution consisting of 1000g/mol PFPE (an α, Ω–functionalized dimethacrylate and 2, 2-diethoxyacetophenone as the photoinitiator) was donated by Liquidia Technologies Inc. FTO coated glass substrates (15Ω/sq, 2.3mm thick) were purchased from Hartford glass. FTO coated glass substrates were sonicated in acetone (99.5%, Fisher Scientific), isopropanol (99.9%, Fisher Scientific), and deionized water sequencially and then heat-treated at 500°C in the air for 10min before coating the titania gel. *Cis*-bis(isothiocyanato)bis(2,2′-bipyridyl-4,4′-dicarboxylato) ruthenium(II) bis(tetrabutyl ammonium) ($RuL_2(NCS)_2$-2TBA, commonly known as Ruthenium535 bis-TBA or N719 dye) was purchased from Solaronix. For preparation of the redox electrolyte, LiI (99.9%, Aldrich), I_2 (≥99.99%, Aldrich), 1,2-dimethyl-3-propylimidazolium iodide (≥98%, Tokyo Chemical Industry), tert-butylpyridine (96%, Aldrich), guanidiniumthiocyanate (99%, Aldrich), and acetonitrile (99.9%, Fisher Scientific) were used. A 100μm Surlyn film was purchased from Solaronix to fabricate sealed DSSC's.

3.2.2 Preparation of patterned PFPE molds

PFPE molds were prepared by following the method reported by Hampton et al.:[35] A photocurable PFPE solution was poured onto a patterned Si-wafer and spread evenly. After purging with nitrogen gas for 3min, polymerization was achieved by UV radiation for 3min. The photocured PFPE mold was carefully removed from the mold and washed with ethanol

to remove uncrosslinked residues on the patterned surface. Flat PFPE films were also prepared similarly by using a non-patterned, flat Si wafer for fabricating non-patterned mesoporous titania electrodes as a control.

3.2.3 Preparation of patterned electrodes

FTO coated glass substrates (15Ω/sq, 2.3mm thick, Hartford glass) were sonicated in acetone, isopropanol, and deionized water for 20min each, followed by heat treatment at 500°C for 10min to completely remove organic residues. Figure 3.1 shows the procedure for forming mesoporous patterned titania electrodes for the DSSC. Surface patterned titania films were prepared in a 2-step process: 1) formation of a thick base layer (Figure 3.1-(b); the final thickness around ~12μm after calcination), and 2) formation of an additional thin layer (Figure 3.1-(c), patterned or flat, less than 1μm thick after calcination).

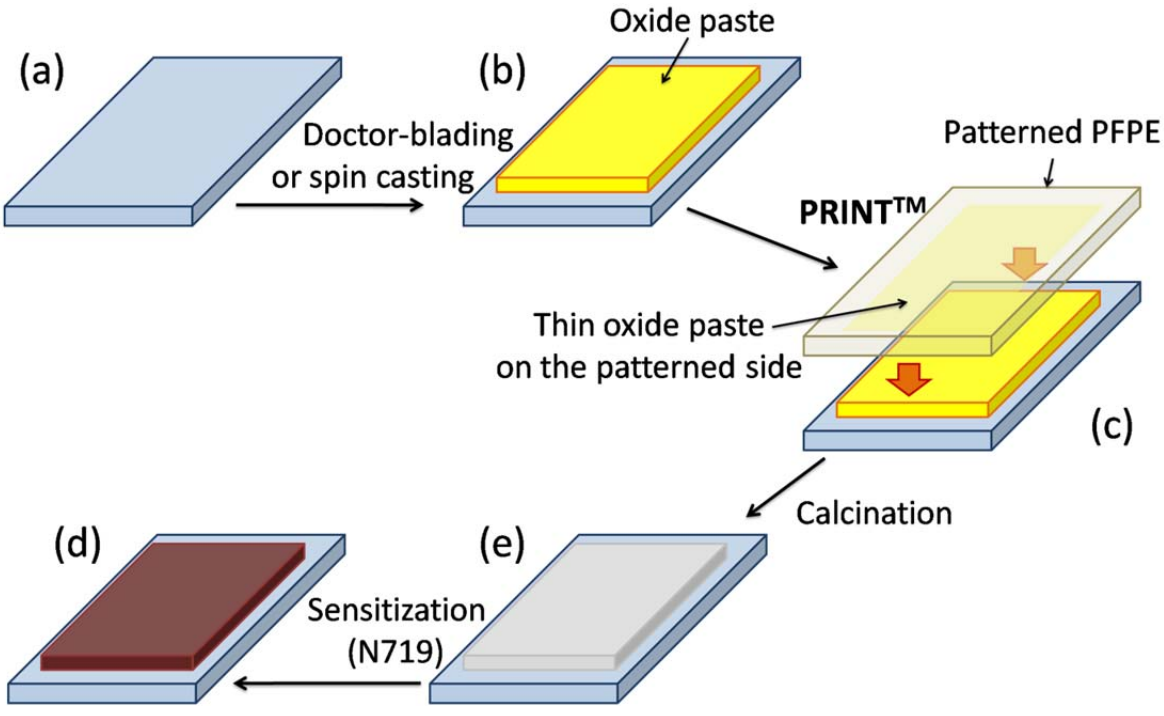

Figure 3.1 Procedures for forming mesoporous patterned titania electrodes for the DSSC.

To form thick base layers, titania precursor films were formed on prepared FTO coated glass substrates by spin-casting the titania containing gel for precise control over the final oxide layer thickness. The titania gel was mixed with ethanol (800mg of gel with 1ml of ethanol) to obtain a solution suitable for spin-casting. The diluted oxide solution was spin-cast onto prepared FTO-coated glass substrates (2000rpm, 30 sec); this was repeated 3 times to achieve the desired thickness (around 10μm). On top of a thick base layer, an additional thin patterned layer was formed by the soft-lithographic technique called PRINT^{TM} (pattern replication in non-wetting templates),[30,31,32] as shown in Figure 3.1-(c). A very small amount of titania gel was spread evenly onto either flat (for the control group) or patterned PFPE molds that were placed onto the thick base layer. Mild pressure was applied to the base-layer/additional-layer/PFPE-mold assembly to ensure good mechanical contact between the PFPE mold and oxide gel under layer throughout the drying step (80°C in an oven). After complete drying, the thick base layer and the additional thin (patterned or flat) layer merged into a single united entity without an interior interface. The latter interface layer inherently appears in the conventional inverse opal-based DSSCs.[21,23,26,27] The dried multi-layered films were calcined in a furnace at 500°C into mesoporous titania (Figure 3.1-(d)). The surface patterns used were gratings with variable spacings consisting of rectangular lines (250nm(W)×150nm(H) separated by 250, 500, and 750nm on the Si master), or a 2-dimensional array of cylindrical posts (200nm(D)×200nm(H)) separated by 200nm in a hexagonal surface pattern.

3.2.4 Analytical instrumentation

Both surface patterns and mesoporous morphologies of the calcined titania films were analyzed with a scanning electron microscope (S-4700, Hitachi). Quantitative information

about the surface patterns were collected with an atomic force microscopy (AFM, Veeco Metrology Group). UV-visible absorption spectra were obtained with an integration sphere (Cary 5000 fitted with DRA 2500). A surface profilometer (KLA Tencor P-6, scan speed: 50μm/s, scan length: 5mm) was used to measure the thickness of prepared titania films.

3.2.5 Sensitization of electrodes

N719 dye was used for sensitization of the mesoporous titania. The N719 dye was added to a 1:1 mixture of acetonitrile and t-butanol (0.2mM), and the solution was sonicated for 30 min. The solution was then centrifuged to remove aggregates. Before sensitization, prepared titania films were heat treated at 500°C for 30min and cooled down to 80°C, then slowly submerged into the dye solution to avoid a thermal shock and possible damage to the nanoparticle network. The samples were sensitized overnight in the solution. After sensitization, samples were rinsed with acetonenitrile to wash off unabsorbed dye and the sensitized titania films were trimmed to ~4 mm×4 mm with a razor blade.

3.2.6 DSSC preparation and photochemical measurements

In order to measure the performance of the DSSC's, we prepared sealed DSSC's basically following methods reported by Wang et al.,[36] using a 100μm Surlyn spacer and drilling one hole for electrolyte injection. The redox electrolyte was a solution of 0.1 M LiI, 0.05 M I_2, 0.5 M 1,2-dimethyl-3-propylimidazolium iodide, 0.5 M t-butylpyridine, and 0.1 M guanidiniumthiocyanate in dry acetonitrile. A Keithley 6517A current meter coupled with a 75W Xe Oriel 6251/Oriel Cornerstone 260 monochromator was used to measure the incident photon-to-current conversion efficiency (IPCE). The photocurrent density-photovoltage (***J*-*V***) curves of the cells were measured using an AM 1.5 solar simulator (NEWPORT 1000-W Xe lamp and an AM 1.5 filter) and a Keithley 2400 source meter.

3.3 Results and Discussion

3.3.1 Analysis of the surface morphology and patterns

The surface images of the calcined samples are shown in Figure 3.2. The calcined films exhibited a mesoporous structure with titania particle sizes around 20nm, adequate to load the (patterned) substrate with a sufficient amount of N719 dye. The well-formed surface patterns on the titania films had lateral dimension almost equal to the original dimensions of the Si master and the PFPE molds. This implied that it is highly probable that the heights of the patterns might be lower than the original mold depth dimension as a result of shrinkage during the drying and calcinations steps. The AFM heights of patterns have nominal values of ~175nm for cylinders in the hexagonal array, and ~135nm for line patterns, less than the master dimension (200nm for cylinders in the hexagonal array and 150nm for line patterns). During the drying following the PRINT step, the superficial thin titania gel layer was confined between the patterned PFPE mold and the previously dried, thick base layer; it fuses into a single entity by the diffusion of the fluid thin paste layer across the base layer interface. That process was enabled by the mild applied pressure to ensure the contact between the mold containing the titania gel and the base layer. When this interfacial junction dried, lateral shrinkage was prohibited by the solid base layer, and thus most of the shrinkage must be accommodated in the direction normal to the interface surface. As the PFPE has high gas permeability,[34] the normal direction is the most likely direction for the evaporation of the solvent phase from the titania gel in contact with the mold.

It was noted that the height shrinkage of the 2-D arrays of cylinders and 1-D lines was similar, 12.5% and 10%, respectively, consonant with lateral confinement effects on the surface plane of the base layer. A more important feature of the surface patterned

mesoporous TiO_2 layer in Figure 3.2 (e) was the cross-section of the sample: There was no hint of the interface between the initial underlying thick base layer and the additional thin layer produced in the PRINT step. These seamless structures could be obtained because the base layer and thin layer used for PRINT were made from identical gels. In contrast, related inverse opal/mesoporous base bilayer structures are inherently susceptible to defect formation at the interface region during the fabrication process, and these defects can cause serious problems both mechanically and electrically.[27] In summary, the PRINT methodology, a kind of soft-lithographic technique employed herein for surface patterning of titania electrodes, can readily form photonic crystal structures in a much simpler way without serious structural or interface issues.

3.3.2 Optical characterization of the sensitized TiO_2 films

To evaluate the optical properties of the patterned TiO_2 films, UV-vis absorption was measured in the integration sphere (IS). Figure 3.3 compares two types of integration spheres: one placing the sample at the entrance window of the sphere (Figure 3.3 (a)), and the other at the center (Figure 3.3 (b)). As the sensitized TiO_2 films scatter light, and the commercially available FTO coated glass substrate and a metallic mask have finite thicknesses on the order of a millimeter, some portion of light cannot enter the IS shown in Figure 3.3 (a), even though the sample actually transmits or reflects that portion. The undetected portion of light results in an underestimation of transmission (**T(λ)**) or reflection (**R(λ)**). As this type of IS calculates absorption (**A(λ)**) by subtracting **T(λ)** and **R(λ)** from the incident intensity, **A(λ)** can be overestimated if measured by this type of IS. Moreover, as the sample is placed at the center of the IS in Figure 3.3 (b), all of the incident light except that absorbed can be detected. So, **A(λ)** can be calculated more accurately by subtracting the measured portion of the light

from the incident light. This is more important to the surface PC structures with line gratings which scatter and change the direction of photons,[37] having a potentially higher risk of overestimation of absorption.

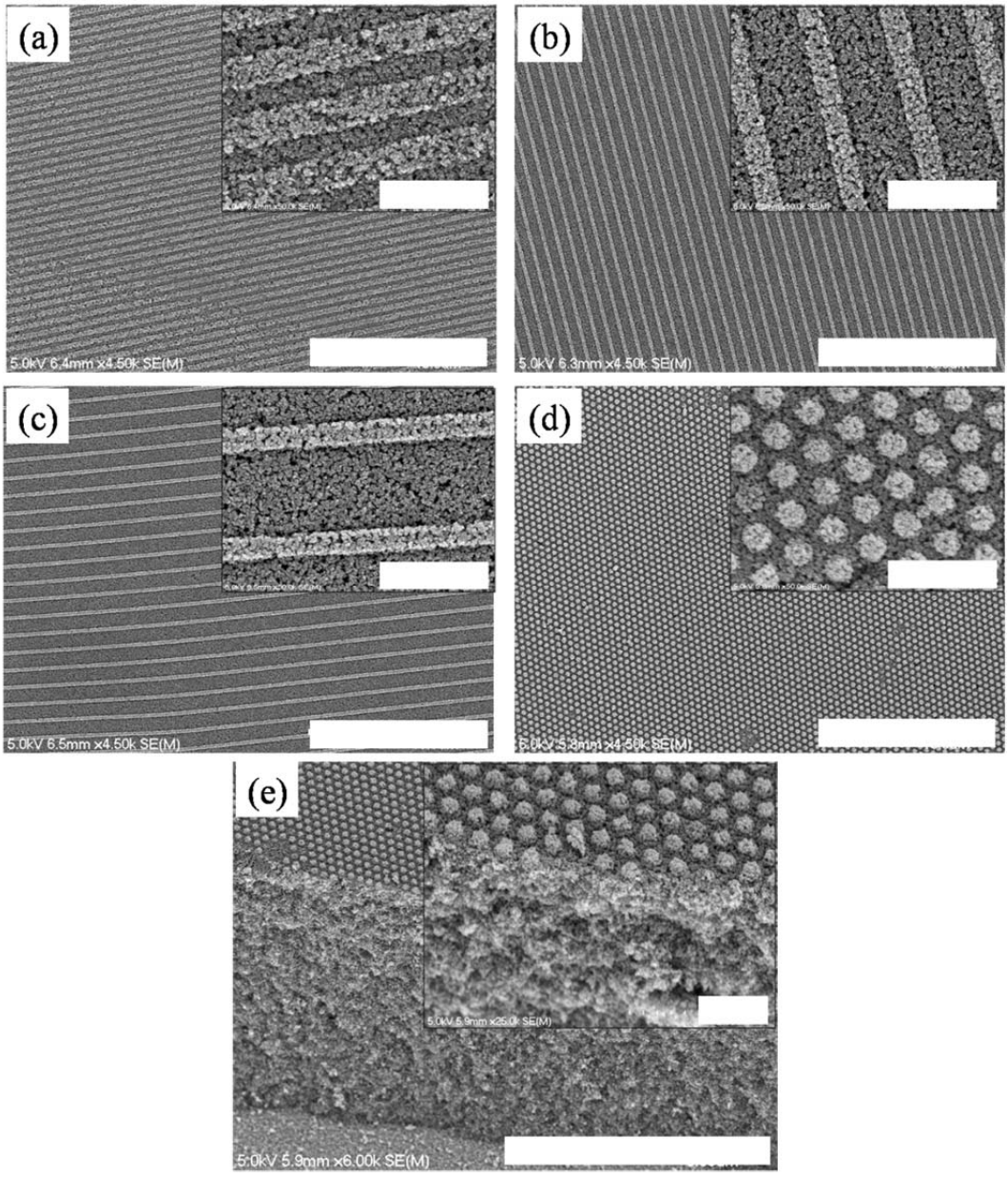

Figure 3.2 SEM images of the patterned surfaces: rectangular line patterns with different spacing ((a) 250nm, (b) 500nm, (c) 750nm) and cylindrical post in hexagonal array (d) and (e). The crosssection view in (e) reveals that the base layer and PRINT layer formed a monolayer without an interface. Scales were 10μm in large images and 1μm in small images. (Scales are 1μm in the insets and 10μm in the larger figures.)

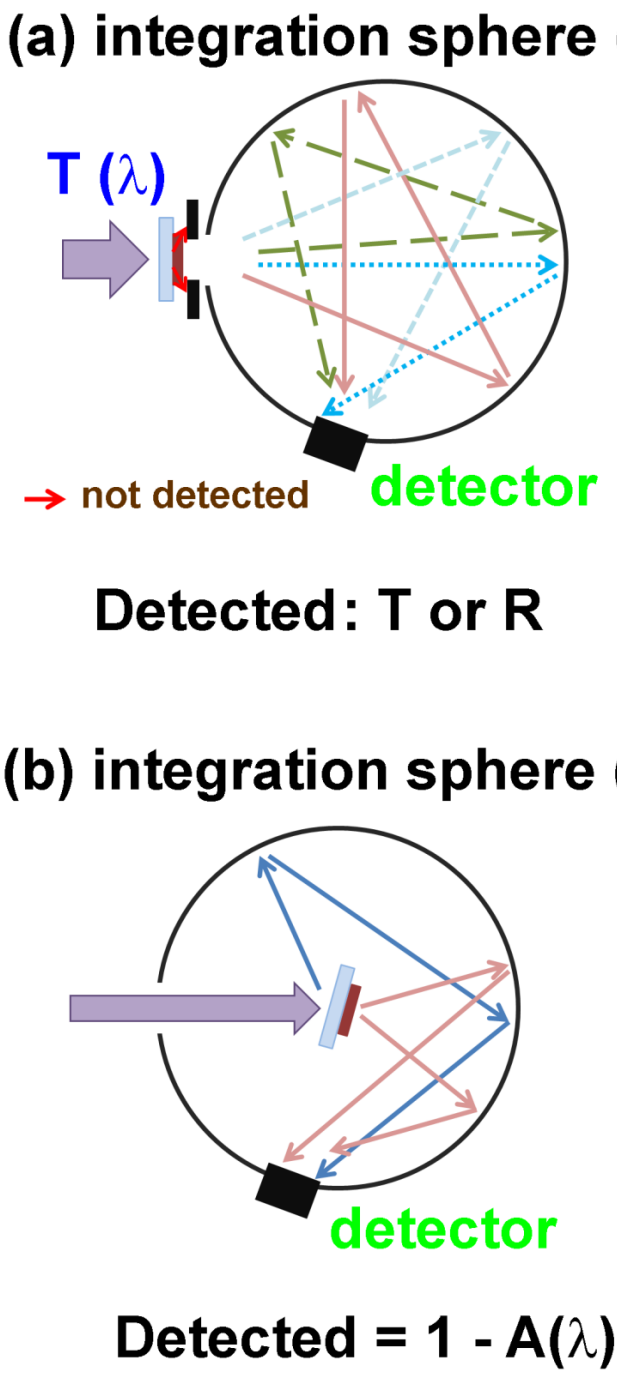

Figure 3.3 Comparison of two types of integration spheres for evaluating absorption of sensitized TiO_2 samples. (a) The samples is placed at the entrance window of the IS and some portion of light can be neglected, leading to overestimation of absorption. (b) As the sample lies inside the IS, all of the light except that which is absorbed is measured by the detector.

Figure 3.4 shows measured and smoothed absorption spectra of flat and patterned samples respectively, after sensitization. The measurement was performed in the wavelength range from 350nm to 750nm, covering the UV to the near IR, but due to large scattering at shorter wavelengths (below 450nm), only the portion with wavelengths longer than 450nm is shown. Samples were located inside of an integration sphere to avoid potential intensity loss by reflection or diffraction. Hence, the light intensity recorded by the detector is the portion of the incident light minus the absorbed portion. One cannot see any distinct absorption enhancement by patterning. In fact, there appears to be some decrement over some or all of the wavelength range (Figure 3.4 (a)). This may be attributed to thickness variations both in an individual sample (typically ~1μm~) and between samples (average thickness of individual samples varied typically 12.5~13.51μm), because the spot size of the incident beam is much smaller than the titania film area, i.e., the measured spectra were collected only from a small area exposed to the incident beam.

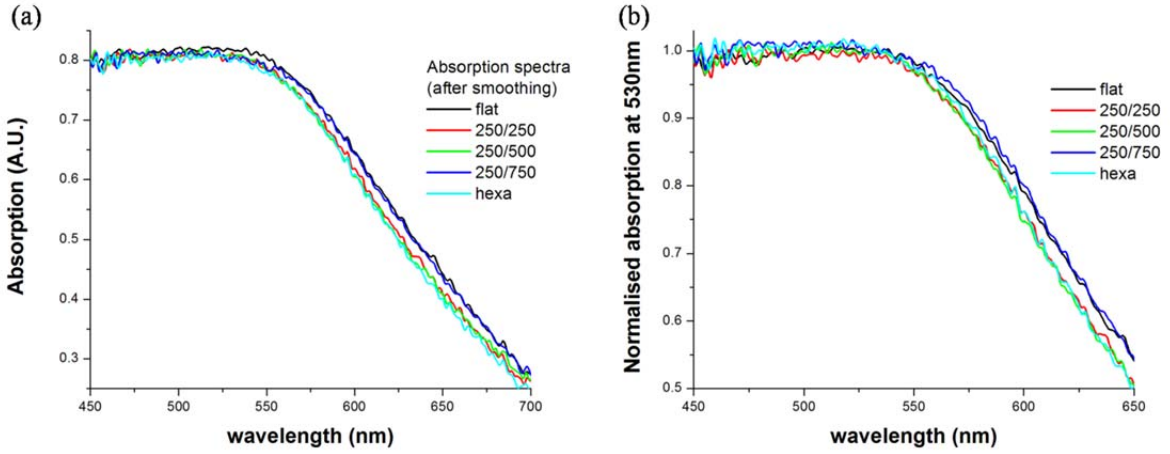

Figure 3.4 Absorption spectra of samples measured in the integration sphere. The spectra shown in (a) were smoothed to remove noises for easier comparison. Spectra shown in (b) were obtained by normalizing spectra in (a) at 530nm.

The trend is almost the same in the normalized spectra at 535nm, as shown in Figure 3.4 (b). Though the difference between spectra is not so clear, one can see a very slight enhancement in the normalized absorption spectrum of the 250/750 sample over the whole wavelength range shown. Similar relative enhancements at shorter wavelengths are apparent in the absorption spectra of 250/250, 250/500, and HEXA samples, relative to that of the flat control sample. Note that the samples have 1- or 2-D photonic crystal structures only on the surface rather than a 3-D structure in the bulk substrate like the inverse opal architectures. This means that the main function of the superficial patterning is diffraction of light to various angles and modes depending on the photonic crystal geometry,[15,37] rather than forming a photonic stop band at a specific designed wavelength. Thus, there cannot be sharp absorption enhancements at a specific wavelength in the patterned substrates. Another noteworthy aspect of the experimental conditions is that because of experimental limitations the absorption spectra in Figure 3.4 were collected in the air (refractive index, n=1), and not in the redox electrolyte of the DSSC. As the main component of the redox electrolyte is the acetonitrile, the refractive index difference between sensitized TiO_2 and acetonitrile (refractive index, n=1.34[26]) is smaller than that in air. Consequently, the actual optical attributes of the patterned titania films should be inferred from experiment or calculations that consider the optical consequences of the acetonitrile medium found in a DSSC.

To evaluate the absorption of flat, reference TiO_2 and patterned samples close to the real operation condition of DSSCs, sensitized TiO_2 films embedded in the redox electrolyte, and sealed between two FTO coated glasses, were prepared. The only difference between these samples and the real DSSCs is the absence of the Pt layer on the cathode to allow transmission of light. Figure 3.5 shows the absorption spectra of sensitized TiO_2 films

embedded in the actual electrolyte to simulate the DSSCs. There is no special difference between groups, which agrees with the spectra in Figure 3.4. So, there is no evidence for a significant enhancement of the light harvesting efficiency (LHE),[1] contrary to my previous work with 3μm Nb_2O_5 film.[15] The discrepancy seems to result from different thickness levels and porosities of the two systems so that the intrinsic absorptions are too different to be equally affected by the surface PC structures: as the intrinsic absorption of the sensitized TiO_2 is high enough, no significant enhancement can be made by reflection at the surface patterns; additionally, the thin (around 3μm) Nb_2O_5 films don't absorb much and have more room for enhancement by surface PC patterns.

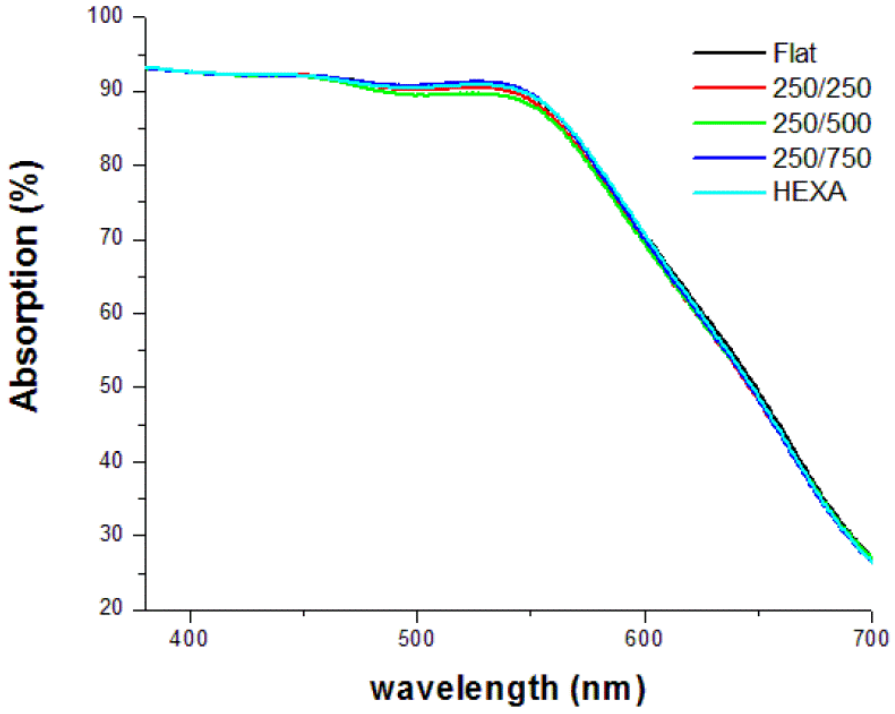

Figure 3.5 Absorption spectra of sensitized TiO2 with or without surface PC structure embedded in the electrolyte: T and R were measured by the IS shown in Figure 3.3 (a) and absorption was calculated by the relationship A=1-T-R.

On the other hand, it can be seen from Figure 3.6 that there appear significant changes between the transmission spectra of samples. One most probable reason for this is the surface PC structures which scatter photons back to the sensitized TiO_2 layer and cause an apparent decrement in transmission spectra depending on wavelength. However, as the spectra were measured before sensitization, the differences would become smaller after dye loading, but Figure 3.6 gives a hint about the characteristics of the surface PC structure as a function of wavelength. At this point, enhancement in LHE does not seem evident enough to cause significant changes in solar energy conversion performances. So, in the next section, I will show experimental data of solar energy conversion and discuss the results focusing on the PC effect.

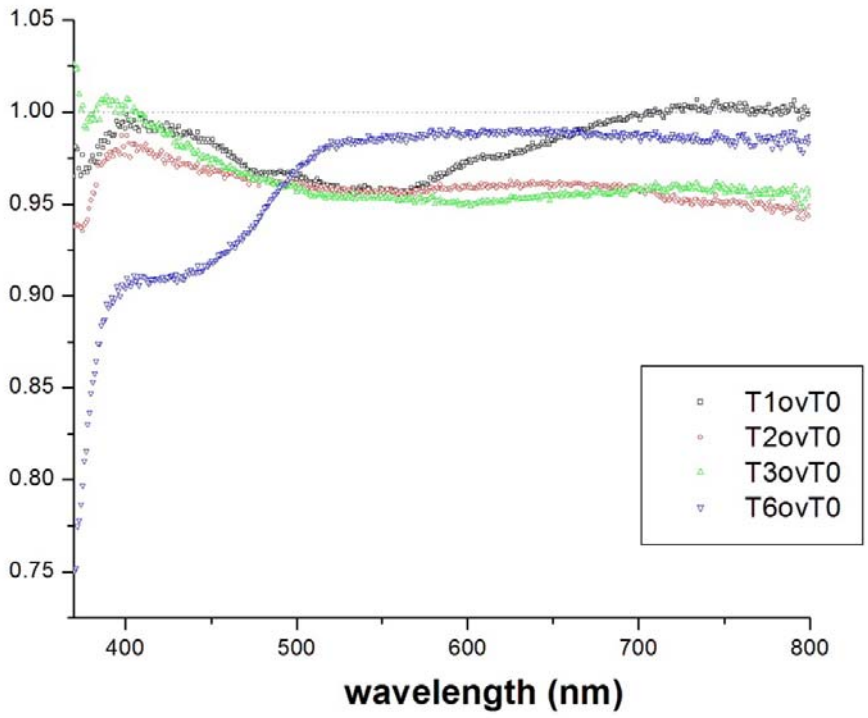

Figure 3.6 Normalized transmission spectra of flat (denoted as '0') and patterned (1~6) TiO2 films before dye loading.

3.3.3 Characterization of photoelectrochemical solar energy conversion

The incident photon-to-current conversion efficiency (IPCE) of samples was measured to analyze the effects of the superficial PC structure on the characteristics of DSSCs. In Figure 3.7 (a), the IPCE of selected samples are shown. All of the patterned samples revealed higher IPCE values than the flat sample over the whole wavelength range shown, although significant enhancement in absorption spectra was not confirmed in the previous section. This suggests that incorporating photonic crystal structures in the form of surface patterning in DSSC is an effective way for solar energy conversion with all the LHE variation in error range. As IPCE is given as a function of LHE, CIE, and CCE as shown in Equation 1.1,[1] the results in Figure 3.7 (a) imply that there might be changes in CIE or CCE by the surface PC structure. To clearly show the PC effect as a function of wavelength, IPCE's normalized to the IPCE of a flat sample, were depicted in Figure 3.7 (b). All of the spectra were higher than 1, meaning there is enhancement over the whole wavelength range. The surface patterns were especially good at producing higher enhancement in the short wavelength range relative to the red end of the visible except for the hexagonal patterned arrays. The pattern most effective at the absorption peak of N719 dye was the 250/750 line pattern; the 250/250 line pattern revealed a peak around 470nm, and the 250/500 line pattern exhibited a plateau around 560nm. Irrespective of peak positions, the IPCEs of the line patterned samples revealed an increasing degree of enhancement on decreasing the wavelength. In general, photons with higher energy scatter more in the media by Rayleigh scattering.[26,38] So, when unabsorbed photons are reflected back through the mesoporous titania electrode by the surface photonic crystal structure, photons of shorter wavelength tend to be absorbed more. Thus, the overall trend of photon-to-current conversion should increase

by decreasing the wavelength of the photons, as shown in the figure. However, the sample with the hexagonal pattern revealed different characteristics in its normalized IPCE: A higher enhancement was found at ~460nm and longer the wavelength region >640nm, and a minimum at 540nm. Considering the absorption peak of N719 dye, this implies that the hexagonal array of posts on the surface effectively enhanced the IPCE at wavelength ranges shorter or longer than the absorption peak of the dye.

Nevertheless, due to the high degree of fluctuation of the absorption spectra measured in the IS, Figure 3.4 (a) only cover wavelengths longer than 450nm and did not show if there exists enhancement in LHE below 450nm range. So, there is no clear evidence to relate the increased IPCE in that interval to the LHE at the shorter wavelength at this moment. However, it can be seen in Figure 3.6 (b) and Figure 3.7 that there are coincident in the wavelength range between decreased transmission in Figure 3.6 (b) and enhancement in the IPCE in Figure 3.7, though the question if the decrement in transmission by the TiO_2 films not sensitized can be enough to generate larger change in the IPCE shown in Figure 3.7 is still left open.

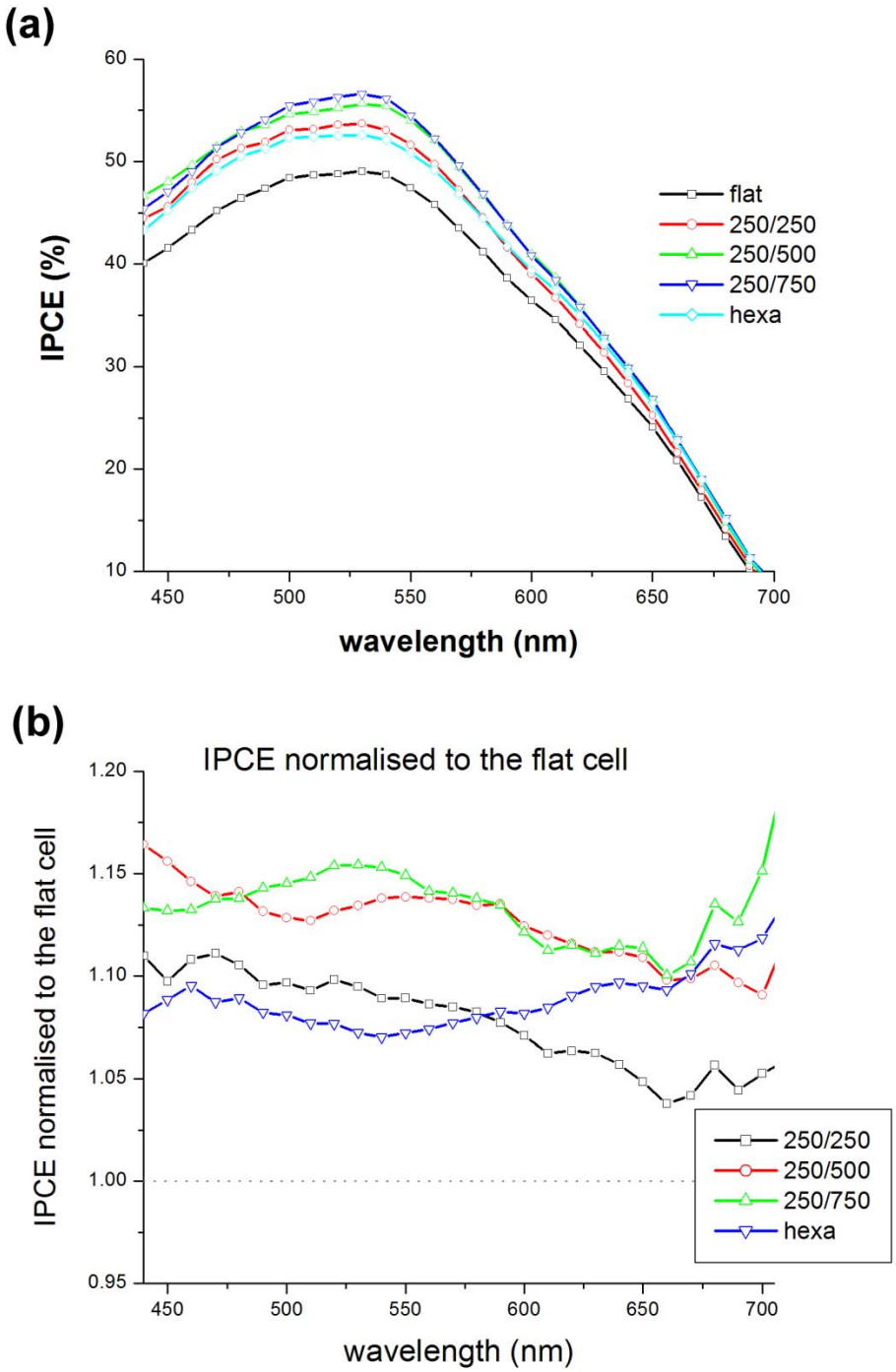

Figure 3.7 (a) Incident photon-to-current conversion efficiency (IPCE) of selected samples and (b) after normalization to the IPCE of flat sample. The IPCE curves of patterned samples all exhibit enhancement at the whole wavelength range.

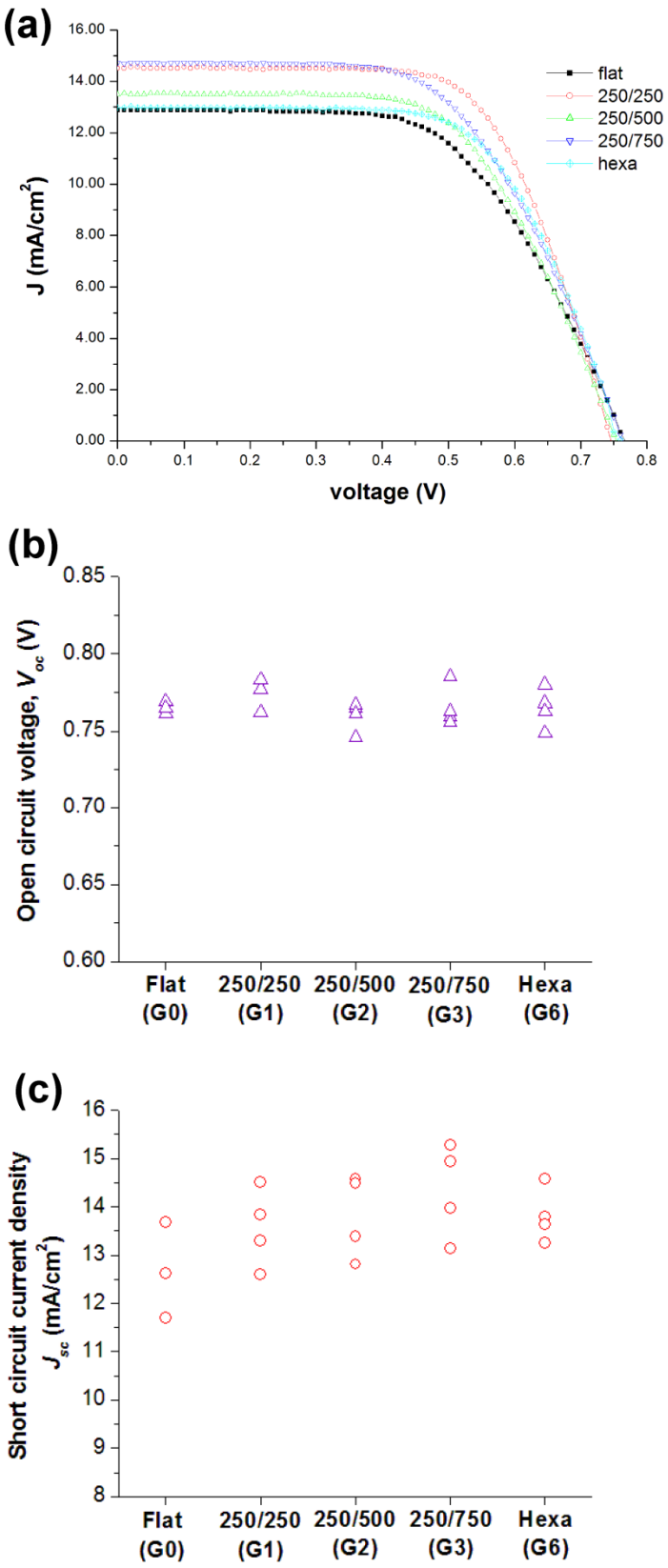
(a)
J (mA/cm^2)
voltage (V)
flat
250/250
250/500
250/750
hexa
(b)
Open circuit voltage, V_{oc} (V)
Flat (G0)
250/250 (G1)
250/500 (G2)
250/750 (G3)
Hexa (G6)
(c)
Short circuit current density J_{sc} (mA/cm^2)
Flat (G0)
250/250 (G1)
250/500 (G2)
250/750 (G3)
Hexa (G6)

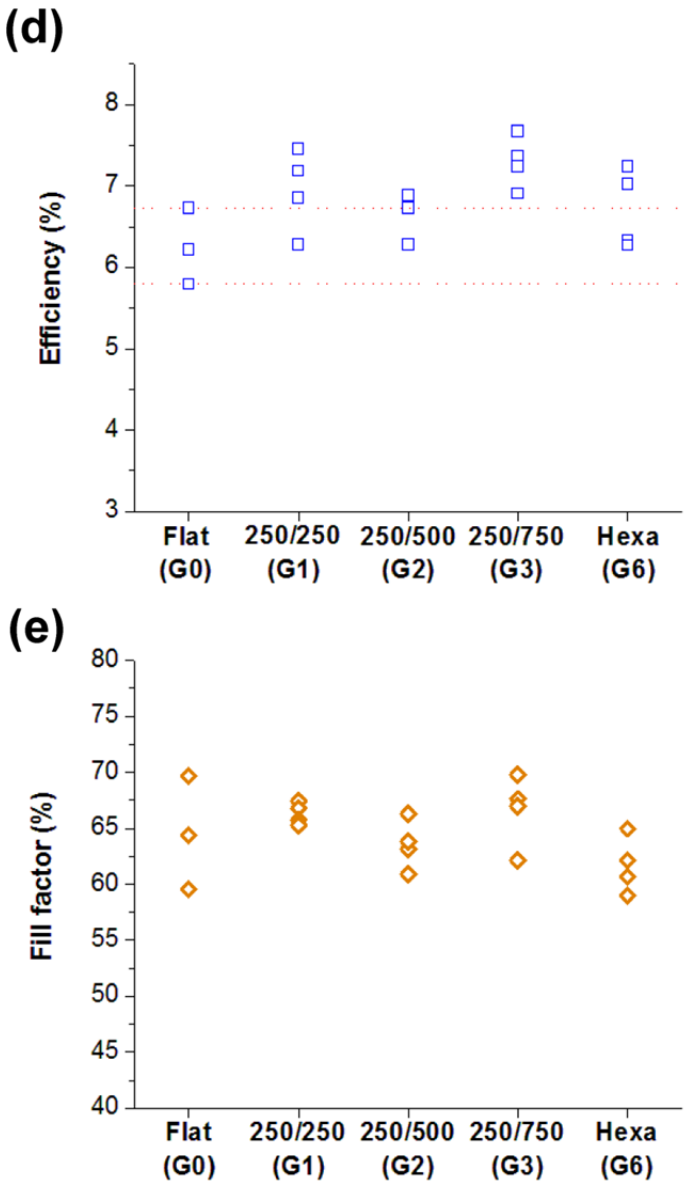
(d)
Efficiency (%)
8
7
6
5
4
3
Flat (G0)
250/250 (G1)
250/500 (G2)
250/750 (G3)
Hexa (G6)
(e)
Fill factor (%)
80
75
70
65
60
55
50
45
40
Flat (G0)
250/250 (G1)
250/500 (G2)
250/750 (G3)
Hexa (G6)

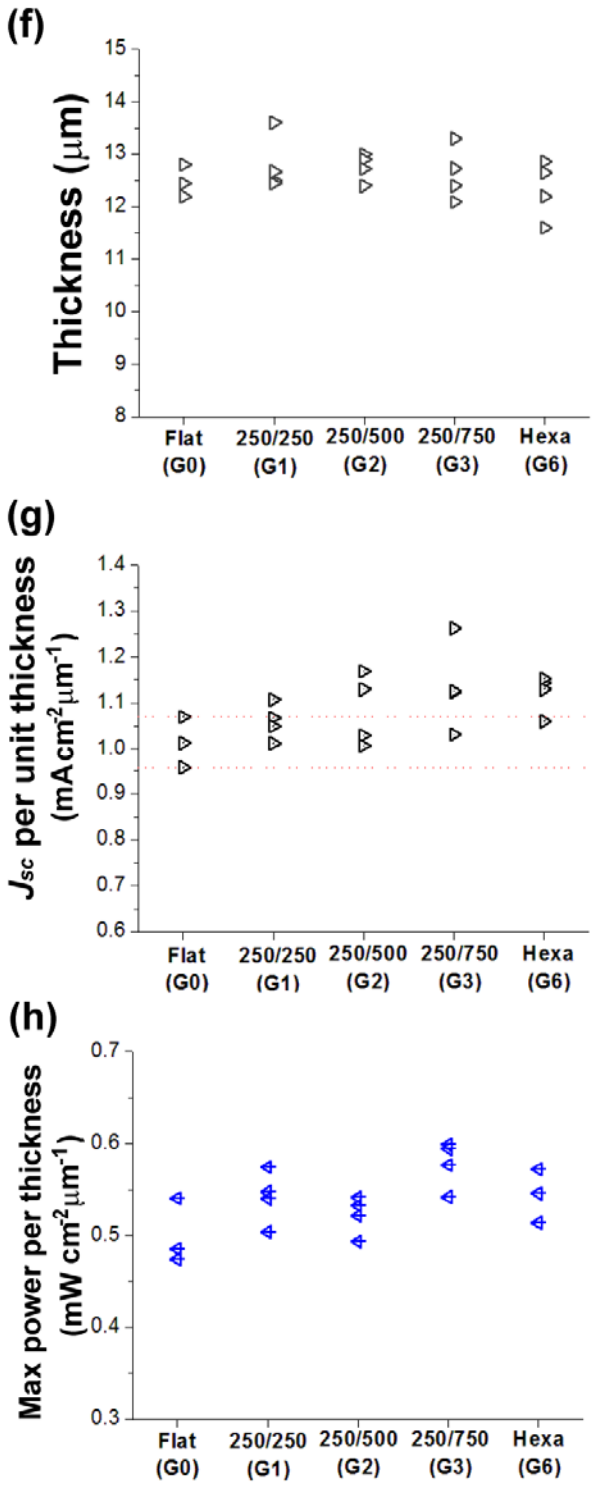

Figure 3.8 (a) Photocurrent density vs. photovoltage (***J-V***), (b) Open circuit voltage (V_{oc}), (c) short circuit current (J_{sc}), (d) global efficiency, (e) fill factor (***FF***), (f) thickness, (g) J_{sc} per unit thickness, and (h) maximum power per unit thickness of flat and patterned samples.

Figure 3.8 shows results obtained by photo-electrochemical measurements that reveal the effect of the surface photonic crystal structure on the characteristics of the DSSC. The photocurrent density vs. photovoltage (***J-V***) curves shown in Figure 3.8 (a) exhibit different short circuit current ($\boldsymbol{J_{sc}}$) values with different surface patterns. As anticipated from the IPCE spectra, all patterned samples showed higher short circuit current densities than the flat sample, which can be attributed to an increased light path via the photonic crystal structure on the surface. Figure 3.8 (b) shows the variation of the open circuit voltage ($\boldsymbol{V_{oc}}$) with surface geometry and sample by sample. Although one can see variations of open circuit voltages by surface geometry, considering the strong dependency of open circuit voltage on the thickness of the titania layers,[36] the variation may not be attributed solely to the PC effect, but rather to the combined effect of thickness and photonic crystal structure. This will be discussed later in this paragraph together with the thickness data. In Figure 3.8 (c), the short circuit current density of the different sample groups were drawn. All patterned groups showed higher short circuit current values than the flat control group, although the values partially overlap by the scatter in the data from sample to sample; the 250/750 line patterned group exhibited the maximum value. Figure 3.8 (d) presents the global efficiency of the DSSCs as a function of surface patterning. The average efficiency of the 250/250 line-patterned group lies outside of the error range of efficiency values of the flat control group. Moreover, there is no overlap in the efficiency range between the flat control group and the 250/750 line patterned group, meaning that enhancement of the efficiency by 250/750 line patterning is significant. All of the other groups also exhibited average efficiency values higher than that of the flat control group. The maximum average efficiency enhancement achieved by surface patterning, was 16.6% by the 250/750 line patterns. The other

enhancements were 10.9% (250/250 lines), 6.5% (250/500 lines), and 4.3% (hexagonal array of posts). These enhancements are remarkable, considering the extreme difference in the dimensions between the thickness of the titania layer (~13μm), and nearly negligible height of the surface structures (~135~175nm). The latter constitute only about 1.0~1.4% of the thickness of the base layer. Note that the efficiency enhancement of ~ 24% reported by Lee et al.[26] was achieved by building a substantive inverse opal/base bilayer structure through complex multistep process. By comparison, the superficial surface patterning with PRINT described here is quite an effective strategy to incorporate photonic crystal effects into DSSC devices using a much simpler process, one exhibiting comparable efficiency enhancement to the inverse opal photonic stop band. The patterns investigated in this study were selected from extant patterns, not designed intentionally for optimal effects: this implies that more enhancements in efficiency than reported in this study are likely to be achieved by optimizing the geometry of the photonic surface patterns.

Even with a larger enhancement in solar energy conversion exhibited in the IPCE and global efficiency, the optical characteristics measured do not show a clear relationship to explain the large enhancement. One possible reason for the discrepancy is the variation of thickness sample by sample, due to the manual preparation of patterned TiO_2 films. For example, Figure 3.8 (f) shows thickness variation more than 1μm even in one group. So, one may argue that the apparent enhancement is actually due to the thickness variation, rather than optical reasons by the surface PC. To clarify this, measured short circuit current density and maximum power values were normalized by the thickness of each sample. In Figure 3.8 (g) and (h), normalized short circuit current densities and maximum power generated by each DSSC to the thickness are shown. One can see in Figure 3.8 (g) that patterned groups had

higher short circuit current density values per thickness than the flat reference group, G0. Also, the normalized power values exhibit the same tendency shown in the global efficiency in Figure 3.8 (d). So, with all the variation of thickness of more than 1μm as shown in Figure 3.8 (f), the change in solar energy conversion performances cannot be disputed. So, I would try to resolve the discrepancy with various aspects in the following sections focusing on the premise that if surface PC really enhances LHE, or if there are some other processes that can explain the phenomena by improving CIE or CCE without significant change in LHE.

3.3.4 Optical simulations for light harvesting efficiency (LHE)

When measuring absorption in the integration surface (IS), an incident white light beam less than 1mm impinges on the sample and the unabsorbed portion was detected. However, in addition to the thickness variation from sample to sample, there exists another type of thickness variation within a sample: the thickness changes point by point across the sample surface, as shown in Figure 3.9.

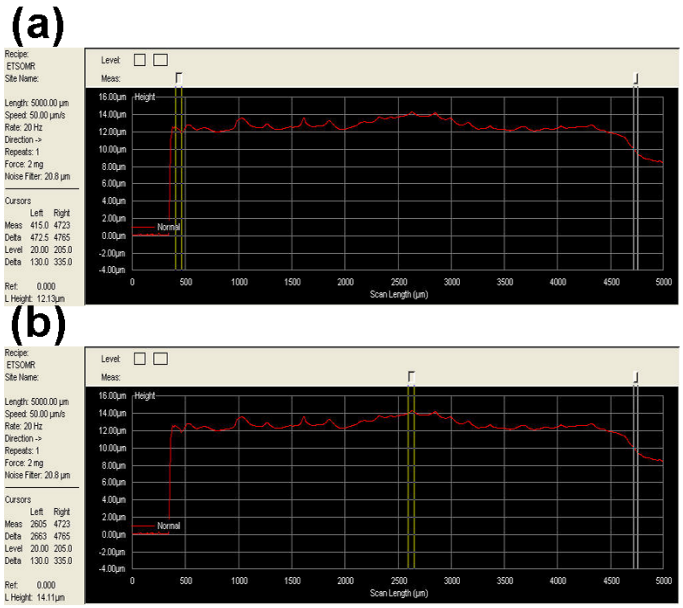

Figure 3.9 Thickness variation in a sample by position: (a) 12.13μm near the left edge and (b) 14.11μm at the center region.

In Figure 3.9 (a), the thickness value at the point marked by two yellow lines is 12.13μm, while thickness at the center of the scan (Figure 3.9 (b)) is 14.11μm, a fluctuation of about 2μm (~16%). As a result, one cannot know the exact thickness of the point of measurement, and this can prevent accurate evaluations of the thickness and possibly mislead the analysis of the absorption.

To check if the absorption spectra are almost identical to each other regardless of surface structures under experimental conditions, an optical simulation was performed assuming a typical 10μm thick, surface patterned and dye-sensitized titania film embedded in the redox electrolyte. As the refractive index of N719 dye is not available in the literature to the best of my knowledge, the refractive index of Z709 was used from the literature.[39] For simulations the DiffractMOD^{TM} (RSoft) package was used.

Figure 3.10 is the simulated absorption spectra of flat and line patterned samples assuming sensitization with the Z709 dye. As shown in the figure, there is no significant change in the absorption spectra. Although the type of dye used and density of the dye molecules in the TiO_2 film may not be equal to the experimental conditions of this study, the results shown in Figure 3.10 are in good agreement with the experimental absorption data illustrated in Figure 3.4 and 3.5. So, it can be concluded that by experiment and simulation, there is no evidence that surface PC structure really improves the LHE. Hence, it is highly probable that the large increment of solar energy conversion is due to the change in CIE or CCE assisted by changes in the optics stemming from the surface PC structure. For example, there is a strong change in reflection by the surface PC both in simulation (Figure 3.11) and experiment (Figure 3.12).

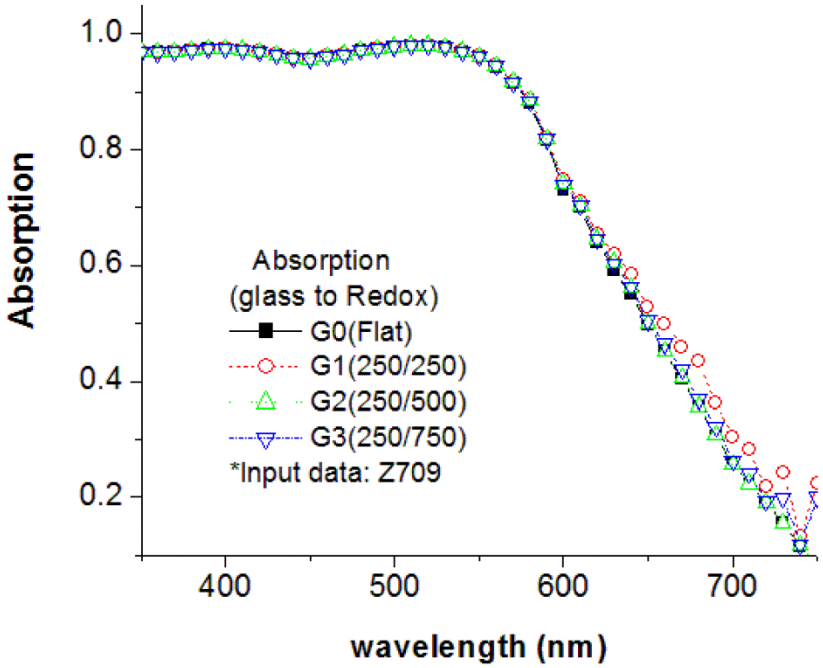

Figure 3.10 Simulated absorption spectra of flat (G0) and line-patterned groups (G1~G3).

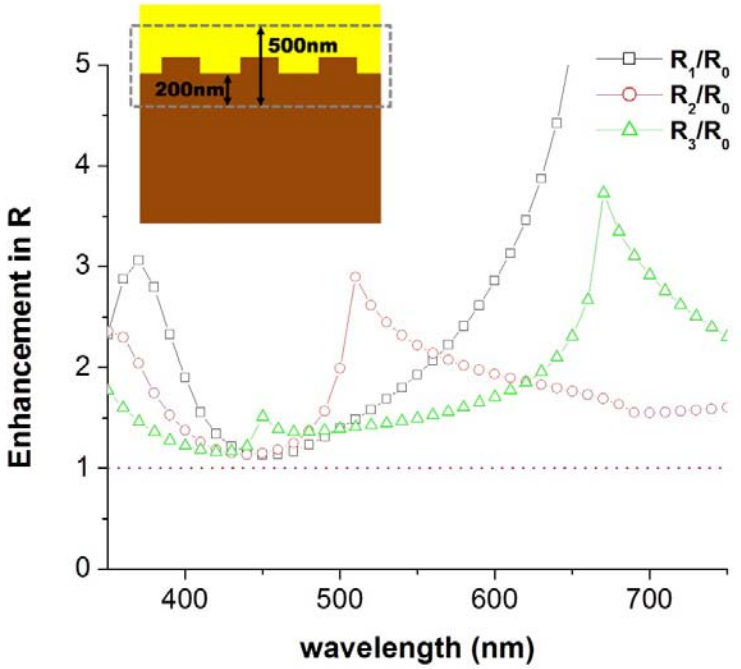

Figure 3.11 Normalized reflection of line-patterned groups to the flat (G0). The simulation was performed at the domain near the surface as shown in the figure.

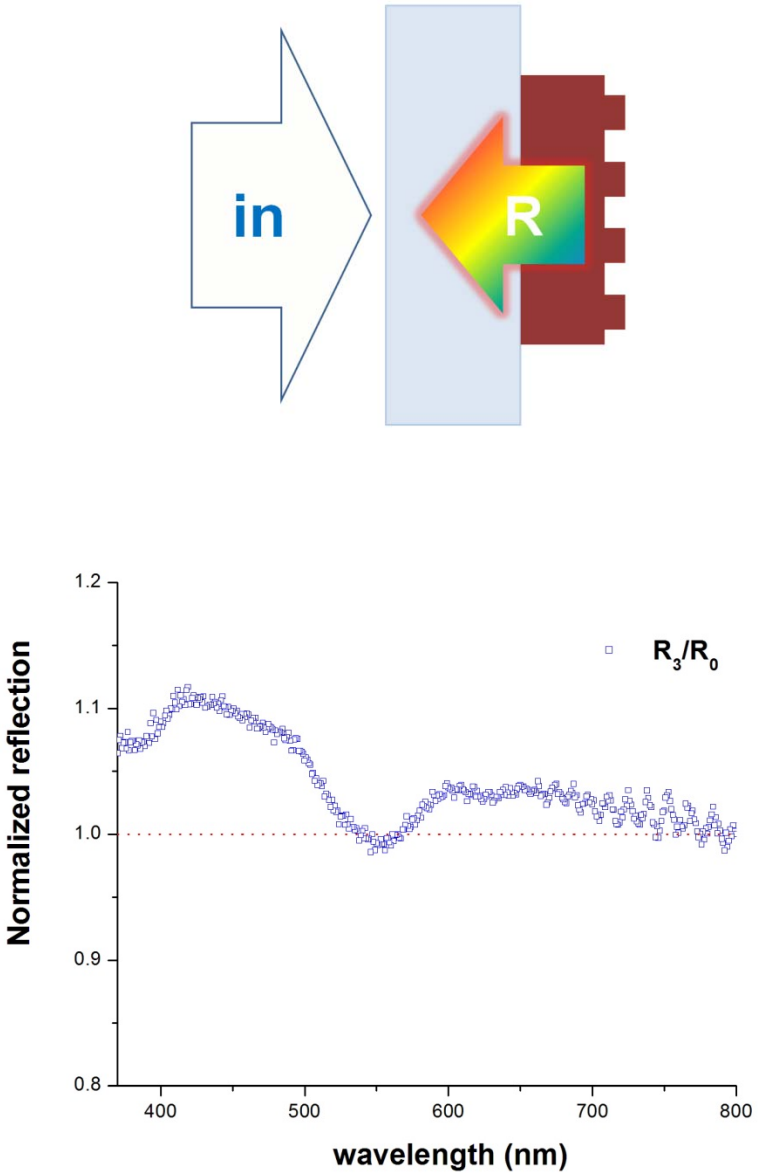

Figure 3.12 Schematic representation of reflection measurement (up) and normalized reflection of G3 (250/750) to the G0 (flat).

3.3.5 Alternative approaches to resolve discrepancies

If one tries to resolve the discrepancy between similar LHE (or absorption) levels and significant changes in the solar energy conversion (since the CIE of the conventional N3 or N719 is close to unity[2,5,40]), it would be reasonable to find a process which can be influenced

by the surface PC structure and result in an improvement in the CCE. One purpose of building PC layers on the sensitized TiO_2 layer is to localize photons as the standing wave forms in the sensitized layer.[23,24] Figure 3.13 is the field strength calculation at 360nm and 700nm wavelengths. The field strength at 360nm (Figure 3.13 (a)) decays faster than at 700nm (Figure 3.13 (c)), matching well to the predictions from Rayleigh scattering.[26,38] As the portion of 360nm photons which can reach the surface PC structure located at 12μm in the graph is small, there exists a weak interaction between incident and reflected waves only near the boundary where the PC is located, as shown in Figure 3.13 (b). However, as the intrinsic absorption of 700nm photons by the sensitized layer is weak, the decay of electromagnetic field strength is slower than that at 360nm, as indicated in Figure 3.13 (c). However, one can see higher degrees of variation in the field strength of wave throughout the whole sensitized layer having a surface PC, as illustrated in Figure 3.13 (d). However, the average field strength is expected to be almost identical, because the wave-like variations in both flat and patterned layers reveal similar levels on average. Thus, one may expect higher fluctuations of electron concentration locally changing periodically, and this may influence the diffusion of electrons and affect the CCE, even though the numbers of generated electrons are the same on a macroscopic scale.

Another possibility of improved CCE by the surface PC structure is the possibility of changes in the trap/detrap rates. When injected electrons diffuse through the TiO_2 nanoparticle network, electrons are trapped by trap states, arising from interfacial defects.[41,42] As detrapping of electrons is a thermally assisted process,[43] it is meaningful to calculate the interaction between the surface PC structure and the IR photons. According to Peters et al.,[44] photons generated by the radiative recombination processes inside the solar cell can be

trapped by the surface photonic crystal structures as shown in Figure 3.14. They suggested that photons retained inside the solar cells by the PC can be reabsorbed and generate more current.[44] However, radiation with sufficient photon energy, i.e., enough to excite the electrons at the HOMO of the dye (λ>800nm), should be counted in the absorption spectra in Figure 3.3, 3.4, or 3.10. So, one should focus on the IR which does not appear in the UV-vis measurements but is potentially energetic enough to detrap the trapped electrons. Degeneration of electrons in the dye molecule, cooling of hot electrons,[42] recombination of electrons from the conduction band of TiO_2 to the dye or electrolyte, are candidates for the internal radiative processes in DSSCs. Figure 3.15 shows the reflection of photons by the final 2μm slabs in both flat and patterned sensitized media. As the direction of recombination-related radiation would be radial, tilting was requires to calculate the reflection. If we consider a spherical surface for the radiation, there would be no change in the emission and reabsorption behavior at the other side of the hemisphere surface away from the sensitized layer surface (form angles of 90 to 180°, if we define the outward surface normal as 0°). So, it is expected that the surface PC can interact with the radiation toward the remaining half of the sphere, from 0 to 90°. However, as the sensitized medium is highly absorbing, it would be enough just to consider emission from 0 to 30°, considering the distance to the surface. In the figure, it can be seen that at angles 0° and 15°, the PC reflects more than the flat surface over the whole wavelength range considered, except the slight depression around 1.3μm and longer wavelength region for the 15° tilting angle. The PC pattern reflects close to 3 times more at the peak wavelengths of 1350nm (0°) and 900nm (15°). For a tilting angle of 30°, the situation is a little different from the first two spectra. Above 700nm, the flat surface reveals a plateau and higher reflection than the PC. However,

the PC strongly reflects photons in the visible which are energetic enough to excite the electrons in the HOMO of the dye molecule.

To confirm this hypothesis, electrochemical impedance spectroscopy (EIS) can be useful to analyze the diffusion process and recombination of electrons quantitatively by using models by Kern et al.,[45] Bisquert,[46] or Adachi et al.[47] which can handle the trap and/or recombination.

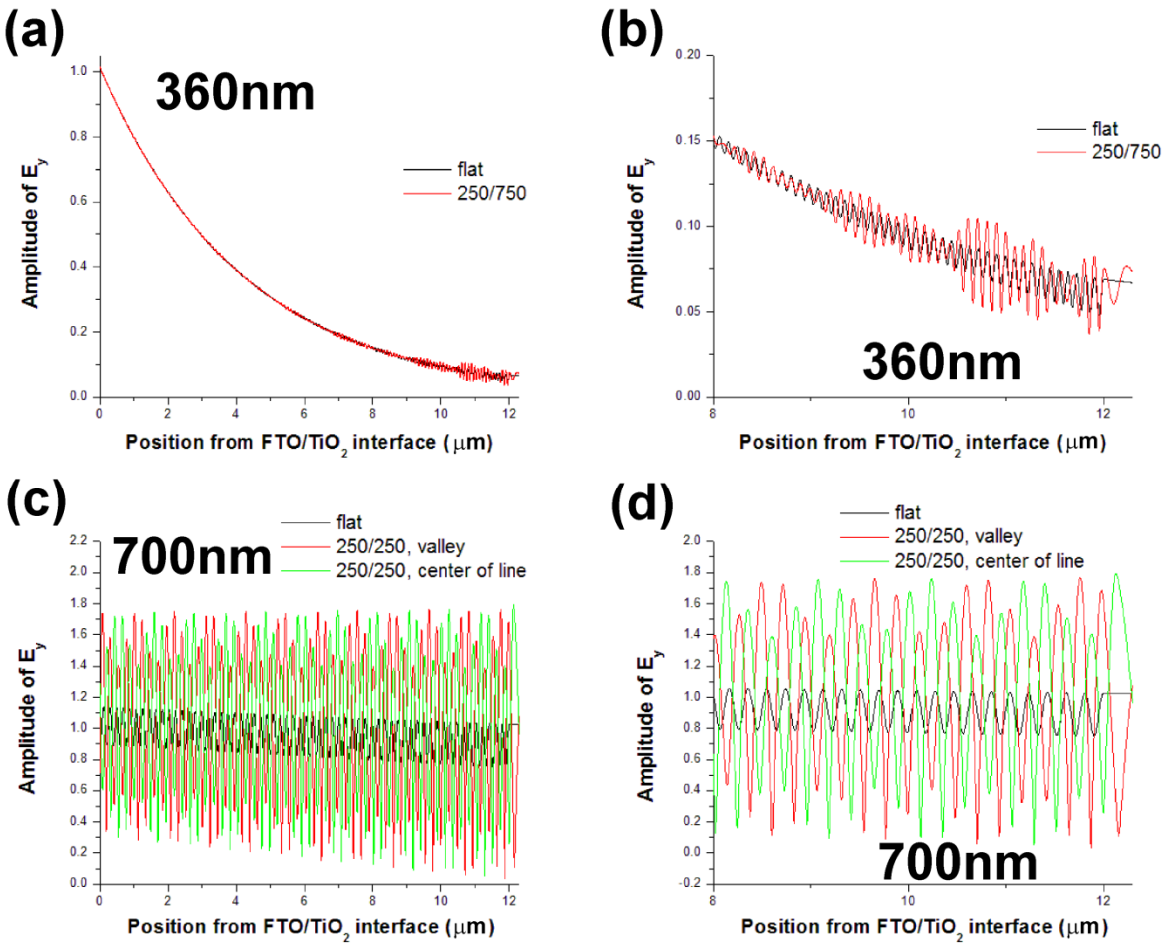

Figure 3.13 Simulated field strength of (a) 360nm and (b) 700nm light waves in the flat and 250/750 line-patterned sensitized layers of 12μm thick. (c) and (d) are showing the region close to the sensitized layer/electrolyte boundary.

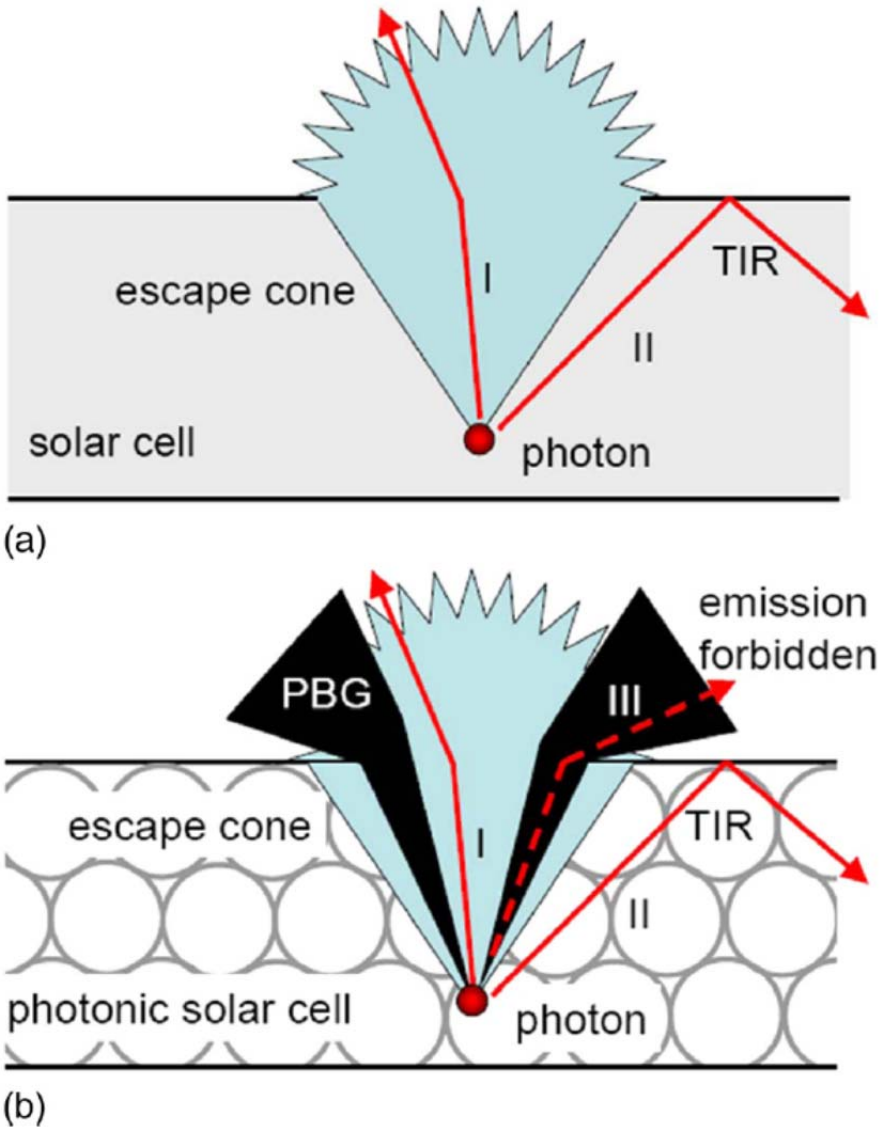

Figure 3.14 Forbidden emissions by the photonic crystal structure. (Reprinted with permission from reference 44. Copyright © 2011 American Institute of Physics)

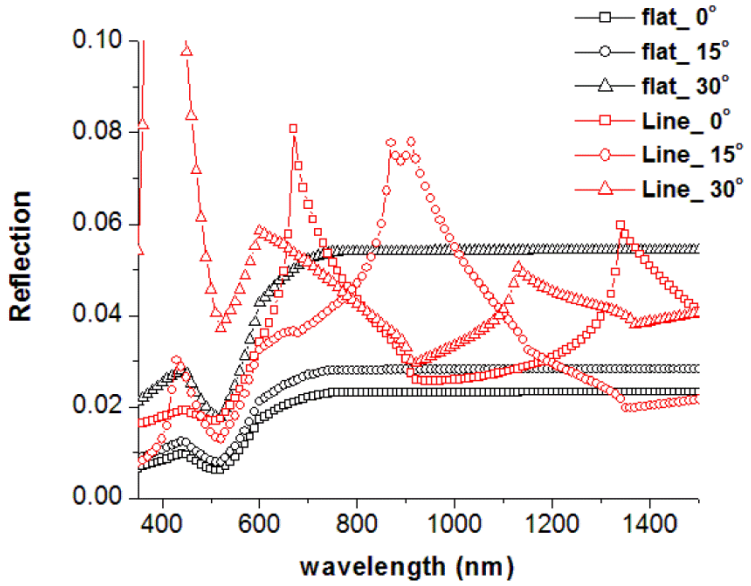

Figure 3.15 Calculation of reflection extended to 1.5μm wavelength IR by 2μm thick flat and patterned slabs by tilting angles. As the sensitized media is highly absorbing, 0 to 30° was considered to simulate the radial radiation.

3.4 Conclusions

A simple surface patterning technique using soft-lithography was applied to form photonic crystal (PC) structures on the surface of titania electrodes of a DSSC. The patterns were well replicated by PFPE molds on top of a preformed base layer without introducing interfacial defects. This enabled surface patterned DSSC devices free from electron transfer problems between the superficial photonic crystal structure layer and the thick base layer. The latter is a significant drawback in inverse opal/base bilayer structures. However, there is no direct evidence that the surface PC enhances the light absorption, unlike other studies dealing with PC-combined DSSCs. Nevertheless, PC effects by surface patterns were distinctly exhibited in the IPCE and other photoelectrochemical, solar energy, conversion measurements. The IPCE was increased by surface patterning over the whole wavelength range, and more photocurrent was generated by the photonic crystal structures, evident from

the higher short circuit current values. The global efficiency of PC samples were also higher than flat control reference samples by 4.3% to 16.6%, which is remarkable considering the minuscule dimensional increment of the surface patterns (about ~1.4% of the thickness of the titania electrodes). These observations suggest that this simple fabrication process can be readily adapted to routine DSSC fabrication.

As there is no clear change in the absorption spectra, the enhancement of global efficiency is not stemming from the improved LHE. Since there is little room for enhancement in the CIE of the commercial dyes, I suggest a hypothesis that the CCE can be improved by the surface PC structure via an enhanced field strength of the light wave in the sensitized medium and/or the faster detrapping process by the photons in the IR range which can be retained inside the DSSCs by the surface PC structure. Electrochemical impedance spectroscopy could be employed as a convincing tool for proving this hypothesis.

3.5 References

(1) O'Regan, B.; Grätzel, M. *Nature***1991**, *353,* 737—740.

(2) Nazeeruddin, M. K.; Kay, I.; Rodicio, A.; Humphry-Baker, R.; Müller, E.; Liska, P.; Vlachopouloss, N.; Grätzel, M. *J. Am. Chem. Soc.* **1993**, *115*, 6382—6390.

(3) Nazeeruddin, M. K.; Pechy, P.; Grätzel, M. *Chem. Commun.***1997**, 1705—1706.

(4) Nazeeruddin, M.K.; Zakeeruddin, S.M.; Humphry-Baker, R.; Jirousek, M.; Liska, P.; Vlachopoulos, N.; Shklover, V.; Fischer, C.H.; Grätzel, M. *Inorg. Chem.* **1999**, *38*, 6298—6305.

(5) Wang, P.; Klein, C.; Humphry-Baker, R.; Zakeeruddin, S.; Grätzel, M. *J. Am. Chem. Soc.* **2005**,*127*, 808—809.

(6) Gao, F.; Wang, Y.; Shi, D.; Zhang, J.; Wang, M. K.; Jing, X. Y.; Humphry-Baker, R.; Wang, P.; Zakeeruddin, S. M.; Grätzel, M. *J. Am. Chem. Soc.* **2008**, *130*, 10720—10728.

(7) Tennakone, K.; Kumara, G. R. R.; Kottegoda, I. R. M.; Perera, V. S. P. *Chem. Commun.* **1999**, 15—16.

(8) Keis, K.; Magnusson, E.; Lindstrom, H.; Lindquist, S. E.; Hagfeldt, A. *Sol. Energy Mater. Sol. Cells* **2002**, *73*, 51—58.

(9) Chappel, S.; Zaban, A. *Sol. Energy Mater. Sol. Cells* **2002**, *71*, 141—152.

(10) Bergeron, B. V.; Marton, A.; Oskam, G.; Meyer, G. J. *J. Phys. Chem. B* **2005**, 109, 937—943.

(11) Sayama, K.; Suguhara, H.; Arakawa, H. *Chem. Mater.* **1998**, *10*, 3825—3832.

(12) Guo, P.; Aegerter, M. A. *Thin Solid Films* **1999**, *351*, 290—294.

(13) Lenzmann, F.; Krueger, J.; Burnside, S.; Brooks, K.; Grätzel, M.; Gal, D.; Rühle, S.; Cahen, D. *J. Phys. Chem. B* **2001**, *105*, 6347—6352.

(14) Ghosh, R.; Brennaman, M. K.; Uher, T.; Ok, M.-R.; Samulski, E. T.; McNeil, L.E.; Meyer, T. J.; Lopez, R. *ACS Appl. Mater. Interfaces* **2011**, *3*, 3929—3935.

(15) Ok, M.-R.; Ghosh, R.; Brennaman, M. K.; Lopez, R.; Meyer, T. J.; Samulski, E. T. *ACS Appl. Mater. Interfaces* **2013**, *5*, 3469—3474.

(16) Zhu, K.; Neale, N.; Miedaner, A.; Frank, A. *Nano Lett.* **2002**, *7*, 69—74.

(17) Gong, D.; Grimes, C.A.; Varghese, O.K.; Hu, W.C.; Singh, R.S.; Chen, Z.; Dickey, E.C. *J. Mater. Res.* **2001**, *16*, 3331—3334.

(18) Paulose, M.; Shankar, K.; Yoriya, S.; Prakasam, H. E.; Varghese, O.K.; Mor, G.K.; Latempa, T.A.; Fitzgerald, A.; Grimes, C. A. *J. Phys. Chem. B* **2006**, *110*, 16179—16184.

(19) Stergiopoulos, T.; Ghicov, A.; Likodimos, V.; Tsoukleris, D. S.; Kunze, J.; Schmuki, P.; Falaras, P. *Nanotechnology* **2008**, *19*, 235602.

(20) Usami, A. *Chem. Phys. Lett.* **1997**, *277*, 105—108.

(21) Nishimura, S.; Abrams, N.; Lewis, B. A.; Halaoui, L. I.; Mallouk, T. E.; Benkstein, K. D.; van de Lagemaat, J.; Frank, A. J. *J. Am. Chem. Soc.* **2003**, *125*, 6306—6310.

(22) Halaoui, L. I.; Abrams, N. M.; Mallouk, T. E. *J. Phys. Chem. B* **2005**, *109*, 6334—6342.

(23) Mihi, A.; Míguez, H. *J. Phys. Chem. B* **2005**, *109*, 15968—15976.

(24) Mihi, A.; López-Alcaraz, F. J.; Míguez, H. *Appl. Phys. Lett.* **2006**, *88*, 193110—193113.

(25) Herman, L.A.; Yip, C.H.; Wong, C.C. *J. Nanosci. Nanotechnol.* **2010**, *10*, 4657—4662.

(26) Lee, S.-H. A.; Abrams, N. M.; Hoertz, P. G.; Barber, G. D.; Halaoui, L. I.; Mallouk, T. E. *J. Phys. Chem. B* **2008**, *112*, 14415—14421.

(27) Guldin, S.; Hüttner, S.; Kolle, M.; Welland, M. E.; Müller-Buschbaum, P.; Friend, R. H.; Steiner, U.; Tétreault, N. *Nano Lett.* **2010**, *10*, 2303—2309.

(28) Johnson, S. G.; Joannopoulos, J. D. *Acta Mater.* **2003**, *51*, 5823-5835.

(29) Zhao, X.-M.; Xia, Y.; Whitesides, G. M. *J. Mater. Chem.* **1997**, *7*, 1069-1074.

(30) Rolland, J. P.; Van Dam, R. M.; Schorzman, D. A.; Quake, S. R.; DeSimone, J. M. *J. Am. Chem. Soc.***2004**, *126*, 2322−2323.

(31) Rolland, J. P.; Hagberg, E. C.; Denison, G. M.; Carter, K. R.; DeSimone, J. M. *Angew. Chem. Int. Ed.***2004**, *43*, 5796−5799.

(32) Ko, D.-H.; Tumbleston, J. R.; Zhang, L.; Williams, S.; DeSimone, J. M.; Lopez, R.; Samulski, E. T. *Nano Lett.* **2009**, *9*, 2742−2746.

(33) Kim, J.; Koh, J. K.; Kim, B.; Kim, J. H.; Kim. E. *Angew. Chem. Int. Ed.* **2012**, *51*, 6864—6869.

(34) Maynor, B. W.; LaRue, I.; Hu, Z.; Rolland, J. P.; Pandya, A.; Fu, Q.; Liu, J.; Spontak, R. J.; Sheiko, S. S.; Samulski, R. J.; Samulski, E. T.; DeSimone, J. M. *Small* **2007**, *3*, 845-849.

(35) Hampton, M. J.; Williams, S. S.; Zhou, Z.; Nunes, J.; Ko, D.-H.; Templeton, J. L.; Samulski, E. T.; DeSimone, J. M. *Adv. Mater.* **2008**, *20*, 2667−2673.

(36) Wang, Z.-S.; Kawauchi, H.; Kashima, T.; Arakawa, H. *Coord. Chem. Rev.* **2004**, *248*, 1381−1389.

(37) Zeng, L.; Yi, Y.; Hong, C.; Liu, J.; Feng, N.; Duan, X.; Kimerling, L. C.; Alamariu, B. A. *Appl. Phys. Lett.* **2006**, *89*, 111111.

(38) Bohren, C. F.; Huffman, D. R. *Absorption and scattering of light by small particles*; John Wiley & Sons, Inc.: Weinheim, Germany, 1983.

(39) Wenger, S. Strategies to Optimizing Dye-Sensitized Solar Cells: Organic Sensitizers, Tandem Device Structures, and Numerical Device Modeling. Ph. D. Dissertation, École Polytechnique Fédérale de Lausanne, Lausanne, Switzerland, 2010.

(40) Yang, Z.; Xu, T.; Gao, S.; Welp, U.; Kwok, W.-K. *J. Phys. Chem. C* **2010**, *114*, 19151–19156.

(41) Yang, Z.; Gao, S.; Li, T.; Liu, F.-Q.; Ren, Y.; Xu, T. *ACS Appl. Mater. Interfaces* **2012**, *4*, 4419–4427.

(42) Grätzel, M. *Inorg. Chem.* **2005**, *44*, 6841—6851.

(43) van de Lagemaat, J.; Park, N.-G.; Frank, A. J. *J. Phys. Chem. B* **2000**, *104*, 2044—2052.

(44) Peters, M.; Goldschmidt, J. C.; Bläsi, B. *J. Appl. Phys.* **2011**, *110*, 043104.

(45) Kern, R.; Sastrawan, R.; Ferber, J.; Stangl, R.; Luther, J. *Electrochim. Acta* **2002**, *47*, 4213-4225.

(46) Bisquert, J. *J. Phys. Chem. B* **2002**, *106* (2), 325-333.

(47) Adachi, M.; Sakamoto, M.; Jiu, J.; Ogata, Y.; Isoda, S. *J. Phys. Chem. B* **2006,** *110,* 13872-13880.

CHAPTER 4

PATTERNED ITO SUBSTRATE FOR ENHANCED ELECTRON COLLECTION IN THE DYE-SENSITIZED SOLAR CELLS

4.1 Introduction

The dye-sensitized solar cell (DSSC) has been intensively studied as one of the strong candidates for low-cost photovoltaics during the last 20 years since the seminal report of the high efficiency (~7.1%) DSSC by O'Regan and Grätzel.[1] To achieve higher power conversion efficiency of the DSSCs, researchers have mainly focused on the development of new dyes absorbing a wider spectrum of light[2-6] and novel electrolytes,[7-9] and/or the application of new metal oxide supports, e.g. ZnO,[10,11] SnO_2,[10,12,13] or Nb_2O_5.[14-18]

In addition to the development of new materials, there have been other approaches focusing on the optimization and/or alteration of the cell structure for optical[18-28] or charge transportational[29-40] purposes. Optical elements were incorporated into the DSSC in the form of an additional layer of larger TiO_2 particles to enhance scattering and internal reflection of light[19] and photonic crystals (PCs) were incorporated in the form of inverse opal layers.[20-26] Additionally, surface patterns,[18,27] or 1 dimensional multilayers[28] have been used to reflect unabsorbed photons back to the mesoporous nanoparticle (NP) network. Structural alterations of the DSSCs were mainly introduced to facilitate the diffusion of electrons and suppress recombination losses which arose from the nature of the NP network: although it is

a highly optimized structure in terms of light absorption with imaximized surface area (780[1] or typically 1000-fold more than the geometric area),[41] to accommodate sufficient number of dye molecules, injected electrons from the dye molecules must diffuse through the complex NP network and spend milliseconds to several seconds before being collected by the TCO layer.[42] During the diffusion process, electrons experience millions of trapping/detrapping events at defect sites[43,44] and a significant portion of them are lost by interfacial recombination.[41] So, vertically textured architectures in the form of nanowires[29-33] or nanotubes[34-40] were adapted to reduce both the number of defect sites and the electron diffusion length to the TCO. However, compared to the random NP network of metal oxide (typically TiO_2) in the conventional DSSCs, as the surface area of these one-dimensional (1-D) structures should be inherently smaller and consequently load less amount of dye. As a result branched nanostructures (nanotripod,[45] nanoflower,[46] nanoforests[17,47-49]) were developed to increase surface area while maintaining the benefit of the vertical architecture. Nonetheless, contrary to the huge number of studies dealing with the improvement and alteration of the metal oxide structure mentioned above, relatively speaking, negligible attention has been paid to the TCO layer and only limited numbers of investigations modifying the TCO structure are available in the literature.[42,50-53] As the conductivity of the TCO is several orders of magnitude higher than that of the mesoporous TiO_2 layer, modification of TCO (or any conductive material with acceptable transmittance of light) by inserting substructures into the mesoporous NP layer can provide shortcuts to electrons and effectively shorten the electron diffusion pathway, as illustrated in Figure 4.1. Martinson et al.[50] reported architecture of concentric ITO nano layers on the anodic aluminum oxide (AAO) template formed by atomic layer deposition (ALD) to reduce electron collection

lengths. Yang et al.[42,51,52] reported several methods for altering TCO structures by adapting a square array of Ni micropillars (3μm in diameter, 10μm in period) fabricated by using photolithography and electrochemical deposition,[42] inverse opal FTO,[51] or random nanoparticle network of FTO substrates.[52] Wang et al.[53] fabricated patterns several hundred nanometers in height on commercially available FTO substrates (550~600nm thick) for light trapping by using nanoimprint and reactive ion etching (RIE). With these inventive attempts, all of these methods rely on complex and/or high cost processes: use of photolithography,[42] nanotemplates,[50,51] atomic layer depositon,[50,52] or RIE.[53] So, there is a strong demand for a new method for fabricating patterns on TCO that is easy and is low cost, and that can be used in combination with the simple doctor blading employed to manufacture conventional DSSCs.

I describe a simple ITO patterning method based on the soft-lithography techniques[54] to form substructures on the several micrometer scale in the DSSCs in order to reduce electron collection lengths. Perfluoropolyether (PFPE)[55,56] was used to replicate patterns fabricated on a Si master, and transfer them to form a patterned ITO architecture on commercial FTO electrodes. Only manual fabrication methods like soft-lithography and doctor blading were used to build all of the structural elements of the DSSCs having patterned TCO substructure in order to impact the performance of DSSCs with minimal fabrication costs. Optical characteristics and power conversion performances of the patterned TCO (patterned ITO/FTO coating) DSSCs were analyzed and compared to the flat TCO DSSCs.

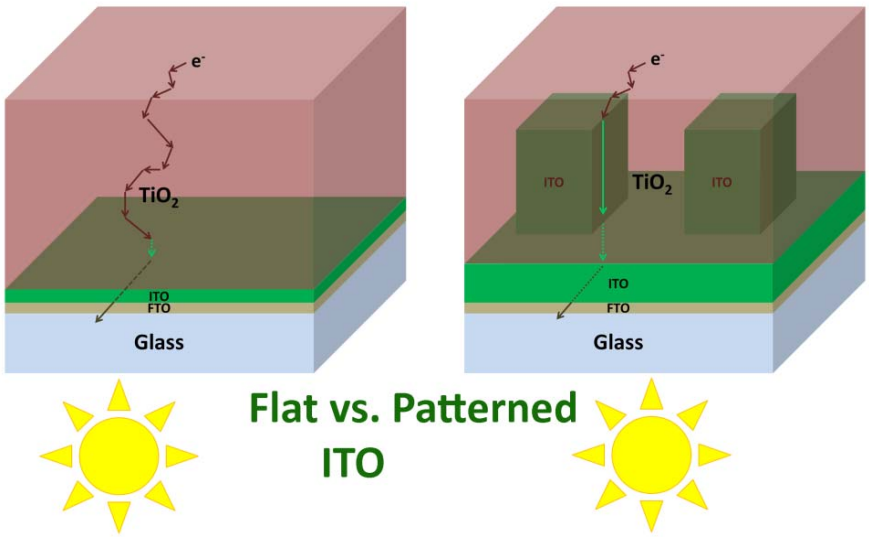

Figure 4.1 Comparison of the flat and patterned architecture of ITO layer depicting reduced electron diffusion length to the TCO in the DSSC.

4.2 Experimental

4.2.1 Fabrication of the ITO paste

Cubic arrays of rectangular ITO posts (5×5×6.5 μm (W×W×H), 10 μm period) were fabricated starting from ITO nanoparticles by using a soft-lithography technique. First, an ITO paste was prepared: 500mg of ITO nanoparticles (17-28nm, 99.5%, In_2O_3:SnO_2=90:10, Nanotek, Alfa Aesar) and 1ml of ammonium hydroxide solution (29.53%, Fisher Scientific) were blended, and 250mg of hydroxypropyl cellulose (M_w: 100,000, Aldrich) was added to this mixture in the form of 10wt% solution in deionized water, and then stirred overnight for homogenization. This paste can be used for soft-lithography after further concentrating and spin-casting for flat reference ITO after dilution.

4.2.2 Fabrication of patterned PFPE mold for soft-lithography

For soft-lithography, PFPE molds were used to fabricate a patterned ITO layer on top of the FTO coated glass. The PFPE molds were fabricated using the method reported by Hampton et al.:[57] A photo-curable PFPE precursor solution (donated by Liquidia

Technologies Inc.) consisting of 1000g/mol PFPE (an α, Ω–functionalized dimethacrylate and 2, 2-diethoxyacetophenone as the photoinitiator) was poured on a Si master and spread evenly. After purging with nitrogen gas for 3min to remove oxygen in the precursor solution, PFPE was polymerized by UV radiation for 3min. The polymerized PFPE mold was carefully removed from the Si master and cleaned with ethanol to remove the uncrosslinked residue on the mold surface away.

4.2.3 Preparation of the anodes on top of the patterned TCO substrates

The overall procedure to prepare sensitized TiO_2 films on patterned TCO is described in Figure 4.2. FTO coated glass substrates (15Ω/sq, 2.3mm thick, Hartford glass) were cleansed in acetone, isopropanol, and deionized water by sonication for 20min each, followed by a heat treatment at 500°C for 10min to completely eliminate organic residues. A small amount of ITO paste was spread evenly onto the patterned side of the PFPE mold and that was placed onto an FTO coated glass substrate as shown in Figure 4.2 (b).

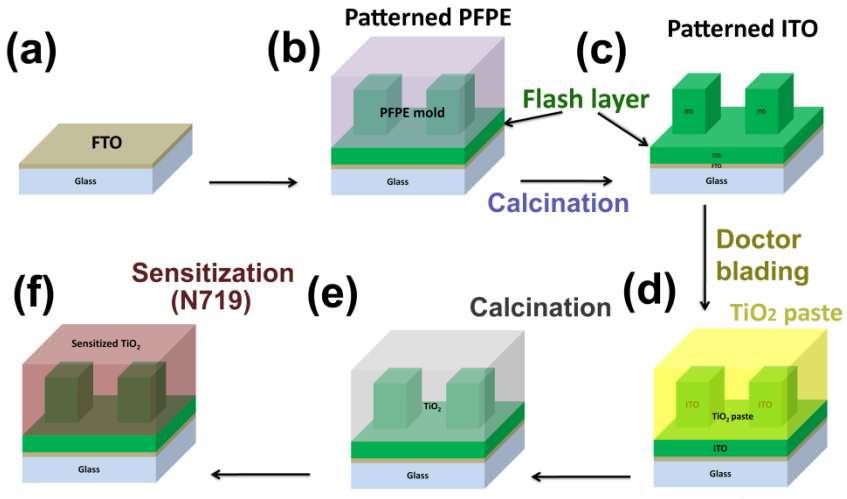

Figure 4.2 Procedures for the fabrication of the anode of the DSSC with patterned ITO geometry.

Mild pressure was applied to the PFPE mold/ITO paste/FTO coated glass substrate assembly to ensure good contact throughout the drying step (80°C oven in the air). After complete drying, the PFPE mold was carefully removed and the patterned, dry ITO layer was calcined in a tube furnace under various heating conditions to obtain sintered patterns of ITO as suggested in Figure 4.2 (c). After calcination, one group of calcined ITO patterns was heat treated in a hydrogen/nitrogen mixture (5:95) to restore the conductivity of the patterned ITO substrates.[58] Calcined ITO films were trimmed to 4.5×4.5mm squares, and tape spacers (3M, magic scotch tape) were placed around the ITO layer to delineate that exposed area for the subsequent doctor blading step. A TiO_2 paste (DSL 18NR-T, Dyesol) was then doctor bladed onto the patterned ITO layers, and tape spacers were removed immediately (Figure 4.2(d)). Doctor bladed TiO_2 films were dried at 80^{o}C on a hot plate and calcined in a tube furnace at 500^{o}C. After calcination, the edges of the calcined TiO_2 films were trimmed so that the TiO_2 films do not contact FTO substrate directly. For reference, flat ITO films about 200nm were fabricated by spin-casting a diluted ITO paste (3000rpm, double layers) and calcined in the tube furnace. After calcination, TiO_2 layers were formed on them with the same method used for the patterned ITO. TiO_2 films were also prepared directly on the bare FTO coatings for comparison.

4.2.4 Assembly of the DSSCs

To compare the solar energy conversion performances of DSSCs with embedded ITO structures and conventional flat reference DSSCs, calcined TiO_2 films were sensitized with dyes for light absorption (Figure 4.2 (f)): N719 dye (*Cis*-bis(isothiocyanato)bis(2,2′-bipyridyl-4,4′-dicarboxylato) ruthenium(II) bis(tetrabutyl ammonium) ($RuL_2(NCS)_2$-2TBA, also known as Ruthenium535 bis-TBA, Solaronix) was dissolved in a 1:1 mixture of

acetonitrile and t-butanol (0.3mM), and the solution was sonicated for 30min. The dye solution was then centrifuged to remove residual aggregates. Before sensitization, TiO_2 films were heat treated at 500°C for 30min and cooled down to 80°C, and carefully submerged into the N719 dye solution. The samples were soaked in the solution overnight for sensitization. After sensitization, the samples were washed with acetonenitrile to remove unabsorbed dye.

4.2.5 Characterization of the DSSC structure and photoelectrochemical performances

For optical characterization, UV-visible absorption spectra were measured with an integration sphere, Cary 5000 fitted with DRA 2500. For structural analysis, patterned ITO substrates and cross-section of the patterned TCO/mesoporous TiO_2 film assembly were analyzed with a scanning electron microscopy (SEM, S-4700, Hitachi).

To characterize the performance of the DSSC's, sealed DSSC's were prepared following the methods by Wang et al.,[59] using a 100μm Surlyn film (Solaronix) and one hole for electrolyte injection. A solution of 0.1M LiI (99.9%, Aldrich), 0.05M I_2 (≥99.99%, Aldrich), 0.5M 1,2-dimethyl-3-propylimidazolium iodide (≥98%, Tokyo Chemical Industry), 0.5M t-butylpyridine (96%, Aldrich), and 0.1M guanidinium thiocyanate (99%, Aldrich) in acetonitrile (99.9%, Fisher Scientific) was prepared for redox electrolyte. A 75W Xe Oriel 6251/Oriel Cornerstone 260 monochromator was coupled with a Keithley 6517A current meter for measuring the incident photon-to-current conversion efficiency (IPCE). The photocurrent density-photovoltage curves of the cells were obtained using an AM 1.5 solar simulator (NEWPORT 1000-W Xe lamp and an AM 1.5 filter) together with a Keithley 2400 source meter.

4.3 Results and Discussion

4.3.1 Structural analysis of the DSSC with patterned ITO substructures

The SEM images of the patterned ITO and TiO_2/patterned TCO cross-section are shown in Figure 4.3. The calcined ITO structures exhibited mesoporous structure made up of sintered ITO nanoparticles. As shown in the inlet of the left figure, ITO posts conserved their dimensions close to the original values in the Si master (5×5×6.5μm, a cubic array with a 10μm period). So, soft-lithography using a paste form of ITO nanoparticles is clearly an appropriate way to transfer the patterns of the Si master to the FTO coated glass substrate for altering DSSC structure on a several micrometer scales. Furthermore, one can clearly see from the center image that the ITO patterns retained the original architecture after the post processes (doctor blading of the TiO_2 paste and another calcination step) to convert the paste to a mesoporous TiO_2 layer. Although the ITO posts experienced two calcination steps, the initial size of the ITO nanoparticle is 14 to 28nm, a similar particle size to the anatase TiO_2 (typically around 20nm), the calcination time is not long enough for distinct coarsening of ITO particles. The overall nanostructures of the TiO_2 and embedded ITO posts are almost identical with similar porosity. In the cross-sectional images of Figure 4.3, a continuous ITO layer is observed on top of the FTO coating layer: this flash layer[60] was formed during the soft-lithography steps because of the good wetting property of the ITO paste on the FTO coating layer and/or on the PFPE mold. For patterning, a very small amount of ITO paste was spread evenly onto the negatively patterned PFPE to fill the negative pattern on the PFPE mold. However, the ITO paste does not only fill the cavities in the negative pattern of the mold, but also forms a thin layer on the PFPE mold surface. When the ITO paste was transferred onto the FTO coated glass, the thin paste layer stuck to the FTO layer and formed a continuous flash layer. This flash layer helps the posts maintain their original position and

stand upright on the FTO substrate during the removal of the PFPE film after drying. However, the manual paste spreading process cannot control the thickness of the flash layer. As a result, the precision and the variation of flash layer thickness point by point from sample to sample or within a sample is unavoidable and can potentially be a source of large error in terms of electrical and optical fluctuations of the TCO properties.

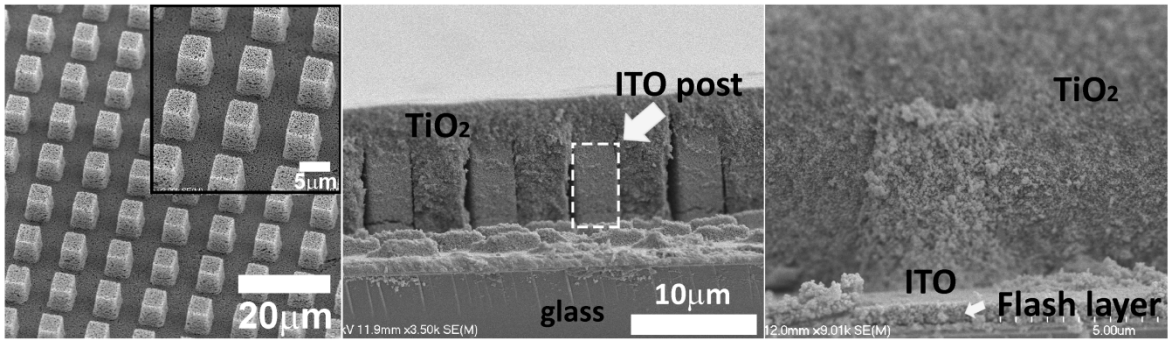

Figure 4.3 SEM images of the patterned ITO and cross-sections of TiO2/patterned TCO architecture for anode of the DSSC.

4.3.2 Optical Characterization

Under ordinary circumstances, commercially available flat ITO coated glass is regarded as virtually 'transparent' and doesn't cause any serious issues when used as simple substrates of electronic devices or DSSCs. Yet, in this investigation, as the transmittance of the ITO patterns several micrometers high is to be smaller than that of the bare FTO coated glass, the difference in light intensity reaching to the sensitized TiO_2 layer can be so different as to make it difficult to draw out the true structural effect of the patterned TCO geometry. So, it is necessary to define another group of DSSCs with a flat intermediate ITO layer on the FTO coating so that equal numbers of photons reach the sensitized TiO_2 layer. In terms of photoelectrochemistry, this can ensure both groups of DSSCs encounter identical photoelectrochemical processes originating from the intermediate ITO layers (flat or

patterned). By optical simulation using the DiffractMOD^{TM} (RSoft), transmission spectra of both flat and patterned ITO were calculated and the optimum thickness of the flat ITO generating equal transmittance to that of the ITO post arrays at 530nm was found to be around 100nm. Nonetheless, as both flat and patterned ITO layers calcined were mesoporous bodies scattering photons severely, it should be regarded as a composite of metal oxide and air,[61] and as a result the refractive index values in the simulation cannot be equal to data found for dense materials. So, the thickness was tuned experimentally using the calculation result as a starting point.

The transmission spectra of a 200nm flat ITO layer and patterned ITO posts on FTO coated glass substrates are shown in Figure 4.4. Figure 4.4 (a) shows transmission of incident light by one flat ITO and two patterned ITO layers, and Figure 4.4 (b) is constructed by normalizing the transmission spectra of the patterned samples (namely P1 and P2) to the spectrum of flat ITO layer. One can see that the patterned ITO layers transmit less light over the whole wavelength range measured. The difference between flat and patterned ITO layers in transmission was more distinct in the blue range, up to 36% at 370nm, as shown in Figure 4.4 (b). As the photons of higher energy scatter more in the media by Rayleigh scattering,[26] the biggest difference in transmission is expected in the blue region considering the mesoporous morphology and 6.5μm pattern height. A more important feature revealed in Figure 4.4 is that there exists large fluctuations amongn transmission spectra of patterned ITO samples. Variations of the flash layer thickness seems responsible for this large degree of fluctuation, considering the uncontrollable nature of the flash layer thickness during the manual soft-lithography steps. The fluctuation of transmission spectra among individual patterned samples essentially causes the volume of sensitized TiO_2 to vary, and as a result, a

greater scattering in the photoelectrochemical energy conversion is expected than in the DSSCs with flat ITO layers or those built just on the bare FTO coated glasses. In the SEM analysis, flash layers were measured to be from 400nm to 2μm, and typically around 700nm ~ 1μm range. The effect of the flash layer thickness will be discussed further in the solar energy conversion section.

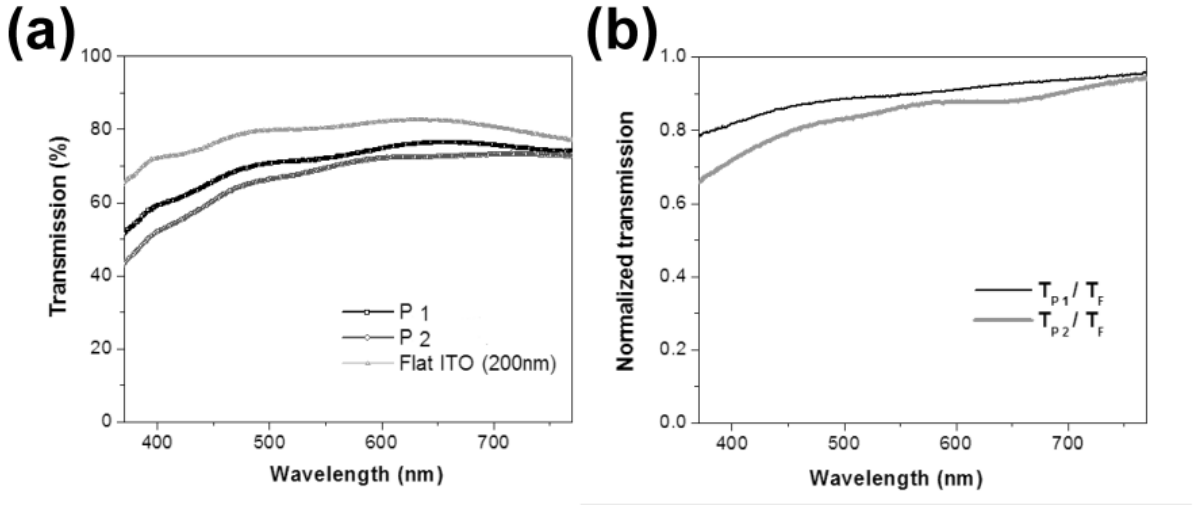

Figure 4.4 Transmission spectra of a flat and 2 patterned ITO layers formed on FTO coated glass substrate: (a) transmission by the flat ITO layer is larger than those of patterned ITOs in the whole wavelength range measured and (b) normalized transmission spectra of patterned samples to the flat ITO layer reveal fluctuation between patterned samples. The discrepancy between flat and patterned geometry is distinct especially in the blue region.

4.3.3 Resistivity of the ITO

As the motivation of the patterning on the TCO is based on the idea that TCO has sufficiently high conductivity to provide a fast diffusion path to electrons, it is necessary to find optimized process conditions for patterned ITO preparation in terms of its resistivity. Figure 4.5 shows the resistivity data of calcined ITO films with various calcination conditions. In the figure, samples with diamond symbols were calcined in a mild air stream to the final temperatures (heating rate: 2K/min). One can see a 'V' shaped curve as the final temperature value increases and this seems to be caused by the competition of two different

mechanisms to lower and raise the resistivity respectively: sintering of ITO nanoparticles would result in enhanced connections among nanoparticles and lower the resistivity of the calcined ITO films, while degradation of the individual ITO nanoparticles during the heat treatment in air[62] would cause the degradation of electrical conductivity of the whole ITO film. In Figure 4.5, the fall in resistivity from 400°C to 500°C is thought to be dominated by the sintering of ITO nanoparticles by increasing thermal treatment temperature, but the resistivity rise from 500°C to 600°C can be interpreted as the degradation of the discrete ITO nanoparticles overwhelming the possible resistivity decrease by further sintering at 600°C. On the other hand, the resistivity data of ITO films calcined in a closed tube furnace show different behavior. In Figure 4.5, the circular symbols represent resistivity data of ITO films calcined in a closed tube furnace (heating rate of 2K/min to 500°C and 600°C, followed by a holding time (1hour) at the final temperatures for further sintering), and square symbols show resistivity data of samples calcined in the closed tube furnace, followed by additional heat treatment in the H_2/N_2 mixture to recover the conductivity of the ITO films.[58] When calcined in a closed tube in the absence of an air supply, the resistivity of ITO films further decreased to 600°C, and this implies that the sintering mechanism extended its dominant range to 600°C, and degradation of the ITO nanoparticles was diminished in the static atmosphere in the tube. Moreover, ITO films calcined in a closed tube with holding time exhibited lower resistivity than samples treated with air stream at all temperatures. As electrically degraded ITO has a lower metal to oxygen ratio,[62] it is reasonable to interpret the resistivity data in terms of the oxygen partial pressure in the quartz tube under different calcination conditions. When the ITO films were calcined in a mild air stream to effectively remove carbonaceous components in the ITO paste, the oxygen pressure was kept nearly constant and further

oxidation of ITO at the elevated temperatures could occur, resulting in a decreased metal to oxygen ratio and leading to significant degradation of the electrical conductivity. However, when ITO films were calcined in a closed quartz tube, some of the initial oxygen was consumed to burn out the polymeric phase in the ITO paste and the oxygen pressure gradually falls to an equilibrium value at the end of the sintering process. As a result, the degradation of ITO particles is not so influential and the sintering of ITO nanoparticles may be dominant under that condition.

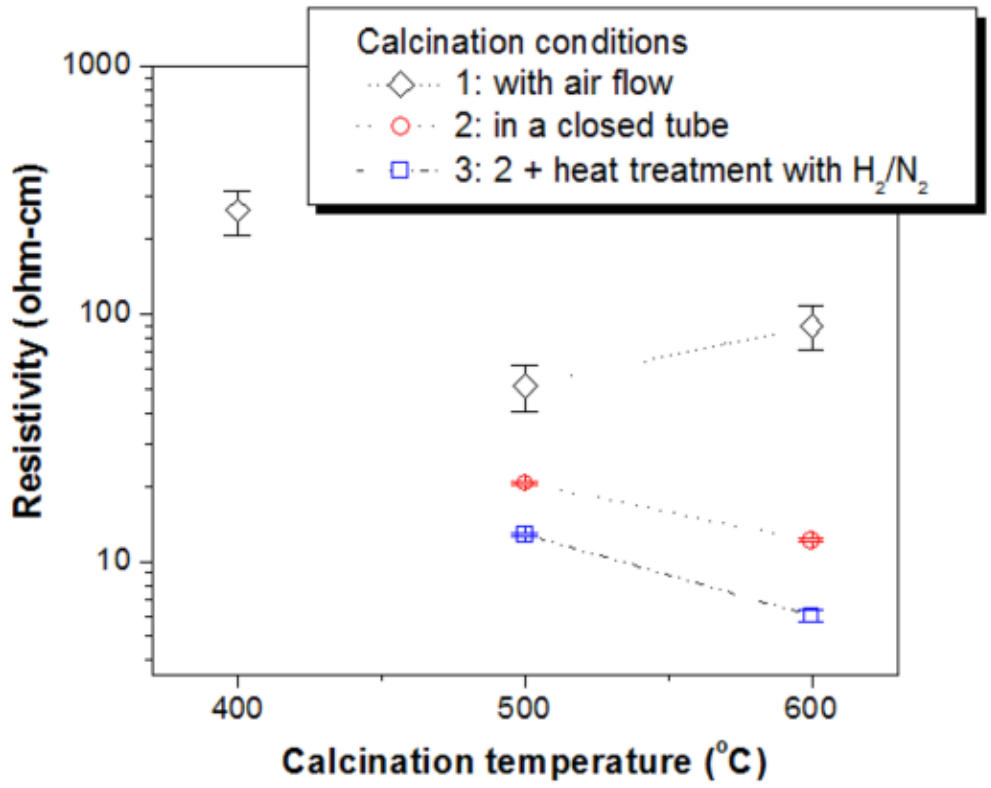

Figure 4.5 Resistivity of ITO films at various calcination conditions: 2K/min to final temperature without holding under mild air stream (◊), 2K/min to final temperature with 1hour holding time in the closed quartz tube (○), and additional H_2/N_2 treatment at 300°C (□).

An additional heat treatment in 5% hydrogen/nitrogen mixture was performed to lower the resistivity of the ITO films, and the results are shown in Figure 4.5. One can see

that the resistivity of ITO films dropped to about a half of the initial resistivity, e.g. samples calcined at 600°C, 12.2Ω-cm to 6.0Ω-cm, after heat treatment in the hydrogen atmosphere. However, even though the minimum resistivity value (6.0Ω-cm) is one order of magnitude smaller compared to the minimum resistivity value of the ITO samples calcined with air flow (51.1Ω-cm) and several orders of magnitude smaller compared to the low doping metal oxide semiconductors typical in DSSCs,[41,52] it is still 4 orders of magnitude greater than the resistivity of commercially available ITO or FTO coatings (typically having sheet resistance of ~10^1Ω/sq with ~10^2nm thickness). Besides, as the calcined ITO is to encounter another calcination step after doctor blading the TiO_2 paste on top of it, it is highly probable that the calcined ITO structures may experience a further increment of resistivity. So, it is necessary to understand and confirm the significance of the ITO resistivity along with the structure in the actual solar energy conversion conditions.

4.3.4 Photoelectrochemical characterization of the DSSCs

Figure 4.6 shows solar energy conversion performances of the DSSCs built on bare FTO, flat ITO, and patterned ITO with different resistivities, respectively. The detailed results are summarized in Table 4.1. For comparison, two reference groups were constructedt on bare FTO substrate with different thickness, 8.8 and 10.7μm, respectively, as suggested in Table 4.1. These values were chosen based on the total thickness of ITO/TiO_2 structures (group 3~6) ranging from 10.2 to 11.4 μm. Assuming a flash layer thickness of the ITO patterns to be 1 μm, ITO structures would occupy 100% of the space from the FTO surface to a 1 μm height (height defined as the distance from the FTO surface in the normal direction) and 25% from 1 μm to 7.5 μm height, considering the geometry of the ITO patterns. So, by excluding the ITO volume from the total thickness (11.4μm), a thickness of 8.8μm is

obtained to give an equivalent volume of sensitized TiO_2. So, 8.8μm thick conventional DSSCs (group 1) have equivalent volumes of TiO_2 as the TiO_2 in the DSSCs of group 6, and 10.7μm; DSSCs in group 2 have comparable thickness to the apparent thickness of DSSCs with embedded ITO structures.

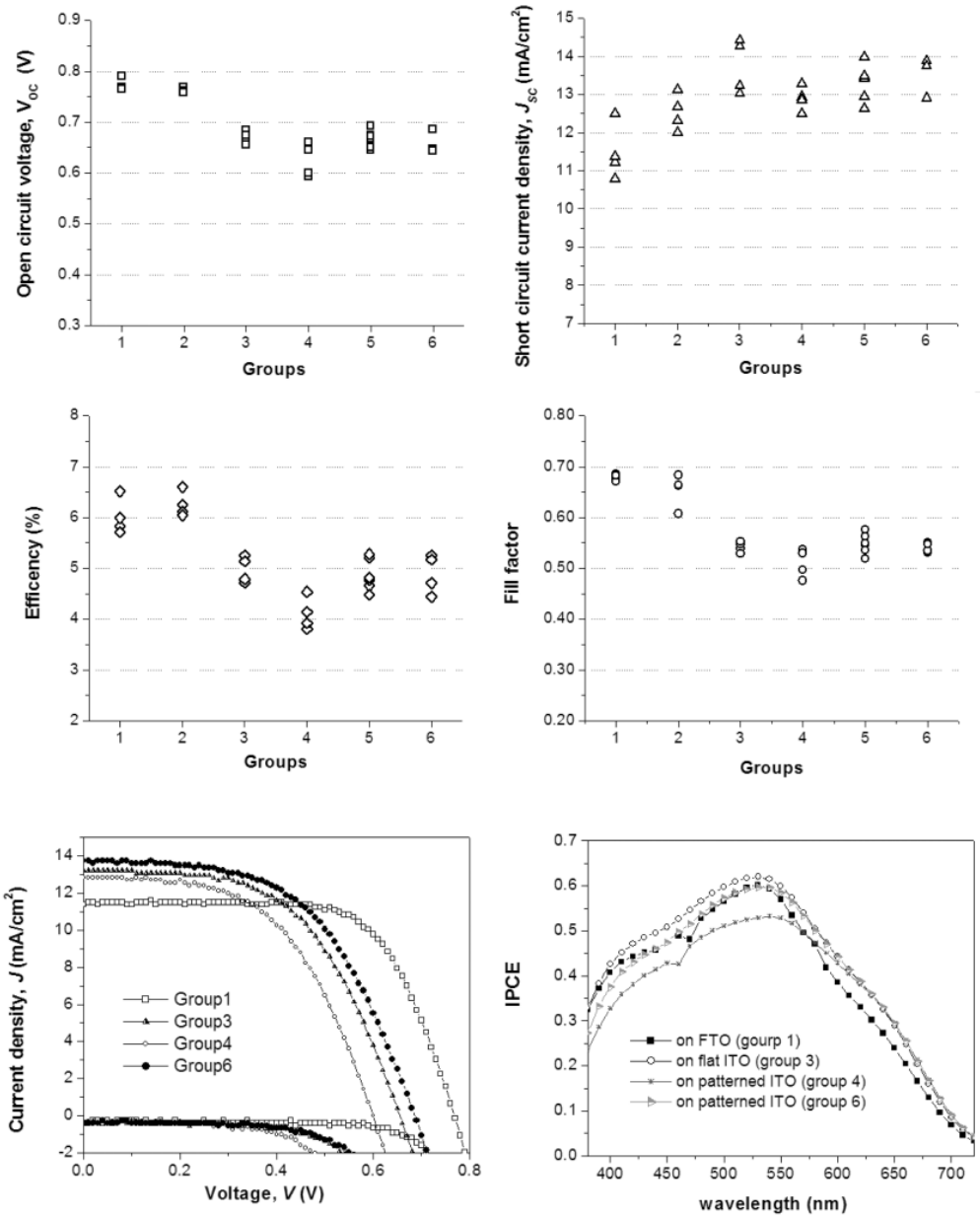

Figure 4.6 Summary of photoelectrochemical performance data of DSSCs with/without ITO structures of various thermal history. Selected incident photon-to-current conversion efficiency (IPCE) and photocurrent density (***J***)-photovoltage (**V**) curves are also shown.

It is notable in Figure 4.6 and Table 4.1 that DSSCs having embedded ITO structures revealed a decrement of the open circuit voltages ($\mathbf{V_{oc}}$), about 100mV or more compared to the reference groups built on bare FTO. The drop of the open circuit voltage seems to result from the change of the energetics of the DSSCs by the altered cell configuration. It is noteworthy that no significant change in the energetics of the DSSCs was observed if the embedded metallic bodies were built in a discrete manner on the FTO coatings and direct contact between TiO_2 and FTO was dominant.[42] In this investigation, as both ITO sub layers and TiO_2 films were trimmed to remove any direct contact between TiO_2 and FTO coatings, the energetics of the cells could have changed. This explanation can be strengthened if one considers the electrical resistivity of the ITO embedment: as the resistivity of the ITO structures are in the 6.0~51.1Ω-cm range, about 4 orders of magnitude greater than the commercial ITO films, they cannot be regarded as metallic conductors, but more reasonable be considered as a doped semiconductor.[52] So, it can be concluded that the huge drop of $\mathbf{V_{oc}}$ mainly arose from the insertion of the new doped metal oxide between FTO and TiO_2. In Table 4.1, group 4 exhibited the lowest $\mathbf{V_{oc}}$, about 40mV lower even compared to group 5 and 6 having identical architecture. As DSSCs of group 4 were built on the patterned ITO substrates with the highest resistivity (51.1Ω-cm), this can be attributable to the poorer electrical conductivity than group 5 and 6. However, the $\mathbf{V_{oc}}$ of group 3 having a flat ITO geometry is higher than that of the group 4, though the ITO preparation condition for the two groups is identical. As the volume of the sensitized TiO_2 in group 3 having a flat ITO geometry is about 200nm thick and larger by a factor 1.35, this seems to have come from the difference in the cell architectures.

The short circuit current density, $\boldsymbol{J}_{sc}$, showed a different trend to the open circuit voltage. The $\boldsymbol{J}_{sc}$ of the DSSCs with patterned ITO substrates were measured to be 12~18% higher than group 1. As the thickness of group 1 was determined to have an identical volume of sensitized TiO_2 to the patterned ITO counterparts, the increment of the short circuit current can wholly be attributed to the patterned architectures. So, as described in the introduction, it has been proved that the patterned ITO substructure is beneficial to electron collection owing to the shorter distance to the conductive ITO. However, one can see that group 3 with flat ITO layers also exhibited higher short circuit current density than reference group 1 and 2, and similar to the patterned ITO DSSCs. The increment in the short circuit current density relative to group 2 having a similar thickness can be interpreted as the effect of increased interface area:[63] as the flat ITO films were made by spin casting of viscous ITO paste containing ITO nanoparticles and polymeric phase, the film is mesoporous and not homogeneous in thickness, resulting in a larger contact area between flat ITO layer and TiO_2 film in group 3 than in group 2. The discrepancy among groups with patterned ITO architectures shows the effect of resistivity of the ITO.

Although the DSSCs with patterned ITO geometries exhibited higher short circuit current density, the global power conversion efficiency was measured to be much smaller and the fill factors were also lower than the reference groups 1 and 2. The patterned ITO groups exhibited global power conversion efficiency values only 68~83% of that of the reference group 1. Group 4, built on the ITO patterns with highest resistivity, showed the lowest power conversion efficiency (4.1%), and groups 5 and 6 were measured to have similar efficiency values (4.87 and 4.89% respectively). However, comparing groups 5 and 6, which were initially built on the ITO patterns having different resistivity values (by a factor 2

after a heat treatment in hydrogen/nitrogen mixture), it can be seen that all the factors measured and listed in Table 4.1 are identical within the error range. So, it can be inferred from the data that doctor blading of TiO_2 paste and the additional calcination step has equalized the initial resistivity difference of a factor 2, probably by further oxidation of the ITO structures. So, it can be concluded that the initial resistivity of the ITO patterns has a significant effect on the efficiency of the DSSCs after another oxidative calcination step when the initial resistivity values are different at least by an order of magnitude.

The photocurrent density-photovoltage (***J*-*V***) curves shown in Figure 4.6 clearly reveal the characteristic behavior of conventional DSSCs (group 1) and DSSCs with ITO architectures. Curves under illumination manifest the results summarized in Table 4.1, and the dark current curves also exhibited a similar trend between DSSCs under illumination. DSSCs of group 4 which showed the poorest solar energy conversion performance revealed the lowest dark current onset voltages, while group 1 reference DSSCs, which showed best conversion efficiency and fill factor, had the highest onset voltage. Group 3 with flat ITO films and group 6 with patterned ITO with lowest resistivity exhibited almost identical ***J*-*V*** behavior both in dark and illuminated conditions. As the shift of dark-current onset to lower potential is an indication of higher recombination on the electrode surface,[64] recombination of electrons seemed to influence the solar energy conversion performances primarily. As the power conversion efficiency of the conventional architecture showed the best results, it can be inferred that the embedded ITO substructures played a detrimental role in electron recombination.

For quantitative analysis of the electron transport phenomena responsible for recombination, electrochemical impedance spectroscopy (EIS) was used. Figure 4.7 is the

electrochemical impedance spectroscopy (EIS) results of selected samples. Nyquist plots (left) show that electrochemical responses of the DSSCs with and without embedded ITO structure are quite different. Bode plots (right) exhibited difference in the frequency of the peak maxima of the center arcs. Adachi et al.[65] reported the relationship between the frequency at the maxima and the effective rate constant, k_{eff}, giving the rate constant for the recombination reaction. Group 1 having conventional DSSC configuration revealed an effective rate constant k_{eff}=30s^{-1}, while DSSCs with patterned ITO structure showed 54.6s^{-1} (group 4) and 24s^{-1} (group 6) respectively. The effective rate value of group 6 sample shown in Figure 4.7 was slightly larger than that of group 1, although the slope between 24 to 30s^{-1} was very small. The effective rate constant of group 1 samples were all measured to be 30s^{-1}, while group 6 had k_{eff} ranging from 24 to 37.5s^{-1}. The largest recombination rate of group 4 gives a quantitative explanation of the low conversion efficiency and fill factors. Compared to group 1, as group 4 DSSCs have virtually identical volume of TiO_2 but exhibited a much higher recombination rate, it would be reasonable to attribute the faster recombination rate mainly to the nature of the ITO substructure: as the DSSCs of group 4 produced more short circuit current density of than group 1, it can be inferred that the diffusion rate of injected electrons in the TiO_2 network might be at least equal or faster than in the TiO_2 nanoparticle network of group 1 DSSCs. So, fewer or equal numbers of electrons in the conduction band of the TiO_2 of group 4 DSSCs are recombining with the I_3^- ions in the electrolyte. That means extra electron back transfer to the electrolyte should occur on the surface ITO patterns to balance the overall rate through the TiO_2 and ITO. This is a reasonable inference considering the faster electron back transfer from the highly doped semiconductors[52] and the presence of tremendous number of I_3^- ions coupled to the moving electrons on the surface of metal oxides

in the DSSCs.[41,43,66] In the same way, it can be concluded that the ITO also provides the faster recombination reaction sites to the electrons and I_3^- ions in the group 6 DSSCs, but not as fast as on the ITO mesoporous body of group 4, presumably due to their lower resistivity attributable to both extrinsic nanostructure with fewer defects and smaller intrinsic resistivity of individual ITO nanoparticles by the heat treatment in the 5% hydrogen atmosphere.

In terms of the mesoporous nature of ITO nanostructures, as the ITO substructures were sintered nanoparticles having loose interconnections, trapping of electrons at the defect sites and resultant interfacial recombination might have played a major role as in the mesoporous TiO_2.[41] Considering the thermal history of ITO layers used in group 4, a monotonic heating rate (2K/min) to 500°C without any holding time, it is no doubt the ITO substructures have tremendous interfacial defects let alone a degraded intrinsic conductivity of individual particles by thermal oxidation.[62] So, it can be concluded that both intrinsic conductivity of individual ITO nanoparticles by thermal oxidation/reduction and extrinsic structural elements made the ITO substructures in group 4 provide much favorable recombination sites than those of the group 6.

In general, a dense TiO_2 barrier coating has been applied in order to passivate FTO substrate to suppress electron back transfer to the electrolyte.[8,42,67,68] Yet, the conventional barrier coating formation method based on titanium chloride solution[2,67,69-71] could not be applied to the mesoporous ITO structures in this investigation, because ITO is vulnerable to chlorine ions and gets corroded away.[72-74] In my trials with the titanium chloride solution, the calcined ITO structures were all destroyed after soaking the ITO layers in the solution: as the ITO substructures were networks of ITO nanoparticles just connected by small interfacial area, the corrosive conditions were sufficient to dissolve several nanometers of dense planar

ITO would and more than enough for the collapse of the networks. So, it would be necessary to form a conformal layer onto the ITO structures by applying pulsed laser deposition [17,47-49,52] or CVD methods[75-78] to preserve the built ITO substructures.

TABLE 4.1: Summary of photoelectrochemical solar energy conversion data from DSSCs with/without ITO structures of various thermal history.

Group	Condition for ITO Thermal history / atmosphere		Thickness (μm)	V_{oc} (V)	J_{sc} (mA/cm^2)	Fill factor	Efficiency (%)
1: FTO only	-	-	8.8±0.2	0.772±0.012	11.5±0.7	0.679±0.007	6.01±0.35
2: FTO only	-	-	10.6±0.3	0.763±0.004	12.5±0.5	0.654±0.033	6.25±0.25
3: f-ITO/FTO	2K/min to 500°C	air flow	10.4±0.2	0.668±0.013	13.7±0.7	0.542±0.010	4.97±0.26
4: p-ITO/FTO	2K/min to 500°C	air flow	10.2±0.5	0.624±0.033	12.9±0.3	0.510±0.029	4.10±0.32
5: p-ITO/FTO	2K/min to 600°C + holding for 1H	closed	10.9±1.0	0.666±0.017	13.3±0.5	0.548±0.020	4.87±0.31
6: p-ITO/FTO	2K/min to 600°C + holding for 1H	closed	11.4±0.3	0.665±0.024	13.6±0.4	0.541±0.010	4.89±0.38

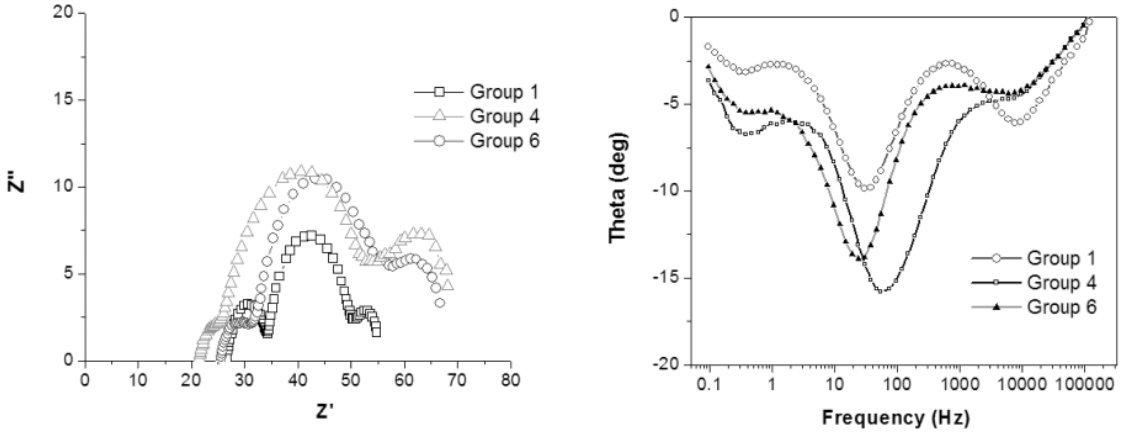

Figure 4.7 Electrochemical impedance spectroscopy (EIS) results: Nyquist plot (left) and Bode plot (right), respectively.

4.4 Conclusions

A simple surface patterning technique using soft-lithography was applied to form patterned ITO structures onto commercial FTO coatings in the DSSCs comparable to the thickness of the sensitized TiO_2 layer in order to enhance charge collection efficiency. The prepared ITO substructures on the commercial FTO coatings were mesoporous bodies with different resistivity values depending on the calcination conditions, such as holding time at the maximum calcination temperature, atmosphere, and post heat treatment in the 5% hydrogen/nitrogen mixture gas. DSSCs with embedded ITO substructures had higher short circuit current density, ranging 12.9~13.7mA/cm^2, than the conventional DSSCs (11.5 and 12.5mA/cm^2 for 8.8 and 10.6 μm thick, respectively) built on the bare FTO coatings regardless of the geometry of the ITO structures. The increment of short circuit current density can be ascribed to the patterned ITO structure which in turn, should effectively shorten the electron diffusion length to the conductive electrode and provide enhanced electron transport path by its higher conductivity than TiO_2 nanoparticle network. The significant enhancement in short circuit current density is meaningful especially because the DSSCs with patterned ITO embedment had less sensitized TiO_2 (about ~74% of reference DSSCs of identical apparent thickness) and performed with a reduced intensity of incoming light due to the high ITO features. However, the ITO substructures lowered the open circuit voltage by more than 100mV, fill factors by more than 10%, and power conversion efficiency to 4.1%~4.97%, compared to the reference cells built on the bare FTO coating (6.01% by 8.8μm thick and 6.25% by 10.6 μm thick TiO_2 films). Impedance spectroscopy revealed that the faster recombination rate of the DSSCs with ITO substructures were the cause of the diminished power conversion efficiency and low fill factor. With all the benefit

of patterned ITO geometry in increased photocurrent density, ITO structures also provided faster recombination sites due to their mesoporous morphology. So, to minimize recombination on the surface of ITO layers and utilize the full advantage of the patterned ITO geometry, it would be necessary to form a dense conformal TiO_2 coating on the ITO surface to suppress electron back transfer to the electrolyte.

4.5 References

(1) O'Regan, B.; Grätzel, M. *Nature***1991**, *353,* 737—740.

(2) Nazeeruddin, M. K.; Kay, I.; Rodicio, A.; Humphry-Baker, R.; Müller, E.; Liska, P.; Vlachopouloss, N.; Grätzel, M. *J. Am. Chem. Soc.* **1993**, *115*, 6382—6390.

(3) Nazeeruddin, M. K.; Pechy, P.; Grätzel, M. *Chem. Commun.***1997**, 1705—1706.

(4) Nazeeruddin, M.K.; Zakeeruddin, S.M.; Humphry-Baker, R.; Jirousek, M.; Liska, P.; Vlachopoulos, N.; Shklover, V.; Fischer, C.H.; Grätzel, M. *Inorg. Chem.* **1999**, *38*, 6298—6305.

(5) Wang, P.; Klein, C.; Humphry-Baker, R.; Zakeeruddin, S.; Grätzel, M. *J. Am. Chem. Soc.* **2005**,*127*, 808—809.

(6) Gao, F.; Wang, Y.; Shi, D.; Zhang, J.; Wang, M. K.; Jing, X. Y.; Humphry-Baker, R.; Wang, P.; Zakeeruddin, S. M.; Grätzel, M. *J. Am. Chem. Soc.* **2008**, *130*, 10720—10728.

(7) Huang, S. Y.; Schlichthörl, G.; Nozik, A. J.; Grätzel, M.; Frank, A. J. *J. Phys. Chem. B* **1997**, *101*, 2576—2582.

(8) Kopidakis, N.; Neale, N. R.; Frank, A. J. *J. Phys. Chem. B* **2006**, *110*, 12485—12489.

(9) Yella, A.; Lee, H.-W.; Tsao, H. N.; Yi, C.; Chandrian, A. K.; Nazeeruddin, M. K.; Diau, E. W.-G.; Yeh, C.-Y.; Zakeeruddin, S. M.; Grätzel, M. *Science* **2011**, *334*, 629—634.

(10) Tennakone, K.; Kumara, G. R. R.; Kottegoda, I. R. M.; Perera, V. S. P. *Chem. Commun.* **1999**, 15—16.

(11) Keis, K.; Magnusson, E.; Lindstrom, H.; Lindquist, S. E.; Hagfeldt, A. *Sol. Energy Mater. Sol. Cells* **2002**, *73*, 51—58.

(12) Chappel, S.; Zaban, A. *Sol. Energy Mater. Sol. Cells* **2002**, *71*, 141—152.

(13) Bergeron, B. V.; Marton, A.; Oskam, G.; Meyer, G. J. *J. Phys. Chem. B* **2005**, 109, 937—943.

(14) Sayama, K.; Suguhara, H.; Arakawa, H. *Chem. Mater.* **1998**, *10*, 3825—3832.

(15) Guo, P.; Aegerter, M. A. *Thin Solid Films* **1999**, *351*, 290—294.

(16) Lenzmann, F.; Krueger, J.; Burnside, S.; Brooks, K.; Grätzel, M.; Gal, D.; Rühle, S.; Cahen, D. *J. Phys. Chem. B* **2001**, *105*, 6347—6352.

(17) Ghosh, R.; Brennaman, M. K.; Uher, T.; Ok, M.-R.; Samulski, E. T.; McNeil, L.E.; Meyer, T. J.; Lopez, R. *ACS Appl. Mater. Interfaces* **2011**, *3*, 3929—3935.

(18) Ok, M.-R.; Ghosh, R.; Brennaman, M. K.; Lopez, R.; Meyer, T. J.; Samulski, E. T. *ACS Appl. Mater. Interfaces* **2013**, *5*, 3469—3474.

(19) Usami, A. *Chem. Phys. Lett.* **1997**, *277*, 105—108.

(20) Nishimura, S.; Abrams, N.; Lewis, B. A.; Halaoui, L. I.; Mallouk, T. E.; Benkstein, K. D.; van de Lagemaat, J.; Frank, A. J. *J. Am. Chem. Soc.* **2003**, *125*, 6306—6310.

(21) Halaoui, L. I.; Abrams, N. M.; Mallouk, T. E. *J. Phys. Chem. B* **2005**, *109*, 6334—6342.

(22) Mihi, A.; Míguez, H. *J. Phys. Chem. B* **2005**, *109*, 15968—15976.

(23) Mihi, A.; López-Alcaraz, F. J.; Míguez, H. *Appl. Phys. Lett.* **2006**, *88*, 193110—193113.

(24) Herman, L.A.; Yip, C.H.; Wong, C.C. *J. Nanosci. Nanotechnol.* **2010**, *10*, 4657—4662.

(25) Guldin, S.; Hüttner, S.; Kolle, M.; Welland, M. E.; Müller-Buschbaum, P.; Friend, R. H.; Steiner, U.; Tétreault, N. *Nano Lett.* **2010**, *10*, 2303—2309.

(26) Lee, S.-H. A.; Abrams, N. M.; Hoertz, P. G.; Barber, G. D.; Halaoui, L. I.; Mallouk, T. E. *J. Phys. Chem. B* **2008**, *112*, 14415—14421.

(27) Kim, J.; Koh, J. K.; Kim, B.; Kim, J. H.; Kim. E. *Angew. Chem. Int. Ed.* **2012**, *51*, 6864—6869.

(28) Colodrero, S.; Mihi, A.; Häggman, L.; Ocaña, M.; Boschloo, G.; Hagfeldt, A.; Míguez, H. *Adv. Mater.* **2009**, *21*, 764—770.

(29) M. Law, L.E. Greene, J.C. Johnson, R. Saykally, P.D. Yang, *Nature Mater.* **2005**, *4*, 455—459.

(30) Feng, X. J.; Shankar, K.; Varghese, O.K.; Paulose, M.; Latempa, T. J.; Grimes, C.A. *Nano Lett*. **2008**, *8*, 3781—3786.

(31) Liu, B.; Aydil, E.S. *J. Am. Chem. Soc.* **2009**, *131*, 3985—3990.

(32) Kokubo, H.; Ding, B.; Naka, T.; Tsuchihira, H.; Shiratori, S. *Nanotechnology* **2007**, *18*, 165604.

(33) Fujihara, K.; Kumar, A.; Jose, R.; Ramakrishna, S.; Uchida, S. *Nanotechnology* **2007**, *18*, 365709.

(34) Roy, P.; Kim, D.; Lee, K.; Spiecker, E.; Schmuki, P. *Nanoscale* **2010**, *2*, 45—59.

(35) Zhu, K.; Neale, N.; Miedaner, A.; Frank, A. *Nano Lett.* **2002**, *7*, 69—74.

(36) Gong, D.; Grimes, C.A.; Varghese, O.K.; Hu, W.C.; Singh, R.S.; Chen, Z.; Dickey, E.C. *J. Mater. Res.* **2001**, *16*, 3331—3334.

(37) Mor, G.K.; Varghese, O.K.; Paulose, M.; Shankar, K.; Grimes, C.A. *Sol. Energy Mater. Sol. Cells* **2006**, *90*, 2011—2075.

(38) Ghicov, A.; Schmuki, P. Chem. Commun. 2009, 2791—2808.

(39) Paulose, M.; Shankar, K.; Yoriya, S.; Prakasam, H. E.; Varghese, O.K.; Mor, G.K.; Latempa, T.A.; Fitzgerald, A.; Grimes, C. A. *J. Phys. Chem. B* **2006**, *110*, 16179—16184.

(40) Stergiopoulos, T.; Ghicov, A.; Likodimos, V.; Tsoukleris, D. S.; Kunze, J.; Schmuki, P.; Falaras, P. *Nanotechnology* **2008**, *19*, 235602.

(41) Grätzel, M. *Inorg. Chem.* **2005**, *44*, 6841—6851.

(42) Yang, Z.; Xu, T.; Gao, S.; Welp, U.; Kwok, W.-K. *J. Phys. Chem. C* **2010**, *114*, 19151—19156.

(43) Kopidakis, N.; Schiff, E. A.; Park, N.-G.; van de Lagemaat, J.; Frank, A. J. *J. Phys. Chem. B* **2000**, *104*, 3930–3936.

(44) Kron, G.; Egerter, T.; Werner, J. H.; Rau, U. *J. Phys. Chem. B* **2009**, *107*, 3556–3564.

(45) Chen, W.; Zhang, H. F.; Hsing, I. M.; Yang, S. H. *Electrochem. Commun.* **2009**, *11*, 1057—1060.

(46) Jiang, C.Y.; Sun, X. W.; Lo, G. Q.; Kwong, D. L.; Wang, J. X. *Appl. Phys. Lett.* **2007**, *90*, 263501.

(47) Sauvage, F.; Di Fonzo, F.; Li Bassi, A; Casari, C. S.; Russo, V.; Divitini, G.; Ducati, C.; Bottani, C. E.; Compte, P.; Gratzel, M. *Nano Lett.* **2010**, *10*, 2562−2567.

(48) Noh, J. H.; Park, J. H.; Han, H. S.; Kim, D. H.; Han, B. S.; Lee, S.; Kim, J. Y.; Jung, H. S.; Hong, K. S. *J. Phys. Chem. C* **2012**, *116*, 8102−8110.

(49) Ghosh, R.; Hara, Y.; Alibabaei, L.; Hanson, K.; Rangan, S.; Bartynski, R.; Meyer, T. J.; Lopez, R. *ACS Appl. Mater. Interfaces* **2012**, *4*, 4566−4570.

(50) Martinson, A. B. F.; Elam, J. W.; Liu, J.; Pellin, M. J.; Marks, T. J.; Hupp, J. T. *Nano Lett.* **2008**, *8*, 2862−2866.

(51) Yang, Z.; Gao, S.; Li, W.; Vlasko-Vlasov, V.; Welp, U.; Kwok, W.-K.; Xu, T. *ACS Appl. Mater. Interfaces* **2011**, *3*, 1101−1108.

(52) Yang, Z.; Gao, S.; Li, T.; Liu, F.-Q.; Ren, Y.; Xu, T. *ACS Appl. Mater. Interfaces* **2012**, *4*, 4419−4427.

(53) Wang, F.; Subbaiyan, N. K.; Wang, Q.; Rochford, C.; Xu, G.; Lu, R.; Elliot, A.; D'Souza, F.; Hui, R.; Wu, J. *ACS Appl. Mater. Interfaces* **2012**, *4*, 1565−1572.

(54) Zhao, X.-M.; Xia, Y.; Whitesides, G. M. *J. Mater. Chem.* **1997**, *7*, 1069−1074.

(55) Rolland, J. P.; Van Dam, R. M.; Schorzman, D. A.; Quake, S. R.; DeSimone, J. M. *J. Am. Chem. Soc.***2004**, *126*, 2322−2323.

(56) Rolland, J. P.; Hagberg, E. C.; Denison, G. M.; Carter, K. R.; DeSimone, J. M. *Angew. Chem. Int. Ed.***2004**, *43*, 5796−5799.

(57) Hampton, M. J.; Williams, S. S.; Zhou, Z.; Nunes, J.; Ko, D.-H.; Templeton, J. L.; Samulski, E. T.; DeSimone, J. M. *Adv. Mater.* **2008**, *20*, 2667−2673.

(58) Hoertz, P. G.; Chen, Z.; Kent, C. A.; Meyer, T. J. *Inorg. Chem.* **2010**, *49*, 8179–8181.

(59) Wang, Z.-S.; Kawauchi, H.; Kashima, T.; Arakawa, H. *Coord. Chem. Rev.* **2004**, *248*, 1381−1389.

(60) Ko, D.-H.; Tumbleston, J. R.; Zhang, L.; Williams, S.; DeSimone, J. M.; Lopez, R.; Samulski, E. T. *Nano Lett.* **2009**, *9*, 2742−2746.

(61) Wenger, S. Strategies to Optimizing Dye-Sensitized Solar Cells: Organic Sensitizers, Tandem Device Structures, and Numerical Device Modeling. Ph. D. Dissertation, École Polytechnique Fédérale de Lausanne, Lausanne, Switzerland, 2010.

(62) Kim, Y.-N.; Shin, H.-G.; Song, J.-K.; Cho, D.-H.; Lee, H.-S.; Jung, Y.-G. *J. Mater. Res.* **2005**, *20*, 1574−1579.

(63) Fan, Z.; Razavi, H.; Do, J.-W.; Moriwaki, A.; Ergen, O.; Chueh, Y.-L.; Leu, P. W.; Ho, J. C.; Takahashi, T.; Reichertz, L. A.; Neala, S.; Yu, K.; Wu, M.; Ager, J. W.; Javey, A. *Nat. Mater.* **2009**, *8*, 648−653.

(64) Ramasamy, E.; Lee, J. *J. Phys. Chem. C* **2010**, *114*, 22032−22037.

(65) Adachi, M.; Sakamoto, M.; Jiu, J.; Ogata, Y.; Isoda, S. *J. Phys. Chem. B* **2006**, *110*, 13872—13880.

(66) van de Lagemaat, J.; Park, N.-G.; Frank, A. J. *J. Phys. Chem. B* **2000**, *104*, 2044—2052.

(67) Kavan, L.; O'Regan, B.; Kay, A.; Grätzel, M. *J. Electroanal. Chem.* **1993**, *346*, 291−307.

(68) Cameron, P. J.; Peter, L. M. *J. Phys. Chem. B* **2003**, *107*, 14394−14400.

(69) Barbe, C. J.; Arendse, F.; Comte, P. *J. Am. Ceram. Soc.* **1997**, *80*, 3157−3171.

(70) Park, N. G.; Schlichthörl, G.; van de Lagemaat, J.; Cheong, H. M.; Mascarenhas, A.; Frank, A. J. *J. Phys. Chem. B* **1999**, *103*, 3308−3314.

(71) Ito, S.; Liska, P.; Comte, P.; Charvet, R. L.; Péchy, P.; Bach, U.; Schmidt-Mende, L.; Zakeeruddin, S. M.; Kay, A.; Nazeeruddin, M. K.; Grätzel, M. *Chem. Commun.* **2005**, 4351−4353.

(72) Folcher, G.; Cachet, H.; Froment, M.; Bruneaux, J. *Thin Solid Films* **1997**, *301*, 242—248.

(73) Huang, C. J.; Su, Y. K.; Wu, S. L. *Mater. Chem. Phys.* **2004**, *84*, 146—150.

(74) Brumbach, M.; Veneman, P. A.; Marrikar, F. S.; Schulmeyer, T.; Simmonds, A.; Xia, W.; Lee, Armstrong, N. R. *Langmuir* **2007**, *23*, 11089—11099.

(75) Pazoki, M.; Taghavinia, N.; Abdi, Y.; Tajabadi, F.; Boschloo, G.; Hagfeldt, A. *RSC Adv.* **2012**, *2*, 12278—12285.

(76) Lee, J.; Park, K.; Kim, T.; Choi, H.; Sung, Y. *Nanotechnology* **2006**, *17*, 4317—4321.

(77) Wu, J.; Shih, H. C.; Wu, W. *Chem. Phys. Lett.* **2005**, *413*, 490—494.

(78) Lee, J.; Sung, Y.; Kim, T. G.; Choi, H. *Appl. Phys. Lett.* **2007**, *91*, 113104.

CHAPTER 5

GENERAL CONCLUSIONS AND FUTURE RESEARCH DIRECTIONS

5.1 General conclusions

The simple surface patterning method using soft-lithographic techniques was an effective strategy to modify the architecture of the DSSCs without significant addition to cost and production complexity. Surface patterns on several hundred nanometer scales and substrate structures with 5 to ~6.5μm dimensions were successfully fabricated on an area of several square millimeters and these patterns altered the physical and electrochemical characteristics of the DSSCs.

Surface patterns with 400 nm to 1000 nm periods and only 135~175nm in height changed the optical response of the mesoporous oxide layers in the UV-vis range, Nevertheless these rather small patterns were confirmed to form photonic crystal (PC) effects. Optical measurements showed that the surface PC structure resulted in increments of absorption of photons, or the enhancement of the light harvesting efficiency (LHE), especially when intrinsic absorption is low, e.g., the Nb_2O_5 layers 3μm thick with coarse nanostructures described in Chapter 2. However, the PC effect on the LHE enhancement is not clear when the intrinsic absorption is close to unity, e.g., highly sensitized TiO_2 layers 10μm thick, as shown in Chapter 3. Nevertheless, the IPCEs of both Nb_2O_5 and TiO_2 were enhanced by the surface PC structure over the whole wavelength range of the UV-visible

spectrum, and the enhancement varied as a function of surface patterns (Chapter 2 and 3). Moreover, although the LHEs of sensitized TiO_2 layers were measured to be virtually identical between flat and patterned groups regardless of the pattern geometry, the solar energy conversion results showed significant improvement caused by the surface PC structures. The global efficiency was enhanced up to ~16% by the small surface features. So, the data imply that surface PC structures influence the LHE directly or result in changes in optics which can alter the diffusion process of electrons in the DSSCs and increase the charge collection efficiency (CCE). Based on the optical simulations that revealed an amplified field strength and strong interactions within IR range, I hypothesized a potential relationship between the PC structures and diffusional processes in the DSSCs. For the confirmation of my hypothesis, further analysis using electrochemical impedance spectroscopy (EIS) is required.

A simple surface patterning technique using soft-lithography was applied to form patterned ITO structures on commercial FTO coatings in the DSSCs; the thickness of the structures was comparable to that of the sensitized TiO_2 layer in order to enhance charge collection efficiency. DSSCs with embedded ITO substructures had higher short circuit current densities than the conventional DSSCs built on the bare FTO coating regardless of the geometry of the ITO structures. The increment of short circuit current density can be ascribed to the patterned ITO structure which could more effectively shorten the electron diffusion length to the TCO and provide enhanced electron transport path by its higher conductivity than the TiO_2 nanoparticle network. However, ITO substructures lowered the open circuit voltages by more than 100mV, lowered fill factors by more than 10%, and lowered power conversion efficiencies by 1~2% in absolute scale, compared to the reference

cells built on a bare FTO coating. Impedance spectroscopy was used to analyze the decrements, and revealed that a faster recombination rate in the DSSCs with ITO substructures was the cause of the diminished power conversion efficiency and the low fill factor. As the ITO patterns were built of ITO nanoparticles, the final calcined structures were mesoporous and the large surface area acted as faster recombination sites. Despite all of the benefits of patterned ITO geometry in increased photocurrent density, ITO structures also provided faster recombination sites due to their mesoporous morphology. So, to minimize recombination on the surface of ITO layers and utilize the full advantage of the patterned ITO geometry, it is necessary to form a dense conformal TiO_2 coating on the ITO surface to suppress electron back transfer to the electrolyte.

5.2 Future research direction

In the previous chapters, I showed that soft-lithographic techniques are useful for the modification of the DSSC architectures without a significant increment of complexity of the manufacturing processes. The basic concept of the structural alterations used in this study was to form structures that influence LHE or CCE via the simplest manual processes, e.g., using soft-lithographic processes for patterning, heat treatments in a furnace, and solution treatments. Some of my trials structural modifications were handicapped by the limitations of using simple manual processes, e.g., the fast recombination on the ITO patterned surface which could not be passivated by conventional solution treatments. So, one main idea for the next logical research direction is to put forward the improvement of current soft-lithographic techniques of this study by combining more complex manufacturing methodologies than the

simple manual patterning processes, to the extent that those would not diminish the benefits of the manual, soft-lithographic techniques—namely, its easiness and its low production cost.

Another future direction is to turn our attention to new materials or systems not fully optimized yet; the DSSCs have already been optimized over the last two decades. This view is strengthened if one compares the discrepancy in the enhancement of photon absorption by the surface PC structure in the Nb_2O_5 layers (Chapter 2) only recently under consideration versus the TiO_2 films (Chapter 3) that have undergone optimization for more than 20 years. So, one section will be allocated to discussions of photoelectrochemical solar energy conversion systems other than the DSSCs.

5.2.1 Passivation of the patterned ITO surface

As stated in Chapter 4, patterned ITO dramatically raised the short circuit current density of the DSSCs while abating the fill factor and global efficiency resultantly. This was due to faster recombination on the ITO surface not passivated by a TiO_2 barrier layer. As the solution-based treatment common in the literature[1-3] caused the ITO nanoparticle network to collapsed because of the presence of the chlorine ion (Cl^-),[4] new methods which can build conformal TiO_2 layers on patterned ITO surfaces are needed. However, as the patterned ITO substructures have a mesoporous morphology, deposition methods guaranteeing good surface coverage must be utilized.

Pulsed laser deposition (PLD)[5-7] is the best candidates for this purpose. Moreover, as the PLD method can generate special aligned TiO_2 structures without sacrificing the porosity,[5,6] combined processes can fabricate architectures of patterned ITO/dense TiO_2 coverage/tree-like aligned TiO_2. Figure 5.1[5] is an example of the mesoporous aligned TiO_2 structure fabricated by PLD. As shown in the figure, by changing the oxygen partial pressure,

different porosity and morphologies can be obtained. PLD is also able to form doped TiO_2 structures as reported by Ghosh et al.[6] So, PLD is not simly a technique to form conformal layers on top of the patterned ITO, but a versatile method to introduce new architectures.

Chemical vapor deposition (CVD)[8-10] is a widely used technique to form thin films from chemical vapor sources with good coverage in nature. It can deposit not only dense thin films on the substrate, but it can produce films of various morphologies by changing experimental conditions: Figure 5.2 is a good example of the TiO_2 structures fabricated by the CVD technique, TiO_2 nanowires grown on the Au-doped TiO_2/Si substrate.[10] So, a combination of soft-lithographic techniques and CVD might be expected to produce a lot of new architectures and functional materials.

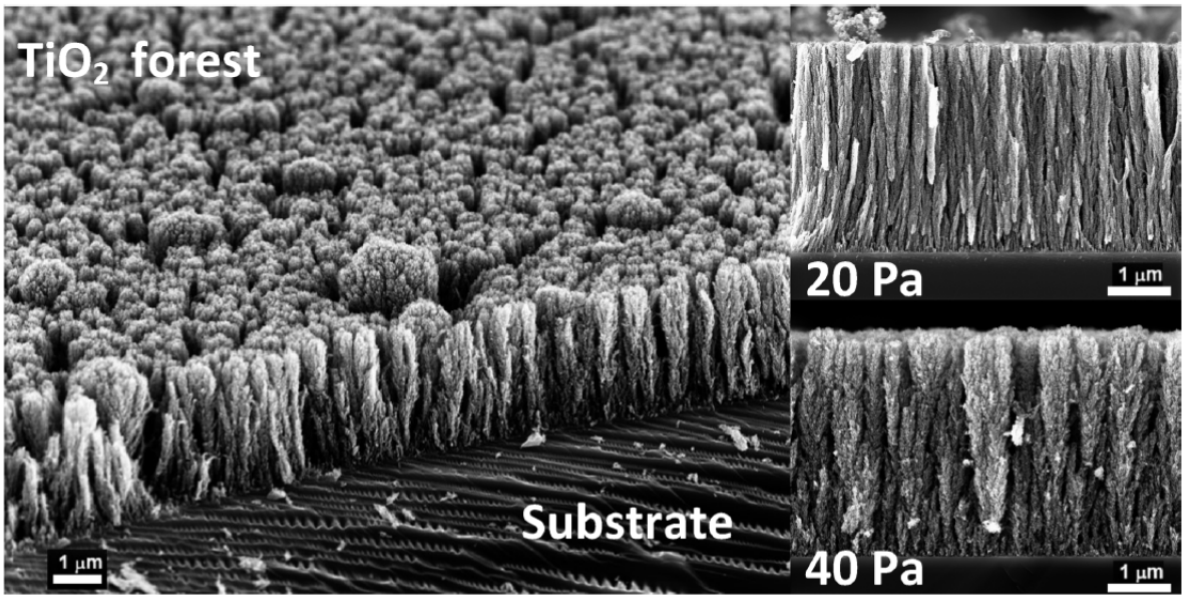

Figure 5.1 Mesoporous aligned structure fabricated by PLD method. (Reprinted with permission from reference 5. Copyright © 2010 American Chemical Society)

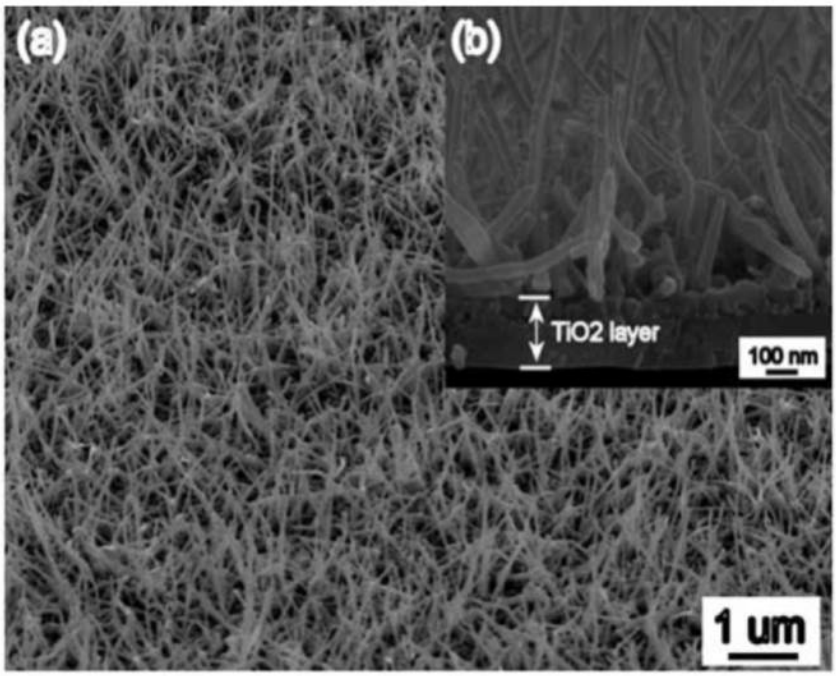

Figure 5.2 (a) TiO_2 nanowires grown all over the substrate and (b) side view revealing that the nanowires were grown on the Au-doped TiO_2/Si substrate. (Reprinted with permission from reference 10. Copyright © 2005 Elsevier B. V.)

5.2.2 Bicontinuous mesoporous structures

Although conventional random network of TiO_2 nanoparticles is a highly optimized structure for maximized dye loading owing to its porosity, it retains a tremendous number of interfacial defects at sintered particle connection sites, and these are the preferred recombination sites for the injected electrons during the diffusional charge collection.[11] So, fabrication of mesoporous but bicontinuous structures is a key technology prerequisite for increasing the global efficiency of current DSSCs. But it is still challenging to develop a bicontinuous structure without sacrificing the porosity at the same time.[12] Amphiphilic Bock copolymers have been attracting researchers' attention because of its ability of self-assemble and function as a template.[13-19] Yang et al. extended this strategy to a variety of metal oxides and reported ordered mesoporous metal oxide structures with pore sizes of ~15nm, as shown

in Figure 5.3.[19] Guldin et al.[20] reported a bilayer structure of inverse opal/mesoporous TiO_2 structure and adapted bicontinuous TiO_2 structure for sensitized TiO_2 layer by using block copolymers. Another example of a highly ordered mesoporous structure is a double gyroid structure reported by Scherer and Steiner.[21] They fabricated a bicontinuous double gyroid structures for electrochromic devices by using the polystyrene-b-poly (D,L-lactide) block copolymer, as shown in Figure 5.4.[21] The bicontinuous mesoporous structures can be optimized by using various combinations of block copolymers. As the porosity of typical bicontinuous structures is just in the 15nm range,[19] there is no conflict between the pore sizes and the pattern scales of this study (several hundred nanometers in scale for surface PC and several micrometer scale for faster pathways), and it could be synergic if combined with the patterning methods suggested in this study.

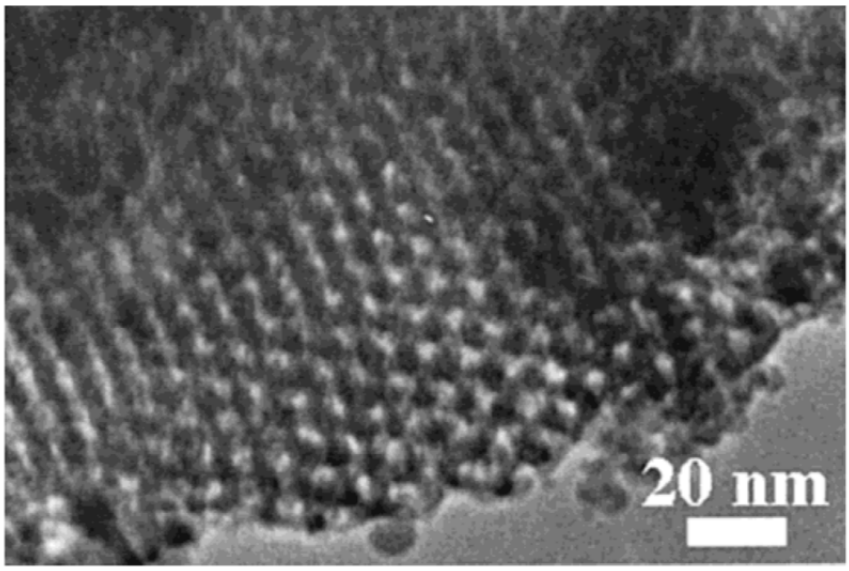

Figure 5.3 TEM image of 2-dimensional hexagonal mesoporous SnO_2 along [001] zone axis. (Reprinted with permission from reference 19. Copyright © 1999 American Chemical Society)

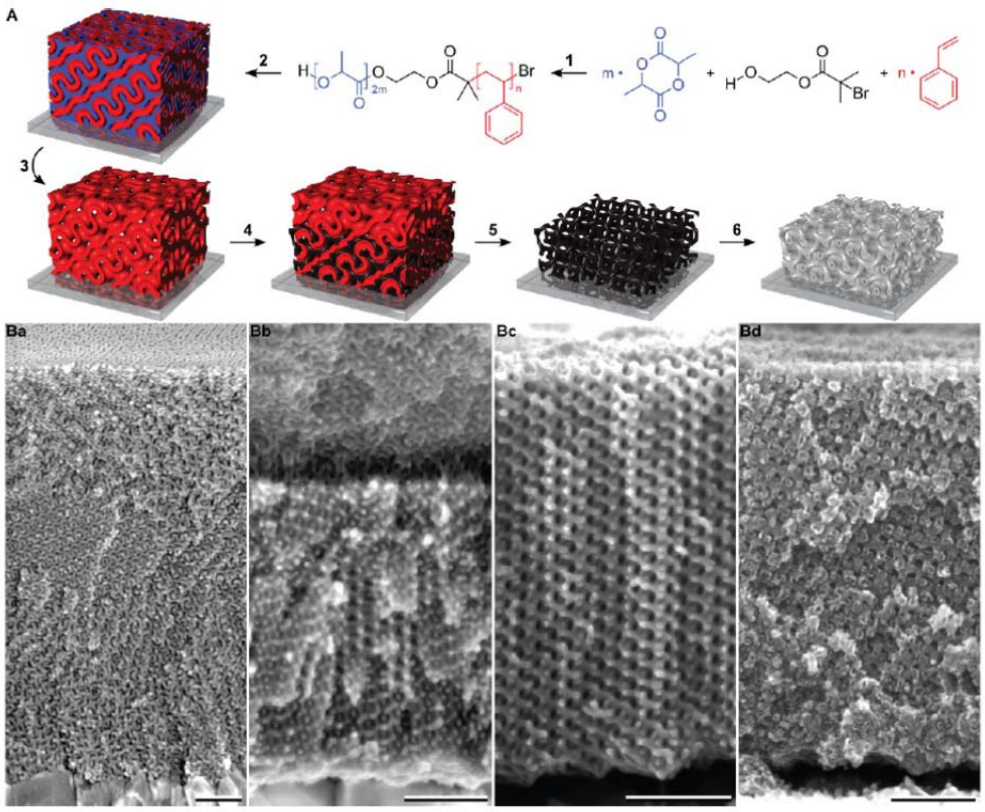

Figure 5.4 Double gyroid structure as an example of bicontinuous mesoporous structure. (Reprinted with permission from reference 21. Copyright © 2013 American Chemical Society)

5.2.3 Application of patterned geometry to other solar energy systems

Although the patterning strategy was applied only to the DSSC architectures in this study, there are also other solar energy conversion systems under development. Since the first demonstration by using TiO_2 electrode,[22,23] research is ongoing to oxidize water to produce solar fuels using the hematite,[24-29] or nano ITO,[30,31] for example. Capturing solar energy and converting it to chemical energy forms is a more convenient way to utilize photons, as the electricity generated by photovoltaic cells must be consumed immediately or stored, as pointed out by Grätzel.[24] In addition, daily or seasonal fluctuations of incident solar energy flux provides good reasons to produce solar fuels.

Among the materials in search, hematite, or α-Fe_2O_3, is a most promising material due to its chemical stability, small band gap energy (reported as 1.9~2.2eV, corresponding to 560~650nm, depending on the preparation method[26]), and most importantly it is really cheap and abundant on earth.[24] Its application is still challenging due to its low conductivity and mismatch in energy levels to the red/ox potential of water.[24] Doping with group IV elements is a frequently used strategy to overcome the conductivity problem,[27-29] and tandem cell with a DSSC is one concept to overcome the mismatch, as shown in Figure 5.5.[24]

Basically, these systems are encountering the same problems DSSCs have overcome during the last two decades. So, patterning strategies on the substrates (for enhanced charge transport) or on the photoactive materials (for enhanced LHE by the PC structure) are expected to be crucial to working out increments in conversion efficiency.

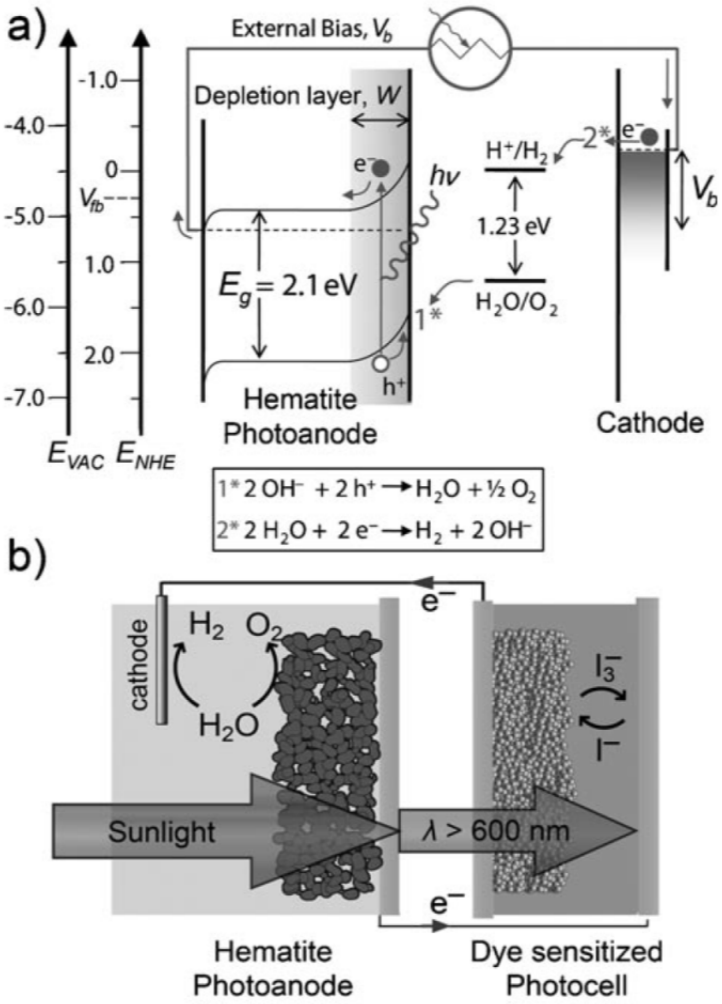

Figure 5.5 Schematic representation of the photoelctrochemical water splitting by using a hematite electrode in (a), and tandem cell architecture to provide appropriate bias to the hematite electrode in (b). The tandem cell structure takes advantage of the mismatch in band gap energy of hematite and dye molecules sensitizing the TiO_2 nanoparticles. (Reprinted with permission from reference 24. Copyright © 2011 Wiley-VCH Verlag GmbH& Co. KGaA, Weinheim)

5.3 References

(1) Kavan, L.; O'Regan, B.; Kay, A.; Grätzel, M. *J. Electroanal. Chem.* **1993**, *346*, 291−307.

(2) Park, N. G.; Schlichthörl, G.; van de Lagemaat, J.; Cheong, H. M.; Mascarenhas, A.; Frank, A. J. *J. Phys. Chem. B* **1999**, *103*, 3308−3314.

(3) Ito, S.; Liska, P.; Comte, P.; Charvet, R. L.; Péchy, P.; Bach, U.; Schmidt-Mende, L.; Zakeeruddin, S. M.; Kay, A.; Nazeeruddin, M. K.; Grätzel, M. *Chem. Commun.* **2005**, 4351−4353.

(4) Folcher, G.; Cachet, H.; Froment, M.; Bruneaux, J. *Thin Solid Films* **1997**, *301*, 242—248.

(5) Sauvage, F.; Di Fonzo, F.; Li Bassi, A; Casari, C. S.; Russo, V.; Divitini, G.; Ducati, C.; Bottani, C. E.; Compte, P.; Gratzel, M. *Nano Lett.* **2010**, *10*, 2562−2567.

(6) Noh, J. H.; Park, J. H.; Han, H. S.; Kim, D. H.; Han, B. S.; Lee, S.; Kim, J. Y.; Jung, H. S.; Hong, K. S. *J. Phys. Chem. C* **2012**, *116*, 8102−8110.

(7) Ghosh, R.; Hara, Y.; Alibabaei, L.; Hanson, K.; Rangan, S.; Bartynski, R.; Meyer, T. J.; Lopez, R. *ACS Appl. Mater. Interfaces* **2012**, *4*, 4566−4570.

(8) Pazoki, M.; Taghavinia, N.; Abdi, Y.; Tajabadi, F.; Boschloo, G.; Hagfeldt, A. *RSC Adv.* **2012**, *2*, 12278—12285.

(9) Lee, J.; Park, K.; Kim, T.; Choi, H.; Sung, Y. *Nanotechnology* **2006**, *17*, 4317—4321.

(10) Wu, J.; Shih, H. C.; Wu, W. *Chem. Phys. Lett.* **2005**, *413*, 490—494.

(11) Grätzel, M. *Inorg. Chem.* **2005**, *44*, 6841—6851.

(12) Zhang, Q.; Cao, G. *Nano Today* **2011**, *6*, 91–109.

(13) Förster, S.; Antonietti, M *Adv. Mater*. **1998**, *10*, 195-217.

(14) Tian, Z.; Tong, W.; Wang, J.; Duan, N.; Krishnan, V. V.; Suib, S. L. *Science* **1997**, *276*, 926-930.

(15) Bagshaw, S. A.; Pinnavaia, T. J. *Angew. Chem., Int. Ed. Engl*. **1996**, *35*, 1102-1105.

(16) Antonelli, D. M.; Ying, J. Y. *Angew. Chem., Int. Ed. Engl*. **1995**, *34*, 2014-2017.

(17) Antonelli, D. M.; Ying, J. Y. *Chem. Mater*. **1996**, *8*, 874-881.

(18) Ciesla, U.; Schacht, S.; Stucky, G. D.; Unger, K. K.; Schüth, F. *Angew. Chem., Int. Ed. Engl.* **1996**, *35*, 541-543.

(19) Yang, P.; Zhao, D.; Margolese, D. I.; Chmelka, B. F.; Stucky, G. D. *Chem. Mater.* **1999,** *11*, 2813-2826.

(20) Guldin, S.; Hüttner, S.; Kolle, M.; Welland, M. E.; Müller-Buschbaum, P.; Friend, R. H.; Steiner, U.; Tétreault, N. *Nano Lett.* **2010**, *10*, 2303—2309.

(21) Scherer, M.; Steiner, U. *Nano Lett.* **2013**, *13*, 3005-3010.

(22) Boddy, P. J. *J. Electrochem. Soc.* **1968**, *115*, 199-203.

(23) Fujishima, A.; Honda, K. *Nature* **1972**, *238*, 37-38.

(24) Sivula, K.; Le Formal, F.; Grätzel, M. *ChemSusChem,* **2011**, *4*, 432-449.

(25) Kumari, S.; Tripathi, C.; Singh, A. P.; Chauhan, D.; Shrivastav, R.; Dass, S.; Satsangi, V. R. *Curr. Sci.* **2006**, *91*, 1062– 1064.

(26) Lindgren, T.; Vayssieres, L.; Wang, H.; Lindquist, S. E. *Chem. Phys. Nanostruct. Semicond.* **2003**, 83–110.

(27) Goodenough, J. B. *Prog. Solid State Chem.* **1971**, *5*, 145– 399.

(28) Kennedy, J. H.; Anderman, M.; Shinar, R. *J. Electrochem. Soc.* **1981**, *128*, 2371 –2373.

(29) Jang, J. S.; Lee, J.; Ye, H.; Fan, F. R. F.; Bard, A. J. *J. Phys. Chem. C* **2009**, *113*, 6719 – 6724.

(30) Concepcion, J. J.; Jurss, J. W.; Hoertz, P. G.; Meyer, T. J. *Angew. Chem., Int. Ed.* **2009**, *48*, 9473-9476.

(31) Hoertz, P. G.; Chen, Z.; Kent, C. A.; Meyer, T. J. *Inorg. Chem.* **2010**, *49*, 8179-8181.